Dissertation

submitted to the

Combined Faculty of Natural Sciences and Mathematics

of Heidelberg University, Germany

for the degree of

Doctor of Natural Sciences

Put forward by
Michael Christoph Paulsen, M. Sc. in Physics
Dr. rer. nat. in Mathematics
born in: Bad Schwalbach

Oral examination: 17th of February 2022

High resolution beta spectrometry with metallic magnetic calorimeters for radionuclide metrology

Referees: Prof. Dr. Christian Enss
Prof. Dr. Maurits Haverkort

Accurate beta spectra measurements are important for radionuclide metrology, validation of theoretical calculations and other applications. To date, most beta spectra were measured with semiconductor detectors and magnetic spectrometers. These methods suffer from low energy resolutions compared to what is achievable with low temperature detectors. Metallic Magnetic Calorimeters (MMCs) with the radionuclide sample embedded in a 4π absorber have proven to be among the best beta spectrometers in terms of energy resolution and threshold, linearity and detection efficiency, notably for low energy beta transitions. In this work, the beta spectrum of ^{99}Tc ($Q^- = 293.8\,\mathrm{keV}$) that was measured using an optimized MMC detector is presented. It features an energy resolution of approximately 100 eV and two orders of magnitude lower energy thresholds ($\sim 0.75\,\mathrm{keV}$) compared to measurements recommended in the literature. The result suggests a spectrum shape which deviates significantly from hitherto theoretical calculations and semi-empirical extrapolations at lower energies ($< 25\,\mathrm{keV}$). Furthermore, suboptimal quantum efficiency in microcalorimeters, due to their geometry or energy detection losses caused by high energy beta emitters such as ^{36}Cl ($Q^- = 709.5\,\mathrm{keV}$), is addressed. In such cases, the resulting beta spectrum distortions can be efficiently corrected with a novel algorithm that relies on extensive Monte Carlo simulations.

Hochauflösende Betaspektrometrie mittels metallischer magnetischer Kalorimeter für die Radionuklidmetrologie

Genau gemessene Betaspektren werden für die Radionuklidmetrologie sowie Validierung theoretischer Berechnungen und weitere Anwendungen benötigt. Bis dato wurden überwiegend Halbleiterdetektoren und Magnetspektrometer für derartige Messungen verwendet. Diese Methoden haben relativ geringe Energieauflösungen im Vergleich zu Tieftemperaturdetektoren. Metallische Magnetische Kalorimeter (MMCs), wobei die Radionuklidquelle im Absorber komplett eingebettet wird, haben sich dabei als ausgezeichnete Betaspektrometer erwiesen. Wegen ihrer Linearität und Energieauflösung, Detektionsschwelle und -effizienz gilt dies insbesondere für Betaübergänge niedriger Energien. In der vorliegenden Arbeit wird ein Betaspektrum von ^{99}Tc ($Q^- = 293.8\,\mathrm{keV}$), das mit einem optimierten MMC-Detektor gemessen wurde, präsentiert. Es besitzt eine Energieauflösung von ca. $100\,\mathrm{eV}$ und eine Detektionsschwelle ($\sim 0.75\,\mathrm{keV}$) die zwei Größenordnungen geringer ist als empfohlene Spektren der Literatur. Der Spektrumverlauf weicht signifikant von derzeitigen, theoretischen Spektren und semi-empirischen Extrapolationen bei niedrigen Energien ($< 25\,\mathrm{keV}$) ab. Weiterhin werden Mikrokalorimeter mit suboptimalen Detektionseffizienzen, verursacht durch ihre Geometrie oder Energieverlusten von Betaemittern höherer Energie wie z. B. ^{36}Cl ($Q^- = 709.5\,\mathrm{keV}$), betrachtet. In solchen Fällen kann das resultierende Betaspektrum mit einem neuartigen Algorithmus, der auf Monte Carlo-Simulationen basiert, korrigiert werden.

Contents

"Die Naturwissenschaft ist der harte Kern der neuzeitlichen Kultur: der neuzeitlichen, abendländischen Kultur. Der harte Kern, das heißt nicht ihr höchstes Ziel, nicht ihr schönster Duft, nicht ihre süßeste Frucht, sondern ihr harter Kern an der man sich die Zähne ausbeißen kann. Es sind diejenigen Erkenntnisse, die am zweifellosesten sind, die man gewonnen hat, ob sie nun wichtig sind oder nicht aber man kommt nicht an ihnen vorbei. So viel wage ich zu sagen über die historische Rolle der Naturwissenschaft."

C. F. von Weizsäcker [Wei92]

1 Introduction

Variants of elements with unstable nuclei, so called radioisotopes or *radionuclides*, have been studied for over a hundred years. The discovery of radioactivity by Henri Becquerel in 1896 gave science and humanity a novel perspective on the natural world. As a result, the theories of weak and strong interaction were developed along with a wealth of experimental methods. Currently, around 3300 radionuclides are known, as depicted in figure 1.5. These have very diverse properties concerning the type of radiation that they emit, their stability and natural occurrence. For this reason, the applications (in e.g. archeology, cosmology, energy production, environmental research, geology, medicine, metrology or weaponry) are manifold [LAn16] and at times controversial. It is of utmost importance to measure the properties of radionuclides in order to

- break new ground in fundamental physics,
- benefit from applications and
- reduce the potential harm for the living world caused by their ionizing radiation.

The radiation is classified into alpha (helium cores), beta (electrons or positrons) and gamma (photons) particles, as depicted in figure 1.1.

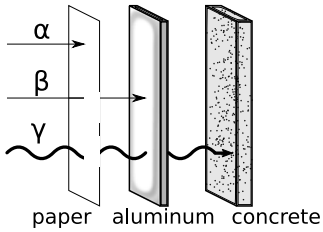

Figure 1.1: Illustration of radiation types and stopping powers of materials.

A significant property of a radionuclide is its *spectrum* i.e. the energy distribution of the emitted radiation caused by the nuclear decay. In the first decades of measuring the emitted particles of radioactive materials, it was found that the spectrum as illustrated in figure 1.2 would consist of a single line or possibly several lines with specific energies. Inconsistencies appeared when beta emitters were measured in the early 1900s.

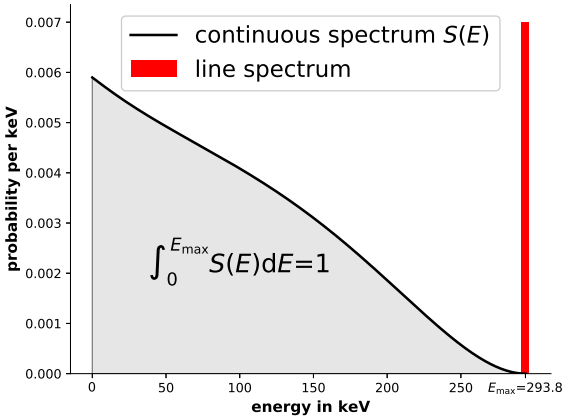

Figure 1.2: Beta spectrum $S(E)$ of ^{99}Tc calculated with BetaShape [Bet21] and a single line spectrum, which one would expect if only monoenergetic electrons were emitted.

Their spectra seemed to consist of an unlimited number of lines. This caused the scientific community including the experimenters to doubt these results and the methods with which they were achieved. That beta spectra are in fact continuous was definitely settled in 1927 by Ellis and Wooster's measurement of ^{210}Bi using a calorimetric setup and confirmed in 1930 by Meitner and Orthmann [Fra09]. Several theoretical explanations to why the measured beta electron energy displays a continuous distribution were suggested including non-conservation of energy. In the same year, Pauli proposed that an additional particle which is extremely light and electrically neutral is simultaneously emitted in beta decay as depicted in figure 1.3. Considering the decay products as a

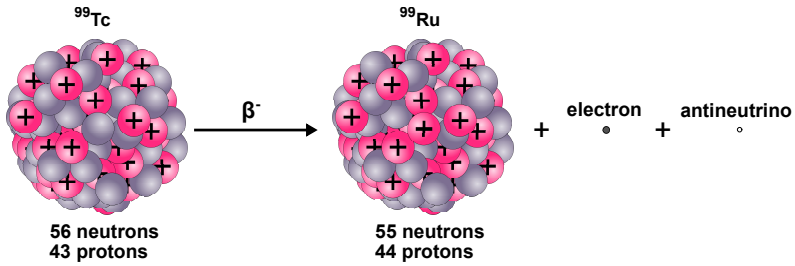

Figure 1.3: Schematic nuclear beta decay of ^{99}Tc to ^{99}Ru.

three-body-problem explained the continuous nature of the energy distribution of the detected electrons, see A.1. The elusive particle was later named *neutrino* by Fermi who was able to develop a successful theory of beta decay [Fer34]. The existence of neutrinos was confirmed several years later by the celebrated experiment of Cowan and Reines [Cow56].

Beta spectra are typically measured with methods that determine the kinetic energy of the emitted electron and that employ semiconductor detectors [Sin19, Sin20], scintillation devices or magnetic spectrometers [Kos19]. These methods suffer from rather low energy resolutions and the measurement of low-energy electrons is difficult due to absorption and attenuation effects within sources and dead layers of detectors. However, accurate measurements of beta spectra with low maximum energy or the low-energy part of beta spectra with higher end-point energy are of highest importance within radionuclide metrology, see e.g. [Kos11, Kos15, Kos18].

Radionuclide metrology is concerned with determining the activity, half-life, energy levels and decay mode probabilities of radionuclides as accurately and precisely as possible [Pom07]. The derived SI unit of (radio)activity is the becquerel [Bq]=1/s, which is defined as the number of nuclear decays per second. Its realization is achieved with primary activity methods which detect the emitted radiation of the radionuclide sample. In principle, determining the activity of a sample is just a counting process. Realizing this task on a metrological level, however, requires very precise and elaborate detection methods since radionuclides have highly individual emission properties. In particular, this has shown to be true when determining the activity of beta emitting isotopes by means of liquid scintillation counting [Bro07], Cherenkov counting [Kos14] or classical microcalorimetry [Col07].

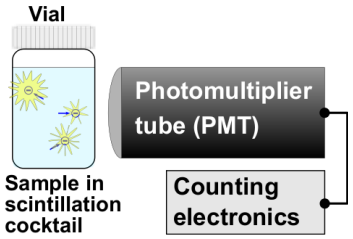

Figure 1.4: Schematic liquid scintillation setup.

Accurate beta spectra measurements are also indispensable for sound validations of theoretical models and corresponding improvements of calculation methods [Mou14, Mou15, Mou16], respectively. Beta spectra are also relevant for fundamental research, e.g. due to the relation between beta and neutrino spectra as shown in Mougeot [Mou15] and for consideration in radioactive waste management [Nic06] as well as for applications in nuclear medicine [Bar94].

In this work, the beta spectrum of ^{99}Tc is measured with an MMC[1], which is a cryogenic detector that is able to measure small amounts of radiation very precisely [Ban93, Fle05, Kem18]. The detection principle is based on the strong temperature dependence of the magnetic susceptibility of a paramagnet (Au:Er$_x$ or Ag:Er$_x$, $x \sim 300\,\mathrm{ppm}$). The paramagnet is held in an induced magnetic field and in thermal contact with a gold absorber. When the latter changes its temperature, e.g. via

[1]MMC = Metallic Magnetic Calorimeter

energy deposition of alpha, beta or gamma radiation, the resulting change in magnetization of the paramagnet can be read out with a SQUID[2] [Dru07]. MMCs with the sample embedded in 4π solid angle absorbers have shown to be among the best beta spectrometers. Although the embedding is labor intensive and technically challenging, the result is a detector with a quantum efficiency of almost 100%, an excellent energy resolution over the entire spectral energy range and a very low energy threshold [Rot07, Rot08, Loi10, Loi14, Loi19, Loi20].

The thesis is organized as follows. Chapter 2 briefly summarizes the theory of nuclear beta decay and the classification of beta transitions. In particular, the strong demand for high precision beta spectrum measurements motivated by primary activity determinations in radionuclide metrology with a focus on advanced liquid scintillation counting methods is described. In chapter 3, an overview of the physical principles and properties of MMCs is given. Details on the experimental setup i.e. the MMC-based beta spectrometer that was used for the measurements is provided in chapter 4. The measurement results and analysis are provided in chapter 5, where a new spectrum of the second forbidden non-unique beta emitter ^{99}Tc is presented and compared to literature and state-of-the-art theory. In the second part of the chapter, the problem of suboptimal quantum efficiency in beta spectrometers is addressed. The cause can be an insufficient absorber geometry ($< 4\pi$) or energy detection losses generated by high energy beta emitters such as ^{36}Cl ($Q^- = 709.5\,\mathrm{keV}$). In such cases, the resulting beta spectrum distortions can be efficiently corrected with a novel algorithm that relies on extensive Monte Carlo simulations. A summary of the thesis is given in chapter 6.

[2]SQUID = Superconducting QUantum Interference Device

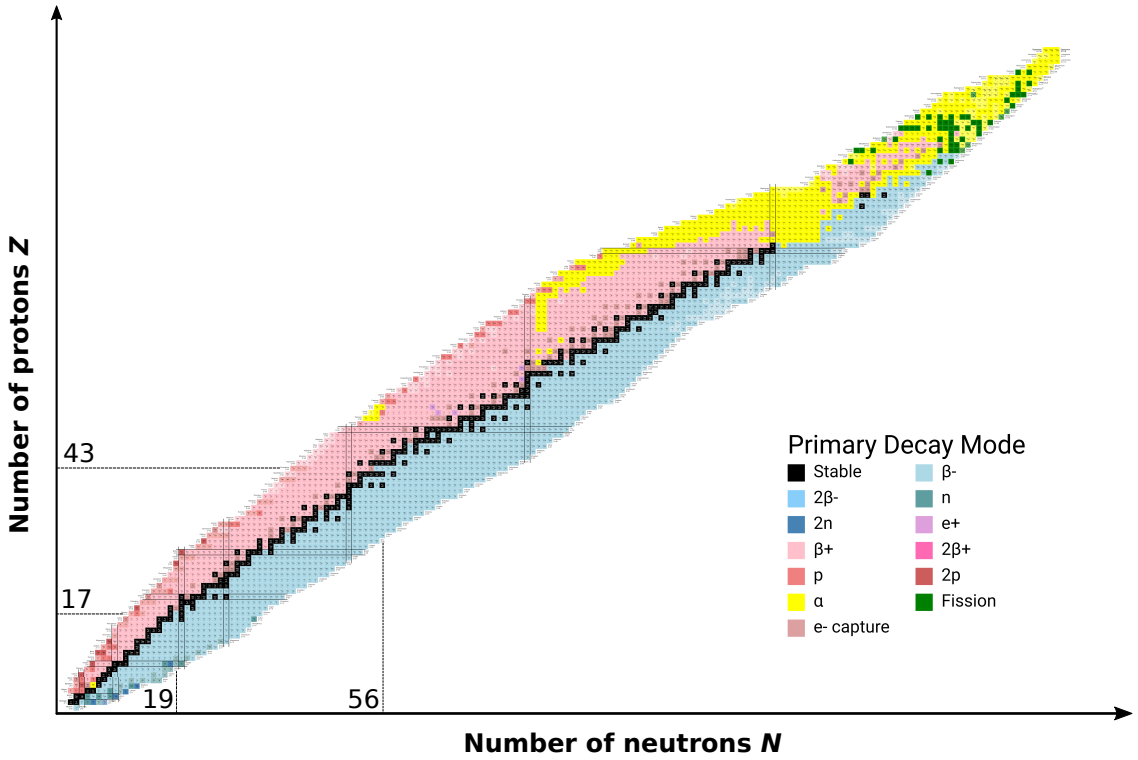

Figure 1.5: A current chart of radionuclides, generated at [Sim21], where the added lines indicate the positions of ^{99}Tc and ^{36}Cl.

Acknowledgements

I thank my thesis advisor Christian Enss for the opportunity to pursue a very interesting topic in cryogenic microcalorimetry at the Heidelberg Graduate School for Physics. The co-advisors Sebastian Kempf and Andreas Fleischmann gave most valuable advice which improved the quality of the thesis.

The thesis work was carried out at the Physikalisch-Technische Bundesanstalt (PTB) which is the national metrology institute of the Federal Republic of Germany. The generous guidance of my PhD advisor Karsten Kossert at the PTB Braunschweig concerning beta spectrometry and the excellent suggestion to develop an unfolding algorithm for external bremsstrahlung effects in microcalorimeters, is most gratefully acknowledged. Furthermore, I thank Jörn Beyer at the PTB Berlin for all of the fascinating and productive discussions while being a superlative PhD mentor.

Concerning the sample preparation and initial measurements with the MMC beta spectrometry setup, I thank the postdoctoral researchers Lina Bockhorn and Philipp Ranitzsch for the generous co-operation and supportive cameraderie. In the latter half of the thesis I greatly benefited from Philipp's expertise in optimizing MMC measurements and evaluating a data set to the fullest.

Dirk Arnold, Ole Nähle, Jörn Beyer and Thomas Schurig along with the colleagues at the PTB Departments 6.1 Ionizing Radiation and 7.6 Cryosensors have been very supportive, during physical and metaphysical events, for which I am very thankful.

This work was performed as part of the EMPIR[3] Projects 15SIB10 MetroBeta and 17FUN02 MetroMMC. The projects have received funding from the EMPIR programme co-financed by the Participating States and from the European Union Horizon 2020 research and innovation programme. Co-authors and project partners: merci tout le monde! I very much look forward to continuing our efforts within PrimA-LTD.

Last but not least, I thank my dear family and friends for their great love, cheerful encouragement and tolerant patience.

[3]EMPIR = The European Metrology Programme for Innovation and Research

2
Motivation

According to the BIPM[1] [Qui97]: *"A primary method of measurement is a method having the highest metrological qualities, whose operation can be completely described and understood, for which a complete uncertainty statement can be written down in terms of SI units, and whose results are, therefore, accepted without reference to a standard of the quantity being measured."*

A well-known primary measurement method to determine the temperature is the constant volume thermometer which is based on the real gas law:

$$pV = Nk_{\mathrm{B}}T\left[1 + B(T)\frac{N}{V} + C(T)\left(\frac{N}{V}\right)^2 + \dots\right], \tag{2.1}$$

where p denotes the pressure, V the volume, N the number of gas particles, k_{B} the Boltzmann constant, T the temperature such that $B(T)$ and $C(T)$ are the first and second virial coefficients, respectively. This kind of gas thermometer is still considered primary although the virial coefficients are temperature dependent since they are well-known via other experiments, negligible under low-pressure conditions or can be theoretically calculated with very high precision.

When it comes to the primary activity determination of radionuclides, the methods are diverse and optimized for the type of decay that is under study [Pom07]. While current techniques have great sensitivity to the detection of emitted particles, they are not overly accurate and uncertainties of less than 1% are considered very accurate [Mal20]. In the case of beta emitters one uses highly developed methods such as liquid scintillation or Cherenkov counting and classical microcalorimetry. Having several,

[1]BIPM = Bureau International des Poids et Mesures, mother organization of national metrology institutes (NMIs)

well-developed techniques to determine a quantity is an advantage as one may validate measurement results and find systematic errors in measurement setups. The quantity to be determined in the aforementioned counting methods is the activity concentration a of a sample which is defined as

$$a = \frac{R_{\text{net}}}{\epsilon\,(S) \cdot m}, \quad [a] = \frac{\text{Bq}}{\text{kg}}, \tag{2.2}$$

where R_{net} is the net counting rate, ϵ the a priori unknown counting efficiency, S the beta spectrum and m is the mass of the sample.

Notably, to calculate the counting efficiency ϵ correctly one needs accurate knowledge of the entire beta spectrum S which will be clarified in section 2.2. Next to determining the activity concentration of a radionuclide itself or equivalently its half-life, measuring specific samples which in practice are handled as solutions is an important task in radionuclide metrology. This involves establishing measurement standards[2] which are utilized for detector calibration and metrological traceability[3]. Before the modern primary activity determination methods for beta emitters are described in closer detail, the physical theory of beta decay [Suh07] is presented in the following.

2.1 Beta decay

According to the *standard model* of electroweak interactions by Glashow, Weinberg and Salam [Gla70, Wei67, Sal68], beta decay modes result from the possible conservations of

i) electric charge $q \in \{0, +e, -e\}$,

ii) lepton number $L \in \{+1 \text{ for leptons}, -1 \text{ for antileptons}\}$, where each lepton flavour electron, muon and tau has its own lepton number that is conserved and

iii) baryon number $B \in \{+1 \text{ for baryons}, -1 \text{ for antibaryons}\}$.

Thus, for the fermions involved in beta decay one has the following table.

[2][BIP12, 2.41]: *realization of the definition of a given quantity, with stated quantity value and associated measurement uncertainty, used as a reference.*

[3][BIP12, 5.1]: *property of a measurement result whereby the result can be related to a reference through a documented unbroken chain of calibrations, each contributing to the measurement uncertainty.*

Table 2.1: Beta decay according to the standard model.

Particle	q	B	L	m **in MeV/c^2**
electron (e^-)	$-e$	0	+1	0.511
positron (e^+)	$+e$	0	-1	0.511
electron neutrino (ν_{e^-})	0	0	+1	0
electron antineutrino ($\overline{\nu}_{e^-}$)	0	0	-1	0
proton (p)	$+e$	+1	0	938.3
neutron (n)	0	+1	0	939.6

In the standard model, ν_{e^-} and $\overline{\nu}_{e^-}$ are *Dirac neutrinos* that have zero mass. This is in contrast with the so called *Majorana neutrinos* which are proposed by more elaborate models within grand unified and supersymmetric theories. Such neutrinos have a non-zero mass and are their own antiparticle i.e. $\nu = \overline{\nu}$. Furthermore, lepton number conservation may be violated which leads to lepton flavour oscillations. Several large-scale neutrino experiments e.g. Super-Kamiokande [Fuk01], SNO [Ahm02] and KamLAND [Egu03] have demonstrated violations of lepton flavour conservation, which means that electron, muon and tau flavours transform into each other. This is only possible if at least one of the neutrino mass eigenstates describes a non-zero mass, which indicates a positive mass for the neutrino.

Recently, the upper bound for the electron antineutrino mass was measured to 1.1 eV in the KATRIN project via the beta decay of ^{3}H [Ake19]. The ECHo [Gas14, Vel20] and HOLMES [Alp15] collaborations aim to measure the mass of the electron neutrino via the electron capture of ^{163}Ho, using MMC [Kem18] and TES[4] [Irw05] detectors, respectively. Lepton flavour oscillations also allows for exotic decay modes such as neutrinoless double beta decay or muon to electron conversion.

In the following, we will concentrate on β^- decay as the radionuclides addressed in this work mainly decay in that manner. The process of β^- decay can be described as in figure 2.1, in the *impulse approximation*, using a Feynman diagram in which only one nucleon takes part in the weak decay process and the other $A-1$ nucleons act as spectators.

[4]TES = Transition-Edge Sensor

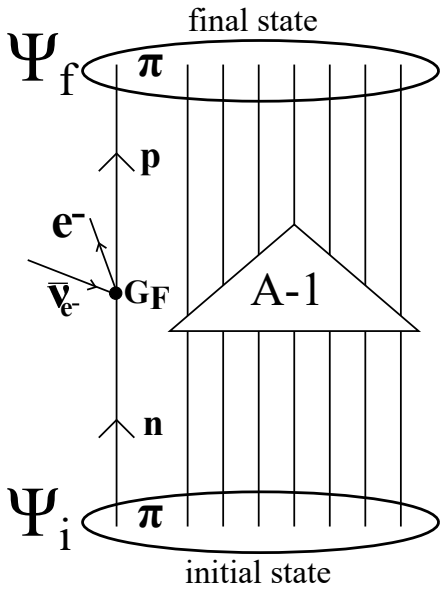

Figure 2.1: Feynman diagram of nuclear β^- decay.

The so-called nucleon current or weak hadronic current is described by the flow lines of the nucleons. At the weak interaction vertex, the weak hadronic current interacts with the weak leptonic current. The antiparticle lines are drawn as going backwards in time and G_F is called the Fermi effective decay strength constant that incorporates the exchange vector boson W^-.

More precisely, when the neutron decays into a proton a negatively charged W boson of mass $m_W = 80\,\mathrm{GeV/c^2}$ is emitted, as depicted in figure 2.2, its large mass causes

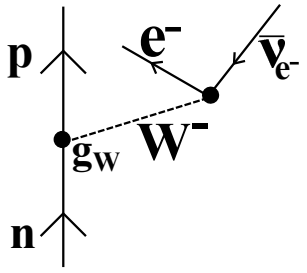

Figure 2.2: Feynman diagram of β^- decay.

it to decay very quickly into an electron and antineutrino with coupling strength g_W. The process is called a current-current interaction. As a result of the large mass of the W^- boson and the relatively small energy of the beta decay, the effective coupling constant can be expressed as

$$G_F = \frac{g_W^2}{8(m_W c^2)^2}. \tag{2.3}$$

There are three types of beta decay which are compatible with the conservation laws of the standard model [Suh07]:

$$\begin{array}{rcll} \beta^- \text{ decay} & : & \mathrm{n} & \rightarrow \mathrm{p} + \mathrm{e}^- + \overline{\nu}_\mathrm{e} \\ \beta^+ \text{ decay} & : & \mathrm{p} & \rightarrow \mathrm{n} + e^+ + \nu_\mathrm{e} \\ \text{electron capture (EC)} & : & \mathrm{p} + \mathrm{e}^- & \rightarrow \mathrm{n} + \nu_\mathrm{e} \end{array}$$

where n denotes a *neutron*, p a *proton*, $\mathrm{e}^-/\mathrm{e}^+$ an *electron/positron* and $\overline{\nu}_\mathrm{e}/\nu_\mathrm{e}$ an *electron antineutrino/neutrino*. Within approximately 15 minutes [Cza18] a free neutron will undergo β^- decay, whereas β^+ decay and EC may only occur if extra energy is supported such as in a nuclear environment. The corresponding nuclear processes can thus be described by

$$\begin{array}{ll} \text{(Z,N)} & \overset{\beta^-}{\rightarrow} \text{(Z+1,N-1)} + \mathrm{e}^- + \overline{\nu}_\mathrm{e} \\ \text{(Z,N)} & \overset{\beta^+}{\rightarrow} \text{(Z-1,N+1)} + \mathrm{e}^+ + \nu_\mathrm{e} \\ \text{(Z,N)} + \mathrm{e}^- & \overset{\mathrm{EC}}{\rightarrow} \text{(Z-1,N+1)} + \nu_\mathrm{e} \end{array}$$

where Z and N denote the number of protons and neutrons, respectively.

2.1.1 Allowed and forbidden transitions

When the recoil energy is not considered, the energy of a β^- decay is given by

$$E_\mathrm{max} = Q^- - E_i, \tag{2.4}$$

where $Q^- = m_\mathrm{parent} - m_\mathrm{daughter}$ denotes the energy of the disintegration and E_i the energy of the level to which the decay occurs. Beta transitions can be categorized according to the angular momentum of the particles that are emitted in the nuclear decay. The initial and final nuclear states have total angular momentum quantum numbers J_i and J_f, respectively. The emitted electron-neutrino pair may have an orbital angular momentum quantum number $L_\beta \in \{0, 1, 2, \ldots\}$ and an intrinsic spin quantum number S_β of -1, 0 or 1. Conservation of angular momentum implies that

$$\Delta J := |J_i - J_f|\,, \quad \text{where} \quad J_i - J_f = L_\beta + S_\beta \tag{2.5}$$

with the parity relationship

$$\pi_i \pi_f = (-1)^{L_\beta}\,. \tag{2.6}$$

If $L_\beta = 0$ i.e. if the emitted particles carry no angular momentum, the transition is called *allowed* and if $L_\beta = n$ it is called *forbidden*[5] of order n.

Forbidden transitions are further classified according to the phenomenologically de-

[5]Despite its name, forbidden transitions may occur but tend to be less probable than allowed transitions.

fined ft value [Beh82, Gro89], where f is the phase-space factor given by

$$f = \int_1^{W_{\max}} pW_{\max} F\left(\pm Z, W\right) \mathrm{d}W \tag{2.7}$$

where $W_{\max}$ is the maximum energy of the beta particle, p its momentum, F the Fermi function and $t = t_{1/2}$ is the experimental half-life. Such transitions are called *unique* if a single multipole term along with *one* transition operator contributes to f. In other cases, the forbidden transition is said to be *non-unique*.

Table 2.2: Types of β^- decay.

Transition	**Forbiddedness order**	ΔJ	$\pi_i \pi_f$	**Nuclide ex.**
Super-allowed	-	0	+1	^{3}H
Allowed	-	0,+1	+1	^{14}C
Forbidden unique	1	± 2	-1	^{198}Au
	2	± 3	+1	^{60}Co
	3	± 4	-1	^{40}K
	4	± 5	+1	-
	$(\Delta J - 1) : th$	> 1	$(-1)^{\Delta J - 1}$	-
Forbidden non-unique	1	$0, \pm 1$	-1	^{86}Rb
	2	± 2	+1	^{36}Cl, ^{99}Tc
	3	± 3	-1	^{87}Rb
	4	± 4	+1	^{113}Cd
	$\Delta J : th$	> 1	$(-1)^{\Delta J}$	-

2.1.2 Theoretical beta spectrum shapes

The beta spectrum shape N i.e. the number of emitted beta particles with energy W in the interval $[W, W + \mathrm{dW}]$ per unit time, can be described as [Mou15, Sin20]

$$N(W)\mathrm{d}W \sim pWq^2 F_{\mathrm{Beh}}(Z, W) C(W) S(Z, W) R(Z, W) \mathrm{d}W, \tag{2.8}$$

where $p = \sqrt{W^2 - 1}$ is the momentum of the beta particle, $q = W_{\max} - W$ is the momentum of the neutrino (assumed to be massless), $F_{\mathrm{Beh}}(Z, W)$ is the Fermi function in the sense of Behrens [Beh76, Beh82, Mou15] for the static Coulomb field of the nucleus, $C(W)$ is the shape factor that describes the coupling of the nuclear structure to the lepton dynamics. Additionally, $S(Z, W)$ and $R(Z, W)$ denote atomic screening and radiative correction functions [Mou15] that take into account the interaction of the emitted beta particle with the electron shell of the atom and non-static Coulomb effects, respectively. Since beta particles have a rest mass of only 511 keV, their dynamics needs to be treated relativistically and thus the corresponding wave functions needed

to define the Fermi function are found by solving the corresponding Dirac equation.

Unique forbidden transitions have theoretical shape factors that can be evaluated as a function of the energy. The theoretical shape factors of non-unique forbidden transitions, in contrast, cannot be directly evaluated as various nuclear matrix elements of their Fermi functions are unknown [Mou15]. However, an overview of experimental beta spectrum shapes for the second forbidden non-unique beta transitions of ^{99}Tc and ^{36}Cl found in the literature is given in section 2.3 below.

2.2 Primary activity determination for beta emitting radionuclides

The activity A of a radionuclide is defined as the number of decays that occur in a specific time frame. Its unit is the becquerel (Bq), where

$$1\,\mathrm{Bq} := 1\,\frac{\text{decay}}{\text{second}} \quad \text{[SI-unit of activity]}. \tag{2.9}$$

Although nuclear decay is quite complicated on a microscopic level, it follows comparably simple statistical laws for macroscopic samples [Rut03]. The number ΔN of nuclei decaying in a given time Δt is directly proportional to the current number N of active nuclei:

$$\frac{\Delta N}{\Delta t} = -\kappa N, \tag{2.10}$$

or in differential form

$$\frac{\mathrm{d}N}{\mathrm{d}t} = -\kappa N, \quad \text{yielding the exponential law} \quad N(t) = N_0 e^{-\kappa t}, \tag{2.11}$$

where κ is the radionuclide specific decay constant[6] and $N(0) = N_0$. Due to its exponential nature, it is practical to describe the activity of a sample via its half-life i.e. the approximately constant time it takes for half of the remaining sample to decay, which may easily be derived by the above as

$$t_{1/2} = \frac{\ln 2}{\kappa}. \tag{2.12}$$

It should be noted that the decay rate is a radionuclide specific quantity which has to be determined on a case by case basis with precise measurements. When the decay rate of a radionuclide, or equivalently its half-life, has been established, one may apply it for radiometric dating (see appendix A.2), nuclear forensics or detector calibration [Pom15].

[6] Doubts have been raised from time to time whether the decay rate is actually constant. A recent paper gives excellent proof that this is a very reasonable approximation for macroscopic samples [Pom18].

2.2.1 Liquid scintillation counting methods

Determining the activity with very high precision and accuracy requires elaborate experimental setups and a very good estimate of the counting efficiency [LAn03]. Currently, the dominating technique for metrological activity measurements of beta emitters is Liquid Scintillation Counting (LSC). The relevant quantity to be determined is the activity concentration a of a sample which is given by

$$a = \frac{R_{\text{net}}}{\epsilon(S) \cdot m}, \quad [a] = \frac{Bq}{kg}, \tag{2.13}$$

where R_{net} is the net counting rate, $\epsilon \in [0, 1]$ the a priori unknown counting efficiency, S the normalized beta spectrum and m is the mass of the sample.

LSC techniques were developed [Kal50, Rey50] after it was discovered that aromatic fluor compounds may convert absorbed energy of nuclear radiation into light photons [Her49]. The fluorescence i.e. the emission of photons as the result of atomic excitation is detected using a photo multiplier tube (PMT). When the photons reach the photocathode of the PMT, electrons are generated at the photocathode via the photoelectric effect and multiplied at the dynodes. The resulting electrodes are collected at the anode of the PMT and detected as a change in current. This serves as the physical principle behind LSC. Typically, the radionuclide sample is placed in a glass or plastic container called the scintillation vial and an appropriate liquid scintillation cocktail, consisting of an organic solvent and scintillator molecules, is added. The intensity of the emitted light flashes is directly proportional to the energy of the nuclear decay while the number of light flashes per unit time corresponds to the activity of the radionuclide sample.

In principle, LSC for beta emitters is a high geometry method i.e. the solid angle for the decays is very close to 4π as the electrons emitted by the radionuclide transfer practically their complete energy to the solvent, with exception of decays that occur very close to the walls of the vials. Thus, almost every decay gives rise to photons in the scintillator which can be detected by the PMTs.

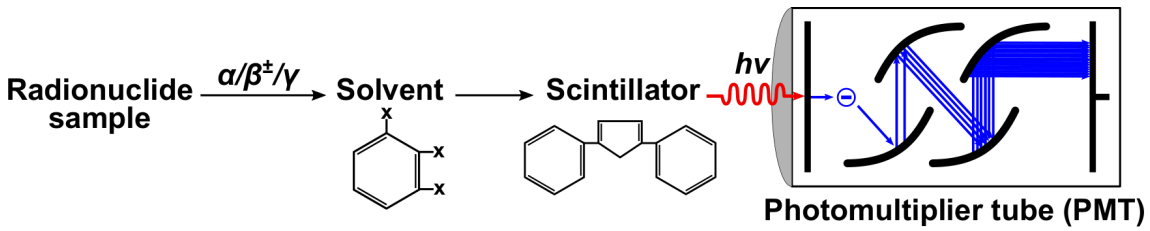

Figure 2.3: Illustration of the liquid scintillation counting principle. The more energy a beta particle has, the longer its path will be in the scintillation cocktail. Along its path, solvent molecules will absorb a large part of the energy and excite scintillator molecules which each emits a photon of a characteristic wavelength. Typical wavelengths are in the range of ultraviolet to blue light. The scintillator molecule above is 2,5-diphenyloxazole, which emits photons with a wavelength of 357 nm [Per22].

Energy transfer

The emitted light from the scintillation cocktail heavily depends on the type of nuclear decay that occurs in the radioactive sample. Alpha particles have a much shorter linear range (0.048 mm, ^{241}Am, 5.5 MeV) compared to beta particles (17.8 mm, ^{10}Be, 0.55 MeV). A beta particle generates ~ 10 scintillation photons which are then detected at one or several of the PMTs. Beta particles with energies higher than 263 keV can be detected using clear aqueous solutions via the Cherenkov effect: charged particles can travel relatively faster than light in certain media such as water, plastic or glass which produces Cherenkov photons in the UV to visible light region. Gamma particles can typically be detected directly by the PMTs and need not rely on the scintillation effect.

Quenching issues

There are various chemical and physical processes that may lead to a reduction of photon yield in the scintillator, this phenomenon is called quenching and needs to be carefully quantified for precision measurements. The presence of unwanted chemicals such as organic acids or dissolved oxygen, e.g. due to sample impurities, may lead to the production of heat instead of light when there is a decay. Colored substances cause an anisotropy of the emitted light while ionization quenching occurs when the ionization density along the track of a charged particle is high.

In general, the light emission L is a non-linear function of the energy of the decay E. The semi-empirical Birks formula for the specific fluorescence light emission is given by

$$\frac{\mathrm{d}L}{\mathrm{d}x} = \frac{\eta_0 \frac{\mathrm{d}E}{\mathrm{d}x}}{1 + kB(\frac{\mathrm{d}E}{\mathrm{d}x})}, \quad [kB]=\frac{\mathrm{g}}{\mathrm{MeV}\cdot\mathrm{cm}^2} \tag{2.14}$$

where η_0 is the scintillation efficiency (photons emitted per unit of energy), $\frac{\mathrm{d}E}{\mathrm{d}x}$ denotes the stopping power of the incident particle and kB is *Birks parameter*[7] (the ionizing quenching parameter). Via integration over the energy range $[0, E]$, one arrives at the fluorescent yield of the scintillator:

$$L(E) = \eta_0 \int_0^E \frac{\mathrm{d}E}{1 + kB(\frac{\mathrm{d}E}{\mathrm{d}x})} = \eta_0 E Q(E), \tag{2.15}$$

where Q denotes the ionizing quenching function

$$Q(E) := \frac{1}{E} \int_0^E \frac{\mathrm{d}E}{1 + kB\left(\frac{\mathrm{d}E}{\mathrm{d}x}\right)}. \tag{2.16}$$

[7] If the reader thinks the common notation kB is unfortunate due to its similarity to the Boltzmann constant k_B, the author is inclined to agree.

Coincidence counting

PMTs suffer from intrinsic and rather large unstable thermal noise. In the early days, one PMT was used for activity determination but this limited the precision due to dark count rates and background events. If at least two are utilized, which is the case in most state-of-the-art commercial LSC setups, coincidence counting greatly reduces these effects. Within the family of LSC techniques for activity determination the CNET[8] and TDCR[9] methods are prominently used in national metrology labs for activity standardization of beta emitters [Bro07]. Both methods are based on the same underlying free-parameter model, which is determined using the measured data and yields a very good estimate for the counting efficiency.

Table 2.3: Coincidence counting probabilities.

R:	**Operation mode**	**Signal**	**Counting probability** $P(E,\lambda)$
1	A	U	$(1-p_{\bar{A}})$
2	A; B	U	$(1-p_{\bar{A}})$; $(1-p_{\bar{B}})$
	A + B	S	$(1-p_{\bar{A}}p_{\bar{B}})$
	AB	D	$(1-p_{\bar{A}})(1-p_{\bar{B}})$
3	A; B; C	U	$(1-p_{\bar{A}})$; $(1-p_{\bar{B}})$; $(1-p_{\bar{C}})$
	A+B; B+C; A+C	S_2	$1-p_{\bar{A}}p_{\bar{B}}$; $1-p_{\bar{B}}p_{\bar{C}}$; $1-p_{\bar{A}}p_{\bar{C}}$
	A+B+C	S_3	$1-p_{\bar{A}}p_{\bar{B}}p_{\bar{C}}$
	AB; BC; AC	D	$(1-p_{\bar{A}})(1-p_{\bar{B}})$; $(1-p_{\bar{B}})(1-p_{\bar{C}})$; $(1-p_{\bar{A}})(1-p_{\bar{C}})$
	AB+BC	D_2	$(1-p_{\bar{A}})(1-p_{\bar{B}})+(1-p_{\bar{B}})(1-p_{\bar{C}})$ $-(1-p_{\bar{A}})(1-p_{\bar{B}})(1-p_{\bar{C}})$
	AB+AC		$(1-p_{\bar{A}})(1-p_{\bar{B}})+(1-p_{\bar{A}})(1-p_{\bar{C}})$ $-(1-p_{\bar{A}})(1-p_{\bar{B}})(1-p_{\bar{C}})$
	BC+AC		$(1-p_{\bar{B}})(1-p_{\bar{C}})+(1-p_{\bar{A}})(1-p_{\bar{C}})$ $-(1-p_{\bar{A}})(1-p_{\bar{B}})(1-p_{\bar{C}})$
	AB+BC+AC	D_3	$(1-p_{\bar{A}})(1-p_{\bar{B}})+(1-p_{\bar{B}})(1-p_{\bar{C}})$ $+(1-p_{\bar{A}})(1-p_{\bar{C}})$ $-2(1-p_{\bar{A}})(1-p_{\bar{B}})(1-p_{\bar{C}})$
	ABC	T	$(1-p_{\bar{A}})(1-p_{\bar{B}})(1-p_{\bar{C}})$

[8]CNET = CIEMAT/NIST efficiency tracing, where CIEMAT = El Centro de Investigaciones Energéticas, Medioambientales y Tecnológicas, NIST = National Institute of Standards and Technology i.e. the NMIs of Spain and the USA

[9]TDCR = Triple-to-Double Coincidence Ratio

The free parameter model

The free parameter is defined as the energy λ which is needed to create a photoelectron at the photocathode of the PMT:

$$\lambda := \frac{E\,Q(E)}{\overline{m}(E)}, \tag{2.17}$$

where E is the energy of the nuclear decay, Q is the ionization quenching function and $\bar{m}$ is the mean number of photons released.

For a radionuclide sample which decays purely by beta decay, the efficiency ϕ is given by

$$\phi(\lambda) = \int_0^{E_{\max}} S(E)P(E,\lambda)\mathrm{d}E, \tag{2.18}$$

where $E_{\max}$ is the maximum energy of the decay, $S(E)$ is the normalized beta spectrum such that

$$\int_0^{E_{\max}} S(E)\mathrm{d}E = 1 \tag{2.19}$$

and $P(E,\lambda)$ is the coincidence counting probability for the energy.

In the free parameter model, the following additional assumptions [Bro07, Nuc21] are made. While being very realistic they allow for calculating the coincidence counting probabilities $P(E,\lambda)$ in closed form.

A1) **Particle statistics**: The number of photons that are emitted when an electron of energy E interacts with the scintillator is Poisson distributed with mean

$$N = \frac{LQ(E)E}{h\nu}, \tag{2.20}$$

where L denotes the energy conversion factor, Q is the ionizing quenching function in (2.16) and $h\nu$ is the energy of the photons. Also, the number of photons X reaching the photocathodes of all PMTs is Poisson distributed with mean $\overline{n}$:

$$\mathbb{P}\left(\mathbb{X} = n\right) = \overline{n}^n \frac{e^{-\overline{n}}}{n!}, \tag{2.21}$$

where $\overline{n} = N\xi$ and ξ is the geometric detection efficiency of the PMTs.

The photons within the optical chamber follow a multinomial distribution i.e. for R PMTs in the setup and K impacting photons such that $K = K_1 + \ldots + K_R$ and K_i photons reach the PMT indexed by i, the configuration of these photons is multinomially distributed:

$$\mathbb{P}\left(K_1 = k_1, \ldots, K_R = k_R\right) = \frac{1}{R^k}\frac{k!}{k_1! \ldots k_R!}, \qquad \text{for } k = k_1 + \ldots + k_R. \tag{2.22}$$

The number of photoelectrons M generated within a PMT due to the impact of n photons is binomially distributed i.e.

$$\mathbb{P}\left(M=m\right)=\frac{n!}{m!(n-m)!}p^m(1-p)^{n-m} \qquad \text{where } p=\epsilon_q\mu, \tag{2.23}$$

ϵ_q is the quantum efficiency of the photocathode and μ is the spectral matching factor between the fluorescence spectrum and the spectral response of the photocathode. Notably, the total cascade of particles described by (2.21)-(2.23) implies that the number of photoelectrons created is Poisson distributed with mean

$$\overline{m}=N\epsilon_{\text{opt}}, \tag{2.24}$$

where ϵ_{opt} denotes the optical efficiency of the LSC setup and $\epsilon_{\text{opt}}=\xi\epsilon_q\mu$.

A2) **Non-linear energy dependence:** The mean number of photoelectrons $\overline{m}$ that are created in the PMT of the LSC is a non-linear function of the decay energy:

$$\overline{m}(E)=\frac{EQ(E)}{\lambda}\overset{(2.16)}{=}\frac{1}{\lambda}\int_0^E\frac{\mathrm{d}E}{1+kB\left(\frac{\mathrm{d}E}{\mathrm{d}x}\right)}. \tag{2.25}$$

A3) **Detection threshold of the setup:** Given a beta decay within the radionuclide sample, the probability of counting at least one photon with the PMT A is assumed to be non-zero and is equal to the complementary probability of detecting zero photons:

$$P(E,\lambda_A)=1-p_{\bar{A}}\overset{(2.24)}{=}1-\mathbb{P}\left(M_A=0\right)=1-e^{-\frac{\overline{m}_A}{R}}\overset{(2.25)}{=}1-e^{-\frac{EQ(E)}{R\cdot\lambda_A}}, \tag{2.26}$$

which follows from the Poisson property of the number of photoelectrons (2.24) and where R is the total number of PMTs in the LSC setup and λ_A denotes the free parameter of PMT A.

The idea of CNET is to perform relative activity measurements of a second standardized radionuclide, the so called tracer, while TDCR is an absolute method. While the CNET can readily be done with commercial setups that typically have two PMTs, TDCR requires a dedicated setup with three PMTs. The two methods will now be described in closer detail.

The CNET method

A CNET setup consists of a vial containing the radionuclide sample along with a liquid solvent and the scintillator chemicals which is placed in front of two PMTs. The method [Mal82] involves the following calculation and measurement steps, as depicted in figure 2.4.

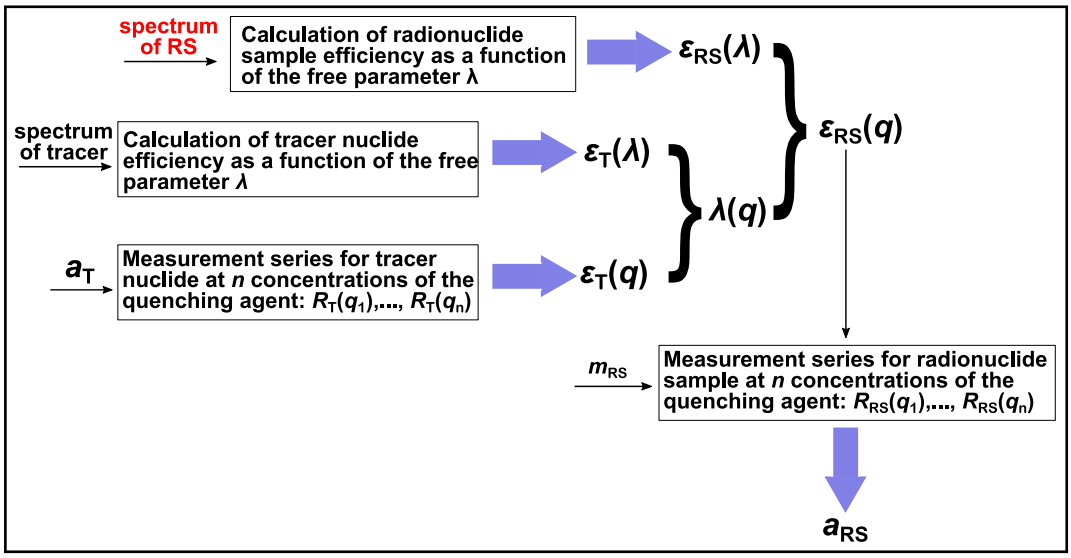

Figure 2.4: Overview of the CNET method.

Firstly, one calculates the efficiency as a function of the free parameter λ for $R = 2$ according to the formula (2.18) and table 2.3, respectively. This is done for the radionuclide under study (RS), as well as for a tracer nuclide (T), which is usually ^{3}H as its beta spectrum is super-allowed and well-understood, see table 2.2. The calculations yield the counting efficiencies of RS denoted $\epsilon_{\mathrm{RS}}(\lambda)$ and that of the tracer, denoted $\epsilon_{\mathrm{T}}(\lambda)$.

Next, the counting efficiency of the tracer is measured as a function of the quenching indicator q in several steps: e.g. ten vials are prepared containing the scintillation cocktail along with a fixed amount of tracer standard solution of well-known activity. The first vial is measured *as is* and starting from vial two an increasing amount of quenching agent is added to decrease the counting efficiency. The activity of each vial is measured and since the activity of the tracer *Urlösung* was well known, this yields the counting efficiency of the tracer as a function of the quenching indicator i.e. $\epsilon_{\mathrm{T}}(q)$. From this function, using the calculated efficiency of the tracer $\epsilon_{\mathrm{T}}(\lambda)$, the free parameter as a function of the quenching agent amount $\lambda(q)$ can be inferred. Combining this information with the calculated efficiency for RS as a function of the free parameter, one arrives at the efficiency of RS as a function of the quenching agent amount: $\epsilon_{\mathrm{RS}}(q)$.

Following these procedures, an equivalent measurement series with ideally identical geometry and quenching agent amounts for the RS is done and the counting rates are recorded. From the mass of the RS, the efficiency function $\epsilon_{\mathrm{RS}}(q)$ and the recorded counting rates as a function of the quenching agent amounts, one finally arrives at the activity concentration a_{RS}.

The TDCR method

A schematic of a TDCR setup [Sch66, Poc88] as they are widely employed at NMIs is depicted in figure 2.5. It consists of a sample vial surrounded by three symmetrically positioned PMTs which are connected to a so called MAC3[10] electronics module [Bou00] with a resolving time of 40 ns.

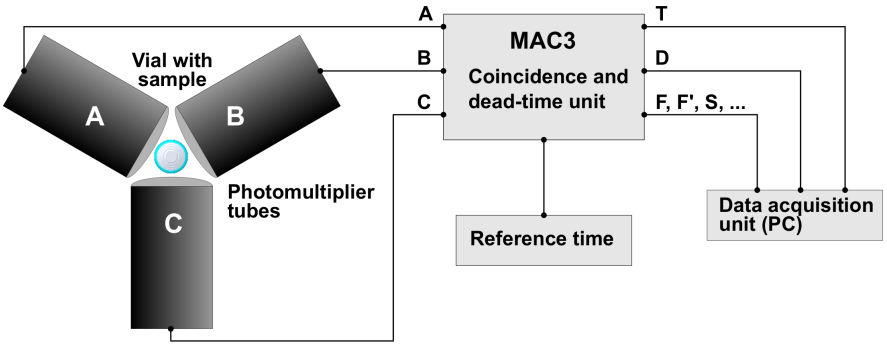

Figure 2.5: Schematic TDCR measurement setup.

Now, by measuring the double and triple coincidences one arrives at a system of equations from which the free parameter of each PMT and thus the efficiency can be calculated. From (2.26), the definition of the free parameter (2.17) and table 2.3, it follows that the ratio of triple over double counting efficiencies can be expressed as

$$\begin{cases} \frac{\phi_{ABC}}{\phi_{AB}} = \frac{\int_0^{E_{\max}} S(E)P(E,\lambda_A)P(E,\lambda_B)P(E,\lambda_C)\mathrm{d}E}{\int_0^{E_{\max}} S(E)P(E,\lambda_A)P(E,\lambda_B)\mathrm{d}E}, \\ \frac{\phi_{ABC}}{\phi_{BC}} = \frac{\int_0^{E_{\max}} S(E)P(E,\lambda_A)P(E,\lambda_B)P(E,\lambda_C)\mathrm{d}E}{\int_0^{E_{\max}} S(E)P(E,\lambda_B)P(E,\lambda_C)\mathrm{d}E}, \\ \frac{\phi_{ABC}}{\phi_{AC}} = \frac{\int_0^{E_{\max}} S(E)P(E,\lambda_A)P(E,\lambda_B)P(E,\lambda_C)\mathrm{d}E}{\int_0^{E_{\max}} S(E)P(E,\lambda_A)P(E,\lambda_C)\mathrm{d}E}, \end{cases} \tag{2.27}$$

where $P(E,\lambda_i) = 1 - e^{-\frac{EQ(E)}{3\lambda_i}}$ for $i \in \{A,B,C\}$ by (2.26), $S(E)$ is the normalized beta spectrum, λ is the free parameter, E is the energy and $Q(E)$ is the ionizing quenching function.

The left hand side of equation (2.27) is measured in the experiment via the coincidence counting rates since their ratios converges to those of their efficiencies. Now, if the beta spectrum $S(E)$ is known and a realistic value for Birks constant kB is assumed, one may solve for the free parameters λ_i e.g. with a bisection algorithm [Bro07]. Using these numerical values, the efficiency can be calculated via (2.18).

[10] MAC3 = Module d'Acquisition de Coïncidences triples

2.2.2 Cherenkov counting based on the free parameter model

When electrically charged particles travel relatively faster than the speed of light in a transparent medium, so called Cherenkov radiation can be observed. It consists of photons which are emitted by the molecules of the medium when these return to their ground state after having their electron clouds locally distorted by the charged particles. The Cherenkov radiation propagates as a conical wave front in the travel direction of the charged particles. The emitted spectrum is continuous and typically ranges from the visible to the ultraviolet light range [LAn03]. The condition for such radiation to occur can be expressed as

$$\beta := \frac{v_\beta}{c} \geq \frac{1}{n}, \tag{2.28}$$

where v_β is the velocity of the particle in the medium, c the speed of light in vacuum and n is the refractive index i.e. the ratio of the speed of light in vacuum and the phase velocity of light v in the medium ($n = \frac{c}{v}$). In water ($n = \frac{4}{3}$), Cherenkov radiation is generated by beta particles with a kinetic energy greater than 263 keV, which corresponds to a speed of approximately 0.75 c i.e. the speed of light in water. The radiation is emitted as a cone in the medium, where the opening angle 2θ is defined by

$$\cos\theta = \frac{1}{n\beta}. \tag{2.29}$$

The emitted photons can be detected with PMTs for precise activity determinations. Since a scintillation cocktail is not needed, the sample may be measured using a simple aqueous solution which reduces costs and the risk of contamination. While chemical quench is not possible for such methods as the photons do not stem from the fluorescent molecules, there may be color quenching due to the resulting refractive index of the solvent. The counting efficiency can be calculated according to the free parameter model when the light anisotropy is also taken into consideration [Kos14]. One has that the number of Cherenkov photons k that are emitted due to an emitted electron of energy E in an aqueous solution is given by

$$k(E) = \int_0^E \frac{\mathrm{d}k}{\mathrm{d}x} \frac{1}{\rho \left(\frac{\mathrm{d}E}{\mathrm{d}X}\right)} \mathrm{d}E, \tag{2.30}$$

where x is the path length, ρ is the density of the medium and $\left(\frac{\mathrm{d}E}{\mathrm{d}X}\right)$ is the electron stopping power.

If one assumes that the number of photoelectrons created at the photocathode of the PMT follows a Poisson distribution, the counting efficiency can be determined. In the case of two PMTs, one has

$$\epsilon_2 = \int_0^{E_{\max}} S(E) \left(1 - e^{-\frac{qk(E)\alpha}{2}}\right) \left(1 - e^{-\frac{qk(E)(1-\alpha)}{2}}\right) \mathrm{d}E, \tag{2.31}$$

where S is the beta spectrum, q is a free parameter and α is the anisotropy parameter which takes the directional property of the Cherenkov radiation into consideration. The values of the two parameters can be found via relative tracing methods, as described in figure 2.4, using two radionuclide samples with known activities and parameters e.g. ^{32}P and ^{36}Cl.

If three PMTs are used, the efficiency can be determined via the triple and double coincidence ratio method, with the added anisotropy parameter α.

$$\epsilon_{\mathrm{T}} = \int_0^{E_{\max}} S(E) \left(1 - e^{-\frac{qk(E)\alpha_1}{3}}\right) \left(1 - e^{-\frac{qk(E)\alpha_2}{3}}\right) \left(1 - e^{-\frac{qk(E)\alpha_3}{3}}\right) \mathrm{d}E, \tag{2.32}$$

where

$$\alpha_1 = \alpha; \quad \alpha_2 = \frac{1}{2}(3-\alpha)\alpha \quad \text{and} \quad \alpha_3 = 3 - \frac{1}{2}(3-\alpha)\alpha - \alpha \tag{2.33}$$

and

$$\begin{aligned} \epsilon_{\mathrm{D}} = \int_0^{E_{\max}} S(E) \Big[& \left(1 - e^{-\frac{qk(E)\alpha_1}{3}}\right) \left(1 - e^{-\frac{qk(E)\alpha_2}{3}}\right) \\ & + \left(1 - e^{-\frac{qk(E)\alpha_1}{3}}\right) \left(1 - e^{-\frac{qk(E)\alpha_3}{3}}\right) \\ & + \left(1 - e^{-\frac{qk(E)\alpha_2}{3}}\right) \left(1 - e^{-\frac{qk(E)\alpha_3}{3}}\right) \\ & - 2 \left(1 - e^{-\frac{qk(E)\alpha_1}{3}}\right) \left(1 - e^{-\frac{qk(E)\alpha_2}{3}}\right) \left(1 - e^{-\frac{qk(E)\alpha_3}{3}}\right) \Big] \mathrm{d}E. \end{aligned} \tag{2.34}$$

As the number of counted decay grows large, the counting ratios converge to the efficiency ratios i.e.

$$\frac{R_{\mathrm{T}}}{R_{\mathrm{D}}} = \frac{\epsilon_{\mathrm{T}}}{\epsilon_{\mathrm{D}}}$$

and from this relation one can solve for the free parameter q. It holds that the anisotropy can be described using a one parameter empirical formula [Kos14]

$$\alpha(E) = x \left(\frac{3}{4} + \frac{1}{4n\beta}\right), \tag{2.35}$$

where x is determined from measurements.

2.2.3 Classical radionuclidic calorimetry

It is also possible to determine the activity of radionuclides using classical calorimetric methods [Col07] by measuring the thermal power of a sample i.e.

$$P = c \cdot A \cdot \bar{E}, \tag{2.36}$$

where P denotes the measured power, $c \in [0, 1]$ the fraction of the decay energy that is measured by the setup, A the activity of the sample and $\bar{E}$ the average decay energy of the radionuclide sample.

Thus, for a beta emitter the activity of the sample is given by

$$A = \frac{P}{c \cdot \bar{E}(S)}, \quad \text{where} \quad \bar{E}(S) = \int_0^{E_{\max}} E \cdot S(E) \mathrm{d}E \tag{2.37}$$

and S is the normalized beta spectrum (2.19).

An isothermal setup that uses this principle has been employed e.g. at the NIST [Col02, Col07] to standardize among others the beta emitters ^{63}Ni and ^{32}P. The setup is operated at room temperature and features a heat bath which contains approximately 45 l of water which is held at a temperature of $T = 30 \pm 0.001\,^{\circ}\mathrm{C}$. Thermal equilibrium is maintained by employing an internal heater along with circulating approximately $15\,\mathrm{l\,min^{-1}}$ water from a chiller bath $T_{\mathrm{chi}} = 22 \pm 0.01\,^{\circ}\mathrm{C}$ around the jacket of the heat bath. The heat bath contains a reference cell (R) and an active sample cell (S) which are each connected to a Peltier element as depicted in figure 2.6, although any kind of thermometers may be employed in principle.

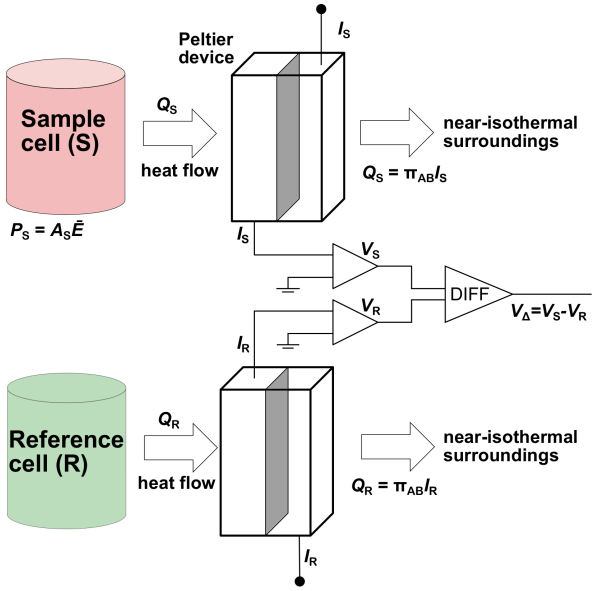

Figure 2.6: Schematic of the classical microcalorimetric setup for activity determination at NIST.

The sample cell is dimensioned to absorb the complete energy of the nuclear decays i.e. to stop every emitted particle. The deposition of energy results in a temperature increase within the corresponding Peltier element which in turn leads to a migration of charge carriers in the device due to the Seebeck effect. While the Peltier element output voltage of the sample cell varies along with the heat bath and the deposited decay energy, the reference Peltier element varies with the heat bath only. The voltage difference $V_\Delta = V_\mathrm{S} - V_\mathrm{R}$ is taken as the measurement quantity and is proportional to the temperature difference i.e. the power generated by the sample decays.

The system is calibrated by employing e.g. a thermoelectric heater within the sample cell with a known power P_C to obtain a calibration curve $V = f(P_C)$ and by inverting this curve one can determine the power in the reference cell from the measured voltage as $P_S = f^{-1}(V_\Delta)$. Typically, f is assumed to be a simple linear function without offset. The sample activities required to perform measurements with the described setup are relatively high. To measure decay powers that exceed $10\,\mu$W one needs approximately 10.9 GBq of ^{3}H and 90.0 MBq of ^{32}P, respectively. The power measurement sensitivity depends on the isothermal quality of the setup and it is estimated that a power accuracy of 0.05% is achievable with the NIST setup. However, to determine the activity one needs the mean decay energy $\bar{E}$ of the radionuclide (2.37) and its uncertainty may very well dominate the error budget e.g. $\bar{E}_{^{55}\mathrm{Fe}} = 5.87 \pm 0.02\,\mathrm{keV}$=5.87 keV±0.34% [Col07]. Again, this calls for adequate radionuclide data with small uncertainties.

2.3 The case for high resolution beta spectrometry

If an activity measurement is carried out with the primary methods described above, one would expect:

- Consistency when comparing the outcomes of the respective methods.
- The result is consistent for each method when varying the counting efficiency within reasonable limits.

In practice, it may happen that these expectations are not realized due to:

i) Inappropriate assumptions in the underlying model e.g. wrong calculation of the ionizing quenching function or the Birks constant.

ii) Systematic errors in the measurement setup e.g. the counters are not operating correctly due to dead-time issues, sample impurities or instabilities.

iii) Using inaccurate nuclear data for the efficiency calculation. In the case of beta emitters this comprises the beta spectrum shape and its maximum energy.

Thus, if the activity is adequately measured using multiple methods and the results are consistent, the beta spectrum shape and maximum energy are validated in this sense. However, if two beta spectra yield different results, at least one of them is incorrect.

In the following, we will show validation results for certain beta spectra using the liquid scintillation counting methods CNET and TDCR, described above. It turns out that beta spectra measured with MMCs reduce the discrepancy between the methods, which thus speaks for the relative accuracy of such beta spectrometers.

2.3.1 The case for using MMCs in beta spectrometry

To date, most beta spectra were measured with semiconductor detectors, scintillation devices or magnetic spectrometers [Beh76, Kos19]. These methods suffer from rather

low energy resolutions compared to what is achievable with LTD[11] calorimeters. More importantly, measuring low-energy beta particles with non-LTDs is difficult due to absorption and attenuation effects within sources and dead layers. Thus, the low-energy region ($\leq 50\,\mathrm{keV}$) of many beta emitters is still unknown and one has relied on semi-empirical extrapolations and theoretical calculations. This combined information of the beta spectrum was thought to be sufficiently accurate until discrepancies arose when equivalent primary activity methods were used to measure beta emitters.

In fact, when the activity of a ^{63}Ni solution was determined with the CNET and TDCR methods using the classical spectrum found in the literature, the results did not agree [Kos15, Kos19]. Furthermore, the CNET result showed a trend when the efficiency parameter was varied. When a more elaborate approach for calculating the allowed beta spectrum of ^{63}Ni, that included the atomic exchange and screening effect, was used [Mou14] and which was experimentally supported by an MMC measurement [Loi14], the results for the activity determination are much more in agreement, as depicted in figures 2.7-2.8 below.

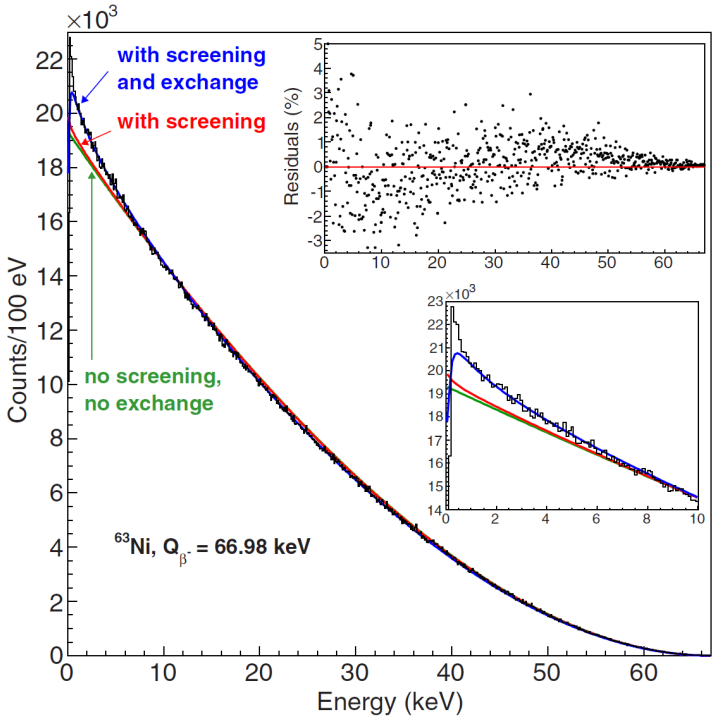

Figure 2.7: Image reproduced from [Mou14]: a ^{63}Ni beta spectrum measured with a 4π MMC setup [Loi14] compared with an analytical calculation **(green)**, a numerical calculation with screening **(red)** and a numerical calculation with screening as well as atomic exchange effect **(blue)**. The data were normalized by integrating over the energy from 500 eV to E_{max}. Standardized residuals between the data and the elaborate numerical calculation as defined in [Mou15] and A.3 **(top inset)** along with a close-up image of the low-energy region **(bottom inset)** are also depicted.

[11]LTD = Low Temperature Detector

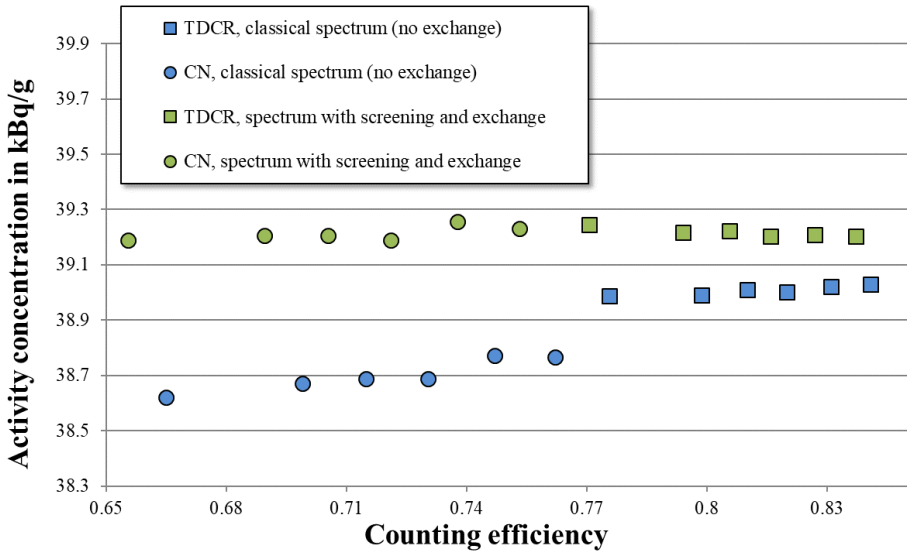

Figure 2.8: Comparison of determining the activity for ^{63}Ni with the liquid scintillation counting methods CNET and TDCR. Calculated beta spectra using the classical vs. the atomic exchange and screening effect were used as inputs for calculating the efficiency. In the latter case the primary counting methods are much more in agreement. Image reproduced from [Kos15].

Similarly, this was the case when the corresponding measurement and a similar analysis was carried out for the beta emitter ^{241}Pu, which has a first-forbidden non-unique beta transition [Loi10, Kos11, Mou14].

The MetroBeta project [Loi18] aimed to improve theoretical computation methods of beta spectra along with modern measurement techniques for silicon detectors, solid scintillator crystals and magnetic spectrometers and MMCs. Central to this dissertation thesis was the optimization of beta spectrometers based on MMCs, in particular for second forbidden non-unique transitions. The reason for this was two-fold: such beta spectra are difficult to calculate and the measurements of the literature do not cover the low-energy part of the spectra.

2.3.2 ^{99}Tc and ^{36}Cl beta spectra in the literature

The ground state of ^{99}Tc decays via pure beta emission (100%, β^-) to ^{99}Ru.

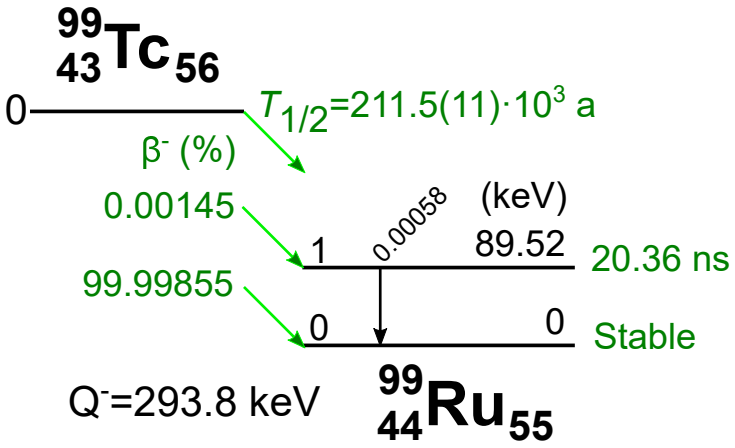

Figure 2.9: Decay scheme of ^{99}Tc [Be11].

Its spectrum has a second forbidden non-unique shape and has been measured several times using various beta spectrometers, see table 2.4. While these setups corresponded to the state-of-the-art when they were applied in the 1950s-70s, the measurements suffer from rather large energy thresholds ($> 50\,\mathrm{keV}$) and limited energy resolutions from a current standpoint as can be seen in table 2.4 and figure 2.10.

Table 2.4: ^{99}Tc measurements in the literature.

Measurement method	**Energy range in keV**	**Shape factor**	$E_{\mathbf{max}}$ **in keV**	**Ref.**
Magnetic spectrometer	> 140	$\sim q^2 + p^2$	290	[Tai51]
Magnetic spectrometer	> 50	$q^2 + (0.5 \pm 0.13) \cdot p^2$	292	[Fel52] [Wu55] [Beh76]
Plastic scintillator	> 50	$q^2 + (0.49 \pm 0.04) \cdot p^2$	294	[Sny66]
4π Si(Li) detector	$55 - 250$	$S(W) = 1 - 3.97 \cdot W + \frac{1.15}{W} + 3.05 \cdot W^2$ or $q^2 + 0.54 \cdot p^2$	293	[Rei74]

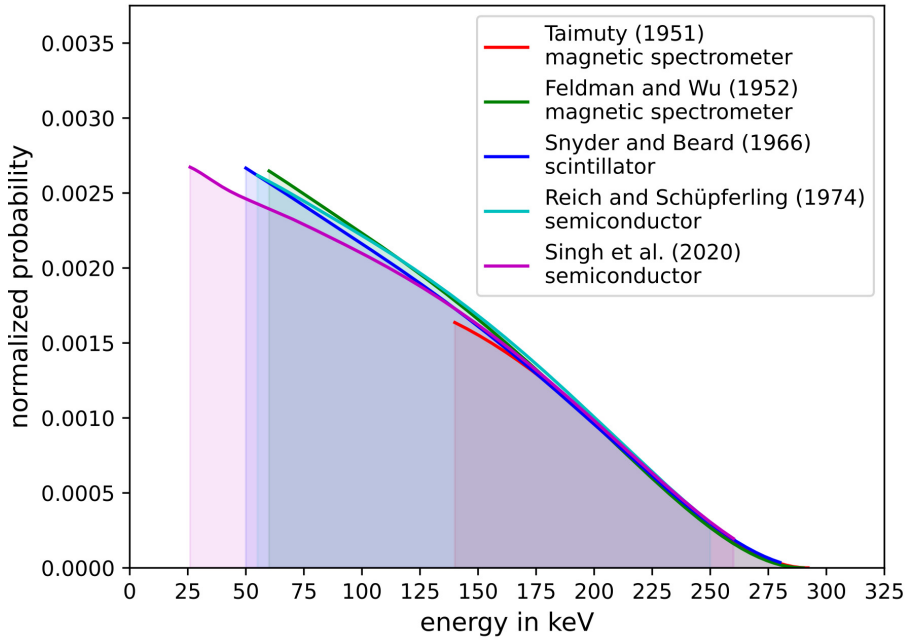

Figure 2.10: ^{99}Tc beta spectra in the literature along with an unpublished spectrum by A. Singh et al. using a setup described in [Sin19, Sin20]. The spectra have been normalized for counts in the energy interval 150-250 keV to allow for a comparison.

The ground state of ^{36}Cl has two decay branches. Firstly, the dominating beta minus branch of second forbidden type with a probability of 98.1(1)% and a maximum energy of 709.53(5) keV (nuclear data from [Be13]). Secondly, the electron-capture branch to the ground state of ^{36}Ar has a probability of approximately 1.9(1)% and there is also a very weak beta plus branch 0.00157(30)%.

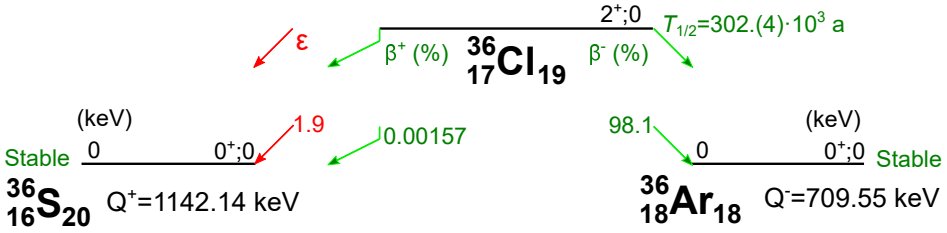

Figure 2.11: Decay scheme of ^{36}Cl [Be13].

The beta spectrum of ^{36}Cl was measured several times in the past, see table 2.5 and figure 2.12. Impressively, the MMC measurement [Rot08] covers almost the entire energy region. Along with the spectrum from [Wil67], it showed the smallest deviation between calculated and experimental efficiencies when a validation was done using the TDCR-Cherenkov method [Kos19].

Table 2.5: ^{36}Cl measurements in the literature.

Measurement method	**Energy range in keV**	**Shape factor**	$\bar{E}$ **in keV**	**Ref.**
Proportional counter	$180 - 680$	q^2	165.0	[Ful51]
Magnetic spectrometer	$105 - 640$	$p^2 + 0.6 \cdot q^2$	301.8	[Fel52] [Wu55]
4π plastic scintillator	$89 - 630$	$p^2 + (0.57 \pm 0.03) \cdot q^2$	303.8	[Joh56]
4π Si(Li) detector	$30 - 680$	$S(W) = 1 - 1.0 \cdot W$ $-\frac{0.24}{W} + 0.42 \cdot W^2$	303.9	[Wil67]
$\sim 4\pi$ Si(Li) detector(s)	$105 - 660$	$1.58 \cdot p^2 + q^2$ $(= p^2 + 0.633 \cdot q^2)$	299.7	[Sas72]
4π Si(Li) detector	$20 - 680$	$S(W) = 1 - 0.981 \cdot W$ $-\frac{0.232}{W} + 0.378 \cdot W^2$	304.9	[Rei74]
Liquid scintillator	$66 - 400$	$S(W) = 1 - 1.167 \cdot W$ $+1.267 \cdot W^2$	305.3	[Gra05]
Metallic magnetic calorimeter	$6 - E_{\max}$	$S(W) = 1 - 1.326 \cdot W$ $+0.6328 \cdot W^2$	309.6	[Rot08] [Kos11]

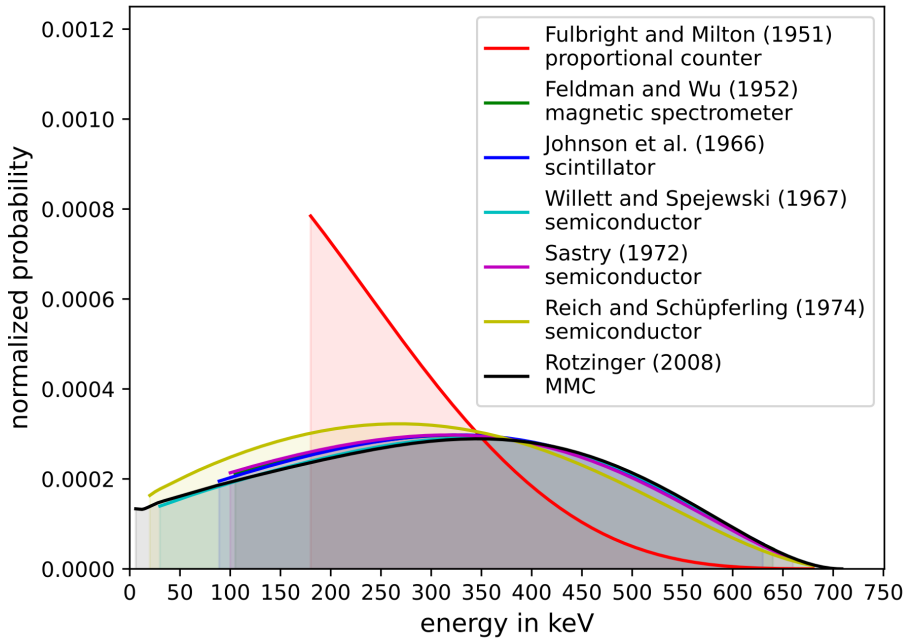

Figure 2.12: ^{36}Cl beta spectra in the literature. In this plot, the spectra are normalized for counts in the energy interval 200-625 keV to allow for a comparison.

3

Metallic Magnetic Calorimeters (MMCs)

Microcalorimeters typically consist of a small absorber that is temperature monitored by a detector. When the energy ΔE is deposited into the absorber, the temperature increase ΔT of such a device is inversely proportional to its heat capacity C:

$$\Delta T = \frac{\Delta E}{C}. \tag{3.1}$$

The idea to detect particles with low-temperature magnetic calorimeters dates back to the mid-1980s [Sei86, Fle05]. In the following years, efforts were focused on utilizing dielectric materials due to their successful application as thermometers. However, the weak coupling of their magnetic moments to phonons at low temperatures leads to rather slow response times which make such detectors less attractive for many applications. Shortly thereafter, it was proposed to use magnetic ions in metallic host materials as a detector material [Ban93].

In a Metallic Magnetic Calorimeter (MMC) [Fle05, Fle09, Kem18] the detector is composed of a metallic paramagnet which is put in a weak magnetic field B and operated at a temperature T, as depicted in figure 3.1. When a particle or radiation deposits the energy ΔE in the absorber, it leads to a temperature increase ΔT. Since the magnetic susceptibility of the paramagnet is strongly temperature dependent, any temperature change will lead to a change in its magnetization M i.e.

$$\Delta M = \frac{\partial M}{\partial T} \cdot \Delta T = \frac{\partial M}{\partial T} \cdot \frac{\Delta E}{C_{\mathrm{tot}}}, \tag{3.2}$$

where C_{tot} denotes the total heat capacity of the absorber and the paramagnet. The corresponding magnetic flux change $\Delta\Phi$ can be measured by means of a Superconducting QUantum Interference Device (SQUID) sensor [Dru07].

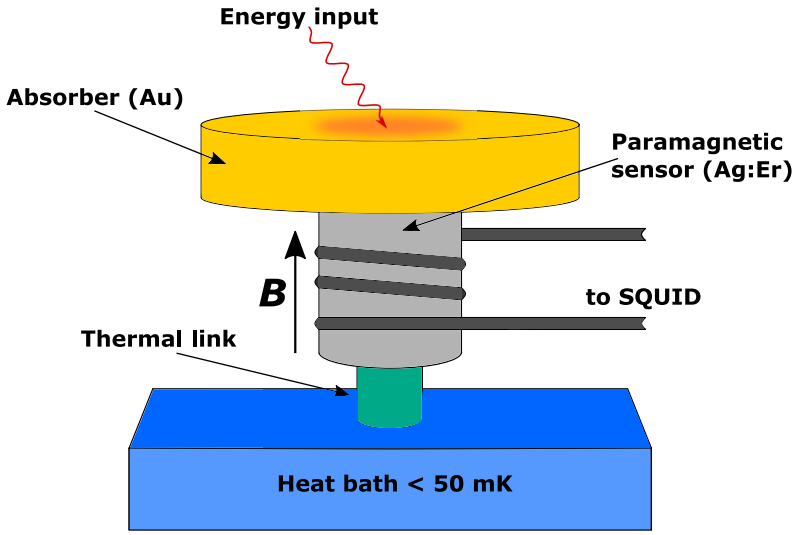

Figure 3.1: Schematic of an MMC.

3.1 Absorber properties

In an MMC detector, the particle deposits its energy within the absorber. Depending on the nature of the particle this can occur via several types of processes [LAn03, Sin20]. When electrically charged particles such as alpha particles, protons or beta particles interact with the absorber material it leads to significant energy loss due to elastic interactions e.g. via scattering by the Coulomb field of the atom or the nucleus. There may also be inelastic interaction such as electron orbital ionization or excitation, which takes place when the coulombic energy transfer is not sufficient to eject an electron from an atom. Bremsstrahlung emission occurs when the charged particle changes its velocity as it interacts with the charges of the atomic nuclei. Electromagnetic radiation i.e. photons deposit their energy via other processes such as the photoelectric effect, Rayleigh or Compton scattering and pair production.

An absorber material needs to have a high stopping power for the particles and radiation it is to detect i.e. a high quantum efficiency. It should also allow for fast and complete thermalization. From a practical standpoint, it is beneficial if the material is available in a highly pure form while being chemically stable. As the absorber preparation process may involve enclosing the sample or integrating it with the detector, it is advantageous if the material is easy to machine and compatible with clean room fabrication processes, respectively.

Determined by the experimental demands, several types of absorber materials can be utilized [Vel20]. Noble metals such as gold (Au, $Z = 79$) or silver (Ag, $Z = 47$) are widely employed as they have free conduction electrons which lead to excellent thermalization. On the other hand, the electrons make a dominant contribution to the heat capacity at low temperatures $C_e \sim T$. Their inert properties and compatibility with fabrication as well as sample preparation make noble metals advantageous for MMC

experiments. Notably, due to their rather high atomic numbers noble metal materials may generate bremsstrahlung when charged particles of relatively high kinetic energy ($\geq 300\,\mathrm{keV}$) interact. It holds that the probability of bremsstrahlung $\left(\frac{\mathrm{d}E}{\mathrm{d}x}\right)_r \sim Z^2$. This along with other energetic losses e.g. as a result of absorber geometry that is less than the full solid angle of 4π may lead to a reduced quantum efficiency and is critical in certain applications. It is in particular relevant for beta spectrometry. In order to measure the true spectrum of the beta transition, the entire energy of each emitted beta particle needs to be measured by the detector. A necessary condition for this to be possible is that the energy is completely deposited within the absorber [Pau20], see section 5.2.2. This means that the absorber quantum efficiency

$$QE_{\mathrm{abs}} := \frac{\text{kinetic energy of emitted particles}}{\text{energy deposition of emitted particles into the absorber}} \tag{3.3}$$

is very close to 100%. When QE_{abs} is significantly less than that, due to primary (i.e. emitted electrons leaving the absorber) and secondary (particles generated by the emitted electron leaving the absorber) energy escape, the beta spectrum will typically be distorted. Even if a high initial energy beta electron itself is stopped within a given absorber, bremsstrahlung photons may escape. This effect may cause decay events with high energies to be detected as lower energy decays, see section 5.2 for a quantitative discussion.

The probability of bremsstrahlung production increases with the electron energy and the atomic number of the material in which the electron decelerates. Hence, a low atomic mass absorber material can reduce the number of generated bremsstrahlung photons. On the other hand, this has two disadvantages: i) a larger absorber with higher heat capacity is then required to stop the electrons, degrading the energy resolution and heightening the energy threshold of the detector, ii) the photon absorption probability of a low atomic mass absorber material is lower, partially counteracting the advantage of the reduced bremsstrahlung production.

A better choice for such an experiment may be to use a bilayer absorber, [Loi18, Boc19]: an inner low atomic mass layer reduces bremsstrahlung production where the electrons still have high energy and a high atomic mass outer layer reduces the total absorber thickness required for stopping the electrons while enhancing the photon absorption probability. In figure 3.2, a qualitative comparison between a gold absorber and a Au-Cu bilayer is provided.

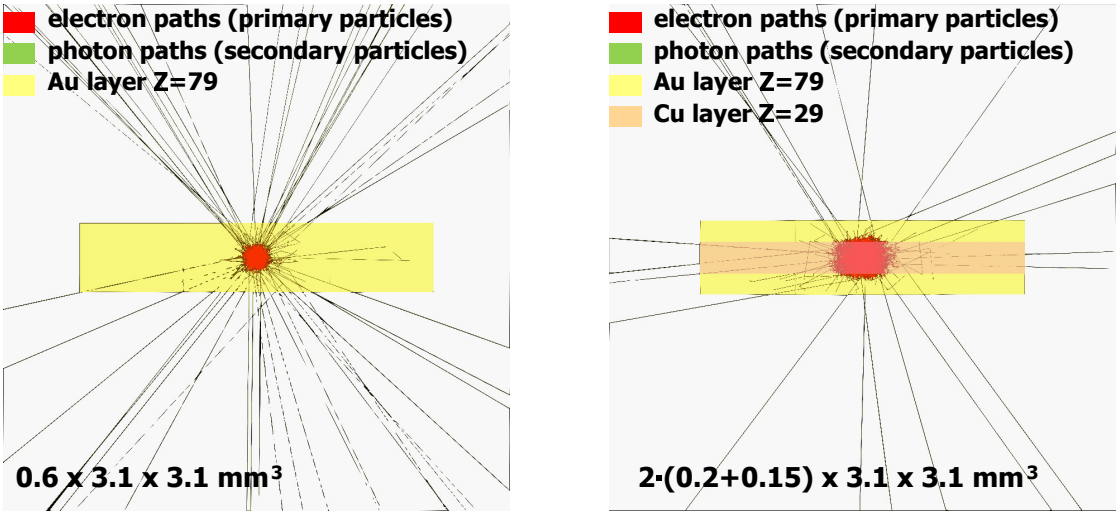

Figure 3.2: Monte Carlo simulations for 1000 tracks of a 750 keV monoenergetic electron source embedded in two different 4π absorbers. The pure Au absorber **(left)** has a greater stopping power for the emitted electrons but plenty of bremsstrahlung photons are generated. The Cu core of the bilayer absorber **(right)** has a weaker stopping power but less energy is lost via bremsstrahlung photons.

Dielectric materials e.g. the semiconductors silicon (Si, $Z = 14$) and germanium (Ge, $Z = 32$) have much lower heat capacity as they do not have free conduction electrons at low temperatures and only the photons contribute to the heat capacity $C_{\mathrm{ph}} \sim T^3$ according to the Debye model. When particles, in particular photons, interact with the material electron-hole pairs can be created which may be trapped within lattice defects and the resulting recombination times can be very long. Furthermore, the number of created electron-hole pairs can vary for each interaction even for photons having the same energy. Thus, employing such materials typically reduces the energetic resolving power.

Alternatively, superconductors such as lead (Pb, $Z = 82$, $T_{\mathrm{c}} = 7.2\,\mathrm{K}$) and tin (Sn, $Z = 50$, $T_{\mathrm{c}} = 3.7\,\mathrm{K}$) have been used as absorber materials [Hoo06, Kra13]. Below their critical temperature T_{c} such absorbers benefit from the fact that their conduction electrons do not contribute to the heat capacity as these are bound as bosonic Cooper pairs. This property makes them interesting for experiments as one could fabricate rather large absorbers with a large quantum efficiency and a low heat capacity. Still, the thermalization of such absorbers can be on the order of hundreds of milliseconds [Cos93, Hen12] which may be due to relatively long life times of broken Cooper pairs that are created when energy is deposited into the absorber.

3.2 Temperature detector

In MMCs, the temperature detector is typically realized using an alloy of gold or silver that is doped with $\sim 300\,\mathrm{ppm}$ of erbium (Er). At such concentrations, the erbium forms solid solutions with Au and Ag while the Er^{3+} ions substitute the host material

ions at the regular lattice sites while donating electrons to the conduction band, see figure 3.3.

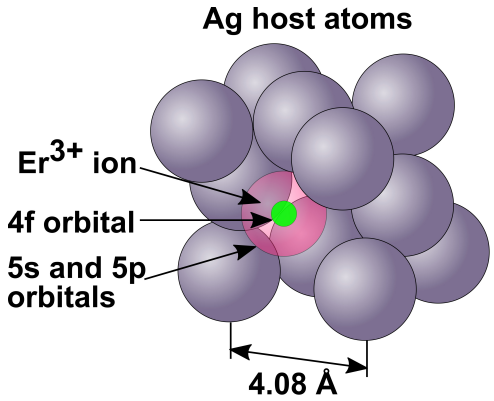

Figure 3.3: Erbium ion in silver lattice.

The electron configuration of Er^{3+} is given by $[Kr]4d^{10}4f^{11}5s^25p^6$ and it is the partially filled 4f shell, located relatively deep within the ion, that causes the paramagnetic properties of the material. Due to its deep location, crystal field effects are negligible at temperatures above 100 K and the magnetic moments can be calculated from the orbital angular momentum **L**, the spin angular momentum **S** and the total angular momentum **J** using Hund's rules as [Kem18]

$$\mu = g_J \mu_B \mathbf{J}, \tag{3.4}$$

where

$$g_J = 1 + \frac{J(J+1) + S(S+1) - L(L+1)}{2J(J+1)} \tag{3.5}$$

is the Landé factor and μ_B is the Bohr magneton. In the case of Er^{3+}, one has $g_J = 6/5$ with $L = 6$, $S = 3/2$ and $J = 15/2$.

At temperatures below 100 K, the crystal field effect needs to be considered and its fcc symmetry induces a splitting of the 16-fold degeneracy of the Er^{3+} into three Γ_8 quartets along with a Γ_6 and a Γ_7 doublet, respectively. The energy of the Γ_7 doublet is the lowest and separated from the higher multiplets with an energy gap of $\Delta E_{Au:Er}/k_B = 17\,K$ and $\Delta E_{Ag:Er}/k_B = 25\,K$. Thus, at typical MMC operating temperatures of around 100 mK the paramagnetic sensor can be modeled as a two-level system with an effective spin $\tilde{S} = 1/2$ and an isotropic g-factor of $g = 6.8$.

3.3 Signal characteristics

The thermodynamic properties of a Au:Er paramagnet, i.e. the temperature dependence of the magnetization and the specific heat, can be reliably calculated using mean-field or Monte-Carlo methods [Fle05]. Both approaches model the magnetic

dipole-dipole interaction and the RKKY[1] interaction.

The change in magnetization of an MMC, as given by (3.2), is inversely proportional to the heat capacity C_{sens} and proportional to $\partial M/\partial T$ i.e. the slope of the sensor material magnetization as a function of the temperature. It was shown in [Fle03] that these two quantities can be qualitatively well-understood using statistical arguments, where thermodynamical properties of the small Er concentrations are modeled by an internally non-interacting ensemble of magnetic moments.

When the Er^{3+} ions with spin $\tilde{S}$ are placed in a magnetic field[2] B their ground states split up due to the Zeeman effect into $2\tilde{S}+1=2$ energy levels which distribute according to Boltzmann factors. The heat capacity of such a Zeeman ensemble can be described by

$$C_{\text{z}}(T) = Nk_{\text{B}}\left(\frac{\delta E}{k_{\text{B}}T}\right)^2 \frac{e^{\delta E/k_{\text{B}}T}}{\left(e^{\delta E/k_{\text{B}}T}+1\right)^2}, \tag{3.6}$$

where N denotes the number of independent magnetic moments and $\delta E = \tilde{g}\mu_{\text{B}}B$ is the energy splitting with the Landé factor $\tilde{g}=6.8$. At lower temperatures the heat capacity rises until it reaches a local maximum at $T \approx 0.42\,\delta E/k_{\text{B}}$, which is known as the Schottky anomaly, whereafter it decays $\sim B^2/T^2$ as depicted in figure 3.4.

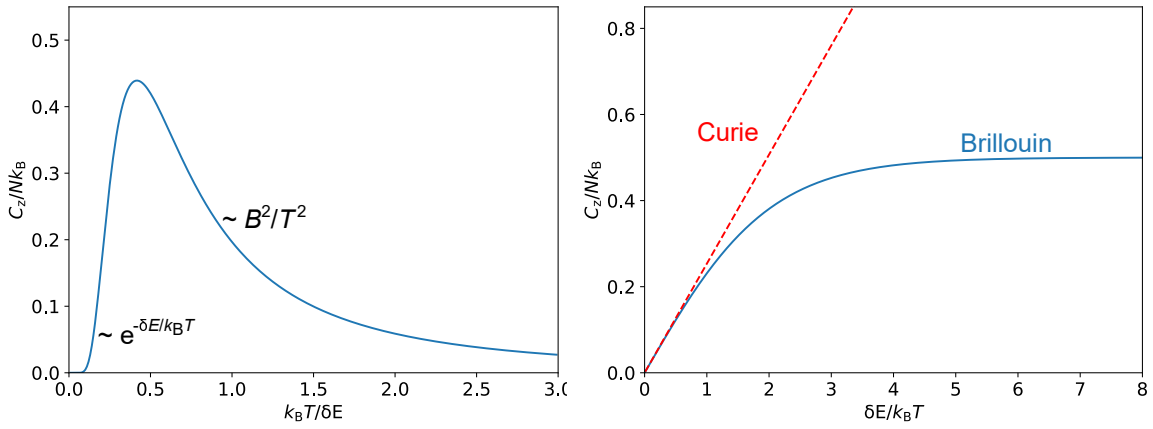

Figure 3.4: Qualitative functions of the specific heat **(left)** and magnetization **(right)** as a function of the temperature and inverse temperature, respectively.

Analogously, one may derive the magnetization M of a sensor with volume V, from the change of the free energy with the external magnetic field B:

$$M(T) = \frac{N}{V}\tilde{g}\mu_{\text{B}}\tanh\left(\frac{\delta E}{2k_{\text{B}}T}\right). \tag{3.7}$$

[1] RKKY = Ruderman-Kittel-Kasuya-Yoshida

[2] In the qualitative discussion, the magnetic flux density B and the proportional magnetic field strength H are used interchangeably.

At higher temperatures it follows a Curie law $\sim 1/T$ and as lower temperatures are approached ($k_\mathrm{B}T \ll \delta E$), the spins align in parallel with the external magnetic field such that the magnetization saturates at a value $M = \frac{N}{V}\tilde{g}\mu_\mathrm{B}$, see figure 3.4.

For quantitative studies, however, it is useful to take the interaction between the magnetic moments of the ensemble into consideration. The main contribution comes from the RKKY-interaction, which occurs when conduction electrons of the Au or Ag host material in the vicinity of an Er^{3+} become polarized due to its spin angular momentum and mediate the interaction to the next spin. In figure 3.5 simulations [Fle03] based on the exact diagonalization of the interaction Hamiltonian are plotted as lines. These agree very well with the measurement data of a Au:$Er_{300\,\mathrm{ppm}}$ paramagnet which are plotted as symbols for different magnetizations and variable temperature.

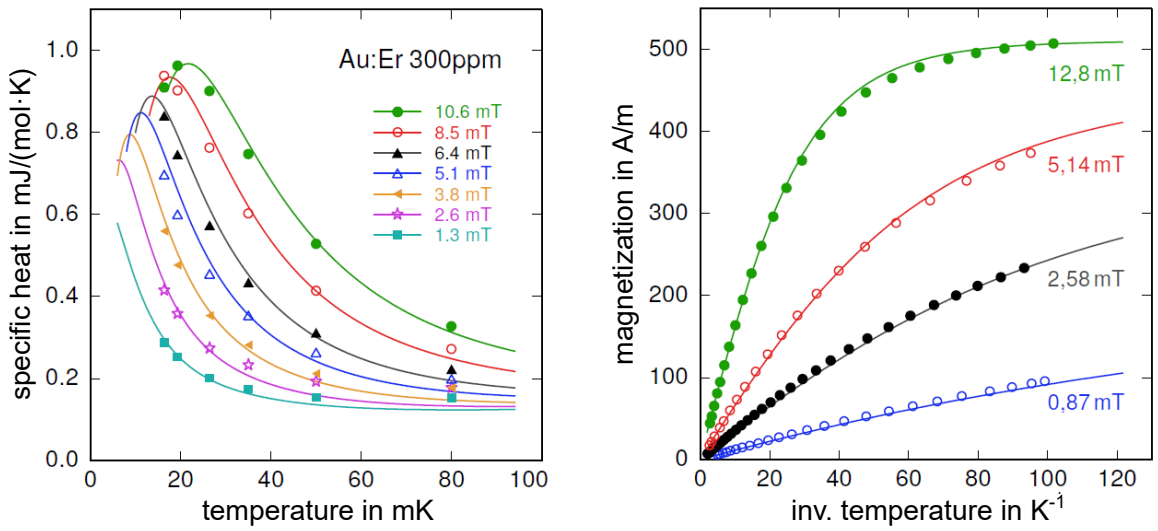

Figure 3.5: Quantitative simulation curves based on the exact diagonalization of the interaction Hamiltonian **(lines)** and measurement data of a Au:$Er_{300\,\mathrm{ppm}}$ paramagnet **(symbols)** for the specific heat **(left)** and magnetization **(right)** as a function of the temperature and inverse temperature, respectively. Image adapted from [Fle03, Gei20].

A useful parameter for quantifying the relative strength of the interactions is described by the parameter $\alpha := \Gamma_\mathrm{RKKY}/\Gamma_\mathrm{dd}$, where one has $\Gamma_\mathrm{RKKY}, \Gamma_\mathrm{dd} \sim T^{-3}$. The dipole-dipole interaction is approximately the same for silver and gold host materials but the RKKY-interaction is several times stronger in Ag:Er ($\alpha_\mathrm{Ag} = 12.5$, [Hen17]) than in Au:Er ($\alpha_\mathrm{Au} \approx 5$, [Fle03]). Based on the properties of Au:Er, empirical scaling laws have been found for the specific heat capacity of the erbium ions in silver [Hen17]:

$$c_\mathrm{Er}\left(B, T, x, \alpha_\mathrm{Ag}\right) = \frac{\alpha_\mathrm{Au}}{\alpha_\mathrm{Ag}} \cdot c_\mathrm{Er}\left(B, T, \frac{\alpha_\mathrm{Ag}}{\alpha_\mathrm{Au}} x, \alpha_\mathrm{Au}\right) \tag{3.8}$$

and for the magnetization one has

$$M\left(B,T,x,\alpha_{\mathrm{Ag}}\right)=\frac{\alpha_{\mathrm{Au}}}{\alpha_{\mathrm{Ag}}}\cdot M\left(B,T,\frac{\alpha_{\mathrm{Ag}}}{\alpha_{\mathrm{Au}}}x,\alpha_{\mathrm{Au}}\right). \tag{3.9}$$

The formulas (3.8)-(3.9) are useful for predicting the thermodynamic properties of MMCs with high accuracy. While the magnetic dipole-dipole interaction is equal, regardless if Au or Ag is used, the difference of exchange energy leads to a three times larger RKKY interaction in the latter case. As a result, the signal strength when using an Ag:Er paramagnet will be slightly less. On the other hand, an Au:Er paramagnet will have an additional heat capacity. This is caused by the non-zero nuclear quadrupole moment of Au. The lattice symmetry distortion of the Er ions induce strong electric fields gradients along lattice sites where there are Au nuclei and the Au:Er energy eigenstates become non-degenerate which leads to nuclear quadrupole splitting. As a result, there is an initial fast signal decay but in the case of Ag:Er the signal shape is simpler and the energy resolution is better due to the slower signal decay time τ_{decay}.

3.4 Detector geometry and signal shape

While the cylindrical design shown in the schematic picture of figure 3.1 was realized for early MMC prototypes [Buh88, Ban93], it is difficult to realize in dimensions that are needed for many microcalorimetric particle detection applications.

In contrast, planar geometries, as depicted in figure 3.6, allow for very accurate and reproducible microfabrication [Fle05] via photolithography. The superconducting detection coil is realized as a structure consisting of two meanders. By injecting a persistent current into the structure, a static magnetic field is generated which magnetizes the paramagnetic sensor according to its susceptibility. The single meanders have reverse polarity and sense the temperature dependent magnetization change of its paramagnetic sensor pixel, which causes a magnetic flux change that leads to a current shift $\pm\delta I$ in the circuit, respectively. The current shift is measured by the SQUID via its input coil and can be read out as a time-dependent voltage signal, where the polarity indicates which pixel was hit by a particle.

The flux change $\Delta\Phi_{\mathrm{S}}$ in the SQUID is given by

$$\Delta\Phi_{\mathrm{S}}=\frac{M_{\mathrm{IN,S}}}{L_{\mathrm{M}}+2\left(L_{\mathrm{IN}}+L_{\mathrm{P}}\right)}\left(\Delta\Phi_1-\Delta\Phi_2\right), \tag{3.10}$$

where $M_{\mathrm{IN,S}}=k\sqrt{L_{\mathrm{IN}}L_{\mathrm{S}}}$ is the mutual inductance of the input coil for a coupling factor k. L_{IN}, L_{S} and L_{M} denote the inductances of the input coil, SQUID loop and meander structure, respectively. The parasitic inductance L_{P} mainly consists of the inductance from the Al bonds which are often used to connect the realized MMC and SQUID chips, see section 4.3. $\Delta\Phi_1$ and $\Delta\Phi_2$ are the magnetic flux change of pixel 1 and 2, respectively. Thus, uniform temperature changes within the substrate are canceled,

provided the pixels are symmetric.

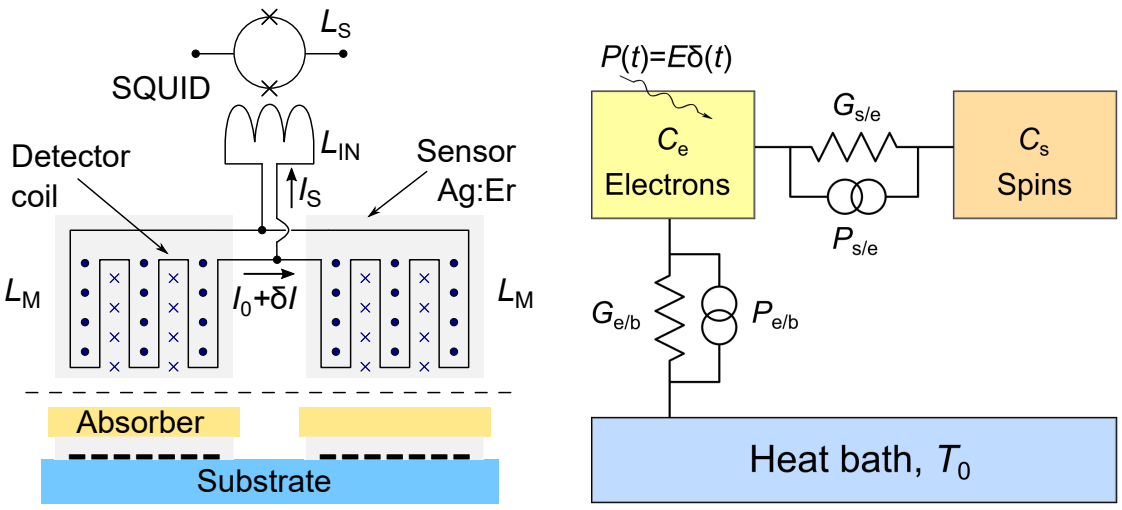

Figure 3.6: Detector geometry **(left)** and canonical subsystems **(right)**, where C, G and P denote the heat capacity, thermal conductivity and noise power. The indices b, e and s refer to the heat bath, conduction electrons and spins, respectively.

The signal shape of the detector as a function of time can be derived by modeling its detector components as a thermodynamical system that consists of two subsystems [Fle05], as schematically depicted in figure 3.6. It is assumed that the absorber and the paramagnetic sensor are in good thermal contact such that phonons and electrons are in thermal equilibrium within the detector. At millikelvin temperatures the heat capacity of the electrons C_e dominate and that of the phonons is regarded as negligible. The magnetic coupling of the electrons to the spins, which was described in section 3.2 above, is given by the thermal conductivity $G_\mathrm{s/e}$ while $P_\mathrm{s/e}$ denotes the corresponding noise power. The paramagnetic sensor is weakly linked to the heat bath, which is analogously described by the thermal conductivity $G_\mathrm{e/b}$ and noise power $P_\mathrm{e/b}$, respectively.

Now, one considers an instantaneous thermal power input into the electronic subsystem as $P(t) = E\delta(t)$, where E is the energy deposit and $\delta(t)$ is the delta distribution function. The resulting system of differential equations for the electron [spin] energy E_e and temperature T_e [E_s and T_s] is given by

$$\begin{cases} \dot{E}_\mathrm{e} = C_\mathrm{e}\dot{T}_\mathrm{e} = G_\mathrm{s/e}\,(T_\mathrm{s} - T_\mathrm{e}) + G_\mathrm{e/b}\,(T_0 - T_\mathrm{e}) + E\delta(t) \\ \\ \dot{E}_\mathrm{s} = C_\mathrm{s}\dot{T}_\mathrm{s} = G_\mathrm{s/e}\,(T_\mathrm{e} - T_\mathrm{s})\,, \end{cases} \tag{3.11}$$

where T_0 is the heat bath temperature.

Since the magnetic signal is dominated by the spin response, the quantity of inter-

est is $\dot{T}_\mathrm{s}$. A solution to (3.11) is given by

$$\Delta T_\mathrm{s} = T_\mathrm{s} - T_0 \tag{3.12}$$

$$= \frac{E}{C_\mathrm{tot}} \left(-e^{-t/\tau_\mathrm{rise}} + -e^{-t/\tau_\mathrm{decay}}\right) =: \frac{E}{C_\mathrm{s}} p(t), \quad \text{for } t \geq 0, \tag{3.13}$$

where $C_\mathrm{tot} = C_\mathrm{e} + C_\mathrm{s}$. The function $p(t) = \beta \left(-e^{-t/\tau_\mathrm{rise}} + -e^{-t/\tau_\mathrm{decay}}\right)$ describes the temporal dynamics of the signal, where $\beta = C_\mathrm{s}/C_\mathrm{tot}$ is the spin proportion of the total heat capacity.

This means that when the energy is deposited into the detector, the temperature rises exponentially to a local maximum value with constant τ_rise and then decays exponentially with constant τ_decay as it thermalizes with the heat bath. The constants depend on the heat capacities and thermal conductivities, see [Fle05] for a general discussion. The dependencies simplify if one assumes approximately equal heat capacities of the paramagnetic sensor and the absorber $C_\mathrm{e} \approx C_\mathrm{s}$ and a weak thermal coupling to the heat bath $G_\mathrm{e/b} \ll G_\mathrm{s/e}$. The rise constant is fundamentally limited by the interaction between the spins and the electrons. Using the Korringa relation $\kappa = \tau_\mathrm{K} \cdot T_\mathrm{e}$ [Ban93, Fle03], it holds that the limit is given by $\tau_\mathrm{0,K} = (1 - C_\mathrm{s}/C_\mathrm{tot})\tau_\mathrm{K}$. In some applications, that involve larger absorbers such as the present work, it is purposeful to avoid this limit i.e. to increase the rise time by introducing a thermal bottle neck $G_\mathrm{a/s}$ as described in [Kem18] and chapter 4. Ideally, the thermal bottleneck ensures complete thermalization of the absorber itself before the heat is transported to the sensor. As a consequence, the rise time constant is not dependent on the position where energy was deposited into the absorber.

From the above it follows that the rise and decay times can be tuned by varying the design parameters of the MMC via its time constants

$$\tau_\mathrm{rise} = \frac{C_\mathrm{a}}{2G_\mathrm{a/s}} \tag{3.14}$$

and

$$\tau_\mathrm{decay} = \frac{C_\mathrm{tot}}{2G_\mathrm{e/b}}, \tag{3.15}$$

respectively, where C_a denotes the heat capacity of the absorber.

3.5 Energy resolution

To specify the energy resolution, one needs to consider the signal as described above along with the various noise components of the system. Using methods from optimal

filtering theory, the FWHM[3] energy resolution of an MMC is given by [Fle05]:

$$\Delta E_{\mathrm{FWHM}} = 2\sqrt{2\ln 2}\left(\int_0^\infty \frac{|\widetilde{p}(f)|^2}{S_{E_{z,\mathrm{tot}}}}\mathrm{d}f\right)^{-1/2}, \tag{3.16}$$

where

$$\widetilde{p}(f) \simeq \frac{\tau_{\mathrm{decay}}}{\sqrt{1+2\pi f\tau_{\mathrm{rise}}}\sqrt{1+2\pi f\tau_{\mathrm{decay}}}}, \tag{3.17}$$

is a normalized detector responsivity rate and $\sqrt{S_{E_{z,\mathrm{tot}}}}$ is the total noise of the detector. The noise budget consists of the following parts.

Thermodynamic energy fluctuations

The subsystems described in 3.6 are thermally linked and heat may fluctuate between them in thermal equilibrium. This can be modeled using the spectral power density $S_{\mathrm{p}} = 4k_{\mathrm{B}}T^2G$. When the noise powers $P_{\mathrm{s/e}}$ and $P_{\mathrm{s/e}}$ are considered in (3.11) and one assumes $C_{\mathrm{e}} \approx C_{\mathrm{s}}$ and $\tau_{\mathrm{rise}} \ll \tau_{\mathrm{decay}}$ the power spectral density is given by [Kem18]

$$S_{E_{z,\mathrm{TEF}}}(f) = 4k_B C_{\mathrm{sens}}T^2\left[(1-\beta)\frac{\tau_{\mathrm{rise}}}{1+(2\pi f\tau_{\mathrm{rise}})^2} + \beta\frac{\tau_{\mathrm{decay}}}{1+(2\pi f\tau_{\mathrm{decay}})^2}\right], \tag{3.18}$$

where k_{B} and T denote Boltzmann's constant and the operating temperature, respectively.

Paramagnetic sensor Er intrinsic $1/f$ noise

The cause of the $1/f$-type noise is not fully understood. It has been found to be independent of temperature between 20 mK and 4.2 K while being proportional to the number of Er ions within the paramagnetic sensor material. One may model it by considering a fluctuating magnetic moment with a noise density of

$$S_{\mathrm{m}} \simeq 0.1\frac{\mu_{\mathrm{B}}}{f^x}, \qquad x \in [0.8, 1] \tag{3.19}$$

to every ion, where the noise exponent x appears to depend on the geometry of the detector [Fle09].

Magnetic Johnson noise

When charge carriers move due to thermal fluctuations it causes magnetic noise. The electrons in the metallic absorber, paramagnet and other support structures in an MMC experiment may thus contribute to the noise budget if they are close enough to the detection coil or the SQUID. For the magnetic Johnson noise it holds that

$$\sqrt{S_{\Phi,\mathrm{J}}} = \mathscr{C}\sqrt{\sigma k_{\mathrm{B}}T}, \tag{3.20}$$

[3] FWHM = Full Width at Half Maximum

where $\mathscr{C}$ is a geometry dependent factor that quantifies the coupling to the detection coil, which may be calculated using finite element methods and σ denotes the electrical conductivity of the metallic component within the detector [Kem18].

Electronic readout noise

The SQUID contributes dominantly to the noise budget and the readout noise can be quantified as the coupled energy resolution

$$\epsilon_{\mathrm{c}} = \frac{S_{\Phi,\mathrm{SQ}}}{2k_{\mathrm{in}}^2 L_{\mathrm{s}}}, \tag{3.21}$$

where $\sqrt{S_{\Phi,\mathrm{SQ}}}$ is the magnetic flux noise of the SQUID, k_{in} the magnetic coupling factor between the SQUID and its input coil and L_{s} is the inductivity of the SQUID.

Under idealized detector conditions, the thermal contributions limit the noise of an MMC from below. The expression in (3.18) corresponds to the intrinsic noise contribution of the detector. If the heat capacities of the absorber and the paramagnetic sensor are equal, it limits the energy resolution to

$$\Delta E_{\mathrm{FWHM}} = 2.35\sqrt{4k_{\mathrm{B}}T^2 C_{\mathrm{sens}}}\left(4\frac{\tau_{\mathrm{rise}}}{\tau_{\mathrm{decay}}}\right)^{1/4}. \tag{3.22}$$

4

Experimental setup

The MMC based beta spectrometer [Pau19] presented in this chapter was developed within the projects MetroBeta [Loi18] and MetroMMC [Ran20]. The thermal sensor consists of a Ag:$Er_{310\,ppm}$ paramagnet, that is put in a weak magnetic field $B \sim 1\,mT$. The field is produced by two superconducting Nb meandering pickup coils holding a persistent current I, as depicted in figure 4.1. A persistent field current $\sim 50\,mA$ is injected to produce the bias magnetic field B. An electric resistance heater is used to realize a current switch [Rot08] between the two superconducting meandering pickup coils. These are connected to each other with an electrical bypass line. When the heater is activated, by applying $\sim 3\,mA$ to it, the bypass line becomes normal conducting while the meandering pickup coil remains superconducting.

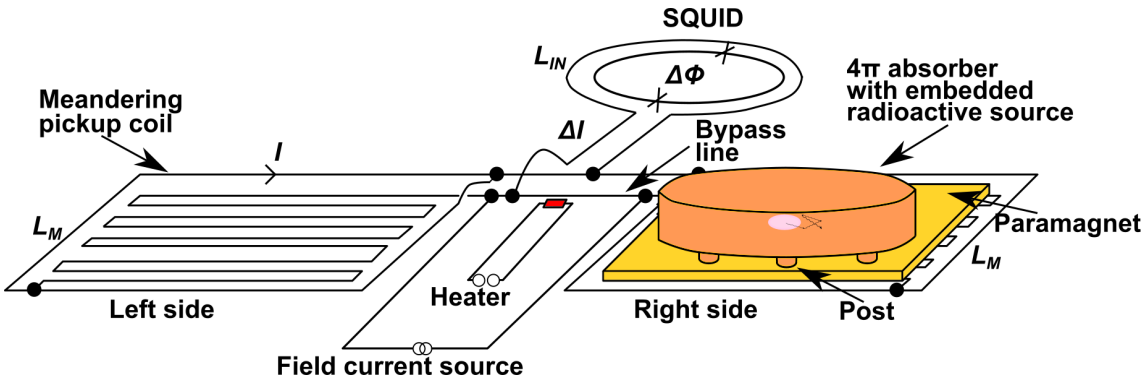

Figure 4.1: Schematic view of the MMC detector: to show the underlying meandering pickup coil structure, the paramagnet on the left side is not included in the picture. The meanders have reverse polarity which results in either a positive or a negative voltage signal in the SQUID.

A 4π gold absorber is thermally linked to the MMC detector via several gold posts

[Kem18] which work as intentional thermal bottlenecks. When a decay occurs in the radionuclide source, the kinetic energy of the emitted beta particle is absorbed completely, causing a small temperature increase in the absorber. The heat is transported via the posts to the paramagnet, which due to the temperature dependence of its magnetic susceptibility, changes its magnetization. The corresponding magnetic flux change of the paramagnet is detected by the superconducting meandering pickup coil, which generates the compensating current ΔI and is coupled to the input coil of the SQUID sensor. Thus, the energy of the radioactive decay in the absorber is proportional to the compensating current. The rise and decay times of the signal pulses depend on the thermal couplings: absorber↔MMC sensor and MMC sensor↔thermal bath, respectively, see (3.14) and (3.15). As there are two sensors with reverse polarity on the MMC chip, it is possible to operate it with two absorbers (either giving rise to positive or negative signal pulses, respectively). The design was made in such a way that the left and right sensors are slightly imbalanced. Hence, the net magnetization due to thermal variations can be measured e.g. during a diagnostic test of the detector characteristics.

4.1 Beta spectrometry using MMCs

To measure high quality beta spectra, one needs to ideally measure every decay of the source in a considered time frame with a high energy resolution over the entire energy range $[0, E_{\max}]$. Hence, the absorber needs to be large enough to completely stop the beta particles of the radioactive decay. When gold absorbers are used, the following thicknesses can be calculated [Loi18]: 260 µm (^{36}Cl, $E_{\max} = 709.5\,\mathrm{keV}$), 60 µm (^{99}Tc, $E_{\max} = 293.8\,\mathrm{keV}$) and 21 µm (^{14}C, $E_{\max} = 156.5\,\mathrm{keV}$).

At the same time, the absorbers need to have small dimensions (0.25-9 mm^2) to ensure a low heat capacity so that a high energy resolution may be realized (3.22) while also being manageable for source embedding. Thus, microfabricated MMC detectors designed for corresponding absorber heat capacities to measure beta spectra with endpoint energies $E_{\max}$ ranging from a few tens of keV up to $\sim 1\,\mathrm{MeV}$ were realized in the MetroBeta project [Loi18], see table 4.1. The constraints of the design optimization were:

1) the heat capacity of the MMC sensor should be matched to that of the absorber,

2) the inductance of the meandering pickup coil should be twice as large as the inductance of the designated SQUID input coil (i.e. $L_{\mathrm{M}} = 2 \cdot L_{\mathrm{IN}}$) and

3) the thermal link between the MMC detector and the on chip heat bath pad should allow a signal decay time of $\sim 1\,\mathrm{ms}$ at the desired operating temperature.

Optimal design parameters concerning the linewidth/pitch of the pickup coil and the meander area/inductance could thus be determined. All five MMC sizes were fabricated at the KIP institute in Heidelberg on a common silicon wafer, which puts an additional constraint on the optimization and fabrication.

In order to calculate the corresponding energy resolution of each design combination, the following fabrication and setup relevant values were used: an Er concentration in Ag of 310 ppm, a sensor thickness of 3 µm, an operating base temperature of 20 mK, with an assumed SQUID white noise level of 0.35 $\mu\Phi_0/\mathrm{Hz}^{1/2}$ and a SQUID $1/f$ noise level at 1 Hz of 2.6 $\mu\Phi_0/\mathrm{Hz}^{1/2}$.

absorber type	XS	S	M	L	XL
material	Au	Au	Au	Au	Au-Cu bilayer
surface shape	circle	circle	octagon	octagon	octagon
diameter	480 µm	600 µm	725 µm	1655 µm	3065 µm
thickness of single foil	15 µm	40 µm	100 µm	300 µm	200 µm: 150 µm (Au:Cu)
absorber heat capacity	8 pJ/K	28 pJ/K	110 pJ/K	400 pJ/K	1.70 nJ/K
designated SQUID type	X1	X1	X1	XS	S
input inductance	2 nH	2 nH	2 nH	27 nH	65 nH
MMC detector type	XS	S	M	L	XL
MMC sensor heat capacity	7.57 pJ/K	17.9 pJ/K	50.6 pJ/K	308 pJ/K	1.17 nJ/K
single meander inductance	3.4 nH	3.1 nH	8.0 nH	56 nH	196 nH
linewidth of pickup coil	2.5 µm	5 µm	5 µm	5 µm	5 µm
pitch of pickup coil	5 µm	10 µm	10 µm	10 µm	10 µm
meander/sensor area (square shape)	$(249\ \mu\mathrm{m})^2$	$(335\ \mu\mathrm{m})^2$	$(538\ \mu\mathrm{m})^2$	$(1427\ \mu\mathrm{m})^2$	$(2663\ \mu\mathrm{m})^2$
expected flux coupling	3.8%	4.0%	2.6%	0.8%	0.5%
optimum field current	38.2 mA	67.8 mA	75.7 mA	63.3 mA	67.1 mA
expected signal size	23.2 $\mathrm{m}\Phi_0$/keV	12.9 $\mathrm{m}\Phi_0$/keV	6.41 $\mathrm{m}\Phi_0$/keV	2.97 $\mathrm{m}\Phi_0$/keV	1.61 $\mathrm{m}\Phi_0$/keV
expected energy resolution	5.17 eV	9.46 eV	19.1 eV	37.5 eV	74.4 eV

Table 4.1: Overview of absorbers, SQUID types and MMC detector parameter values per design in the MetroBeta project [Loi18, Pau19].

4.2 The MetroBeta detector

Embedding the radionuclide of interest within the absorber involves several steps including the use of diffusion welding to seal the Au absorber. To achieve this, temperatures of up to ~ 600 K are applied. Such temperatures are well-known to cause diffusion and subsequent oxidation of the Er ions within the paramagnetic sensor material of the MMC which degrades the measurement performance [Kir10].

Thus, the absorber is prepared separately and then glued or diffusion-welded at lower temperatures to the MMC chip. In both cases, a *mechanical force* needs to be applied to the MMC chip which may also damage critical structures. To avoid such damages, the paramagnetic sensor is spatially separated from the bond pads used to contact the chip and also from the region where many vertical interconnect accesses are placed, as depicted in figure 4.2. The detector geometry parameters, such as the sensor area, the line width and pitch of the meander-shaped pickup coil are as provided in the detector optimization calculations (see table 4.1).

Using an appropriate thickness of the insulation layer ensures that the electrical insulation between sensor and pickup coil can be maintained, e.g. when applying pressure to the absorber during a gluing or diffusion-welding process. A symmetrical and rather

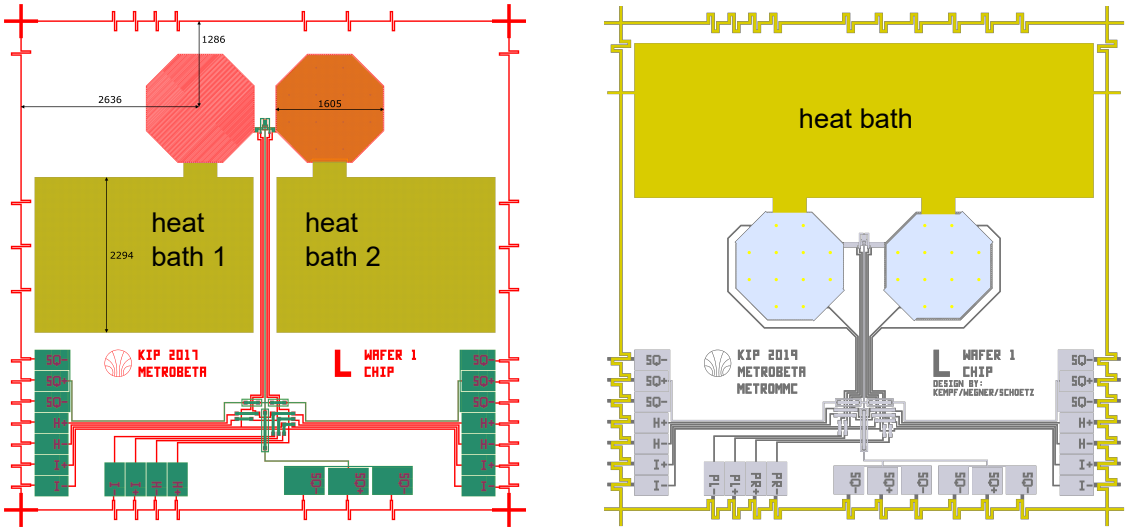

Figure 4.2: MetroBeta V1 **(left)** and V2 **(right)** MMC designs for size L. To allow for a uniform thermalization, the heat baths were unified in the second design. An optional on-chip electrical resistance heater (bond pads: PL±, PR±) was also realized on the chip. This allows for on-chip calibration via defined current pulses although initial tests indicate that using an external calibration source is more accurate.

straightforward absorber geometry would be a cylinder which is large enough to reach an absorber quantum efficiency of up to 100%. A cylindrical absorber shape suggests using a circular sensor geometry. Since circular designs are difficult to realize, it was decided to fabricate an octagonal sensor geometry as an approximation. The sensor was connected to a large on-chip heat bath via a sputter-deposited metal link made of Au. The ratio of the length and cross-section of the link is matched to the target decay time of the detector. Thus, the on-chip heat bath can be thermally connected to the sample holder, which is attached to the base plate of the cryostat. Since the MMC research groups within the MetroBeta and MetroMMC project use contrasting detector modules, it is purposeful to realize appropriate bond pad configurations. For this reason, the fabricated MMC chips have three complete sets of bond pads on the detector chip. All associated bonding pads are electrically routed to a common summing point such that the detector performance should not depend on the chosen bond pad set.

4.3 Absorber and sample preparation

An array of M/L Au absorbers was prepared with high speed milling from a 5N (99.999%) Au foil of 90 µm thickness, as depicted in figure 4.3. Next, the absorber

array was prepared for source embedding by cleaning it with organic solvents, strong acids or bases and distilled water.

There are several methods to embed a radionuclide source into 4π absorbers: ion implantation [Sch16] is a laborious technique which requires dedicated facilities but yields very pure embedded samples. For some radionuclides high-quality sources can be prepared using electrodeposition [Loi18, Koe21]. For the samples of this experiment, however, automatic drop deposition [Ver09] was used. Manual drop deposition allows for the dispensing of small volumes in the order of 0.1 µl which corresponds to a dried drop diameter of $\sim 1000\,\mu m$. Thus, the manual method is not appropriate for absorbers with an area smaller than approximately $1.5 \times 1.5\,mm^2$. In the case of a Au absorber this corresponds to using an MMC detector of at least size L. However, for typical radionuclide carrier solutions (e.g. ^{36}Cl in 0.05 mol/l NaOH, 33 mg/l NaCl), state of the art automated micro dispensers are able to deposit single drops with volumes of less than 50 picoliters and a placement accuracy of 20 µm. This corresponds to a dried drop diameter of approximately 70 µm. A carrier solution (0.1 mol/L NH_3 and ammonium pertechnatate NH_4TcO_4) was dispensed on every other M absorber using the micro dispenser. The Urlösung had an activity of approximately 170 kBq but was diluted such that the deposited volume of $\sim$ nl/absorber yielded an activity of approximately 5 Bq and 10 Bq, respectively. A qualitative autoradiography measurement was performed on the absorbers, as depicted in figure 4.3.

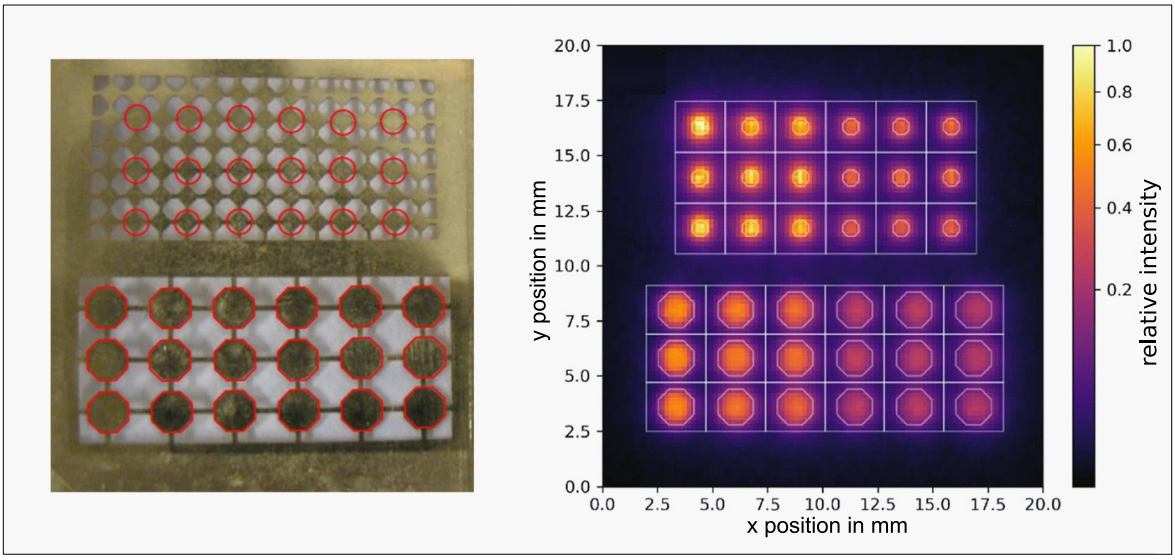

Figure 4.3: Gold absorber array **(left)** and an autoradiography plot of the dispensed array **(right)**. The absorber array was dispensed with a nominal total activity of 10 Bq/absorber and 5 Bq/absorber on the left and right array half, respectively.

After depositing the radionuclide on the surface of an array of absorber halves, the array was mounted on an aluminum/glass assembly and a second absorber-half array of the same shape and thickness but without any radioactive source was placed on top of it. Another glass/aluminum plate was put on top of the absorber-source-absorber

sandwich and screws of the assembly were fastened to produce a pressure of approximately 1.5 N/mm^2. The glass plates are used in order to avoid diffusion welding the aluminum of the pressing apparatus to the Au absorber.

To ensure a leak-proof diffusion welding of the gold foils, as depicted in figure 4.4, the assembly was put into an oven. In general, the appropriate duration and temperature depends on the chemical properties of the carrier solution salts, such as their melting and boiling points. When the solution had dried, Tc_2O_7 crystals remained on the absorbers. Since the melting point of the compound is 119.5 °C, the diffusion welding was done with slow temperature ramping: i.e. 45 minutes to reach 140 °C and 40 h at 140 °C followed by a cooldown of 12 h. A pressure of 10 Nm per screw was used for the isostatic pressing apparatus.

When the assembly had cooled down, the individual absorbers were cut out from the array using a scalpel. The next challenging task was to mount the small absorber onto the MMC detector where it had to remained fixed during the overall experiment. This was done in several steps where first, employing a semi-automatic component placement device, droplets of Stycast 1266 were placed on the posts of the MMC sensor using a thin wire. The absorber was put on top of the epoxy glue droplets using the placement device, applying a force of approximately 1 N for a few minutes to get an initial adhesion between the two surfaces. However, to ensure a tight thermal connection between absorber and MMC sensor, after the initial adhesion, a larger force of approximately 10 N was applied to the absorber with a custom-built assembly.

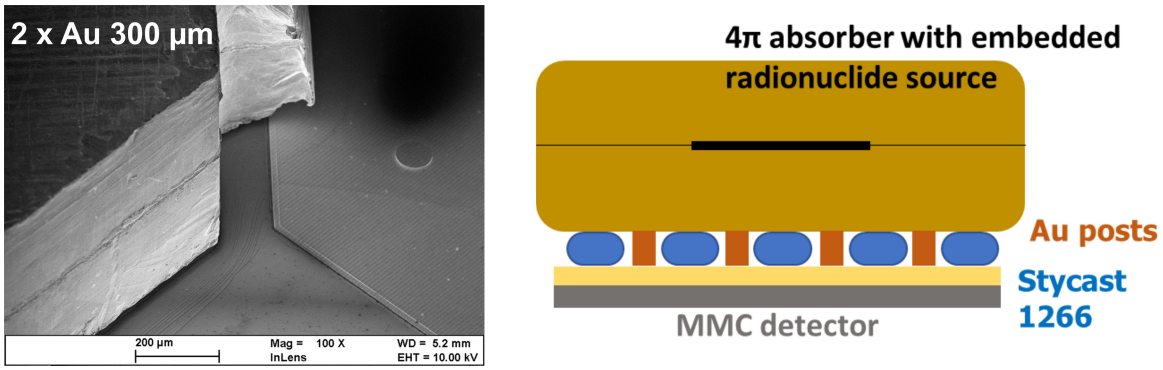

Figure 4.4: Scanning electron microscope image of a diffusion welded XL absorber (2× Au 300 µm) mounted on an XL MMC detector **(left)** and schematic picture **(right)**.

The M Au absorber that was used for the ^{99}Tc measurement had a nominal diameter of 700 µm and a thickness of 2×90 µm. Using the microdispenser, a deposited source having a diameter of at most 500 µm could be expected. The deposited energy for such an absorber and source was simulated using the Monte Carlo-code EGSnrc [Kaw18] and 10^7 samples from the ^{99}Tc ($E_{\max} = 293.8$ keV) beta spectrum provided by the software [Tcd20]. This yielded a quantum efficiency of 99.73% and negligible spectrum distortions that showed no particular trend.

The beta spectrometer [Loi18, Pau19] setup featured a detector module consisting of a gold-plated copper support structure which is operated at $\sim$ 20 mK in a commercial dilution refrigerator (BlueFors LD250). The support structure held the MMC detector and SQUID sensor, as depicted in figure 4.5. The microfabricated MMC chip (MetroBeta V2: W4-B6-M) and SQUID chip (PTB X1: C636-P33-C6X114W) devices were glued to the detector module with Stycast 1266 and GE Varnish, respectively. A slit in the support structure separated the chips to reduce parasitic thermal coupling. An absorber with a fully embedded, drop-deposited ^{99}Tc source was mounted on the left pixel while an empty absorber was mounted on the right pixel of the MMC. Thus, the background and spectral effects due to the calibration source could be measured as the ^{57}Co energy calibration source reaches both pixels. The external calibration source had an activity of approximately 37 kBq and the aperture of the lead collimator was $2\times250\,\mu$m and its distance to the top of the absorber was approximately 1.5 mm. To avoid scattered Auger and conversion electrons due to the external calibration source, the Pb collimator was covered with a 1 mm thick Al foil to stop these low-energy electrons.

Superconducting NbTi wires and copper wires were used to connect the exterior electronics to the Printed Circuit Boards (PCBs) of the MMC detector and SQUID sensor, respectively. While the exterior electronics were at room temperature during the experiment, sufficient thermalization to the base temperature was realized with Au bonds from the MMC detector and the SQUID sensor to the PCB/gold plated copper support structure. Further electrical connections were realized with superconducting Al bonds (PCB$\leftrightarrow$MMC/SQUID and MMC$\leftrightarrow$SQUID). A superconducting magnetic shielding made of aluminum was used during measurement to protect against magnetic background.

4.4 Data acquisition and handling

To read out the SQUID current sensor [Dru07], a state-of-the-art commercial SQUID electronics device (Magnicon XXF-1-6/2 + CSE-2) was used. It featured a two channel Flux Locked Loop (FLL) that additionally allowed for injecting a meander current into the MMC detector of up to 150 mA with a maximum heat switch current of 20 mA. The SQUID FLL output voltage signal was read out using a commercial PCIe digitizer card (Alazar ATS 9462). It has two channels which are sampled at 16-bit resolution, each having a maximum sampling rate of 180 MS/s per channel with an input range from $\pm$200 mV to $\pm$16 V. The custom-built measurement routine, which featured an automatic reset functionality that enables resuming the measurement when the SQUID electronics lose lock, was developed in LabVIEW. The temperature stability was monitored with a control algorithm in the dilution refrigerator software. As described above, the output data of the measurements in the setup were pulses.

In principal, there are two modes of measurement for the setup: a) triggered mode i.e. recording pulse windows for all signals that exceed a certain voltage level, which is

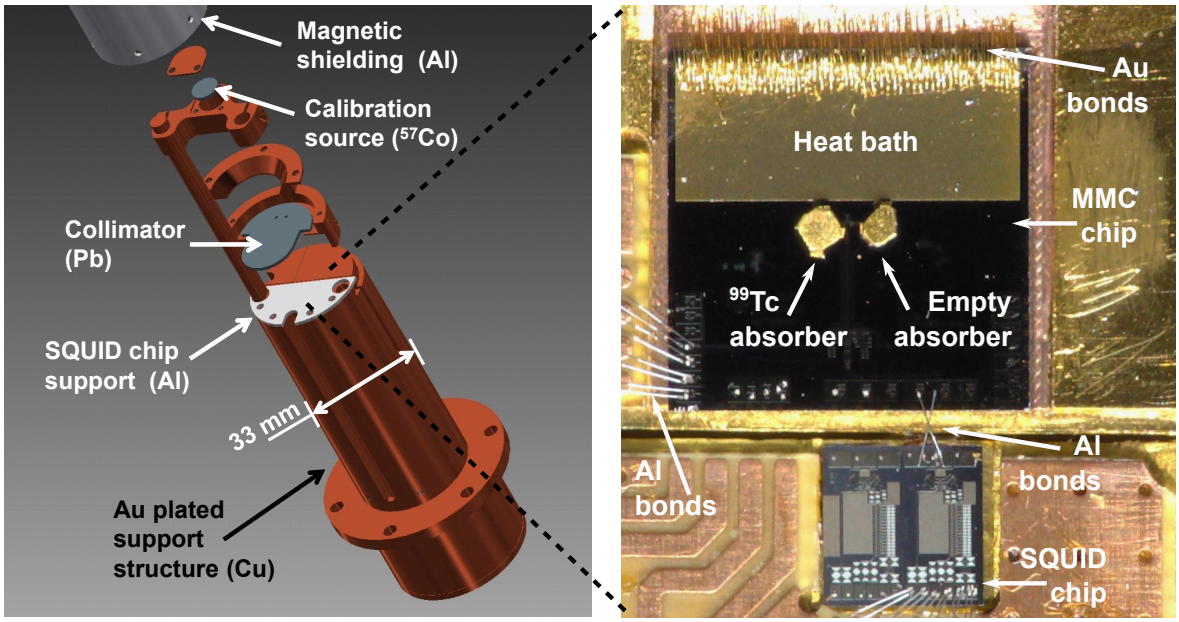

Figure 4.5: Sketch of the detector module **(left)** and image of the MMC detector with mounted absorbers and bonds **(right)**.

implemented in the digitizer hardware and b) continuous data acquisition i.e. recording every data point, as depicted in figure 4.6. To measure a beta spectrum with high

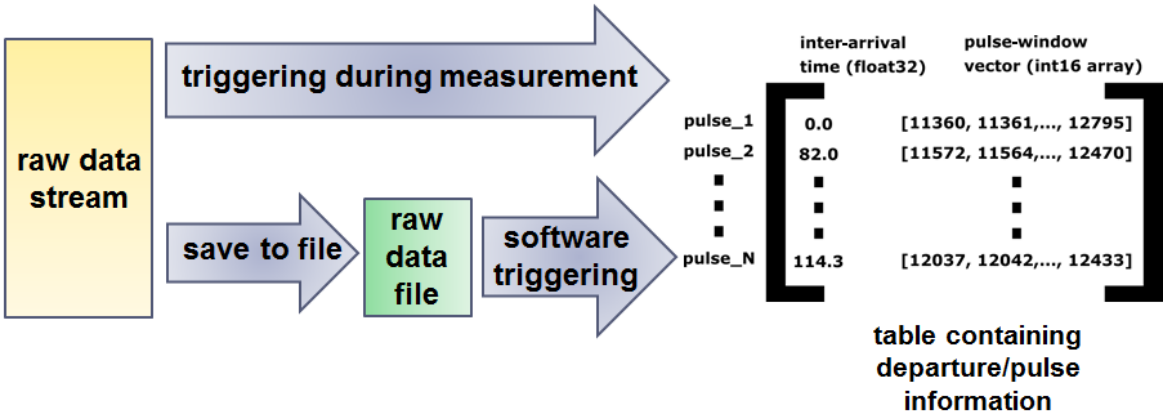

Figure 4.6: Overview of the measurement and trigger modes.

resolution, a histogram of pulse amplitudes with energy calibrated pulses needs to be recorded. The number of required pulses for a 1000 bin spectrum is on the order of $5 \cdot 10^6$. Realistically, the pulses have a 10/90 rise time $\sim 10\,\mu s$ and a 90/10 fall time $\sim 10\,ms$. Assuming an exponential pulse shape and requiring that the pulse height returns to less than 5% of its maximum pulse amplitude, would demand a pulse window of approximately 20 ms (e.g. a pre- and post-trigger of approximately 10 ms). At 4 Bq source activity, one has a pile-up probability (at least one decay occurring during the post-trigger of a previous pulse) of approximately 4% with the conventional assumption of the number of radioactive decays in a time frame being Poisson distributed.

The amount of unresolved pile-up, i.e. the probability for at least one decay on the rising flank (1/99 rise time 20 µs) is in the order of 80 ppm. To measure $5 \cdot 10^6$ pulses, the required measurement time is approximately 14 days. Using a sampling rate of 100 kS/s the size of the measurement data sets would be about 20 GB [triggered mode] and 250 GB [continuous data acquisition], respectively.

When using the trigger mode, pulse windows are only recorded around points exceeding the previously set trigger level, i.e. significant departures from the baseline and saved in binary data format files. While a trigger mode measurement is less data intensive and practical for measuring pulses with a high signal to noise ratio (e.g. lines of calibration sources at higher energies), low energy pulses may get lost due to poorly defined trigger levels. Thus, we currently focus on continuous data acquisition with subsequent software triggering.

If the measurement mode is continuous, every data point is saved into a raw data file in binary format. Since the data sets are rather large it is important to have sensible data handling and sorting algorithms, an overview of the chosen approach is depicted in figure 4.7. The procedures were implemented in Python [vRo95] using compiled code packages such as NumPy, pyTables and pandas to decrease the computation time. Before processing the large data sets, it is useful to study the noise level in the signal baseline and pulses manually e.g. to estimate the rise and fall times as well as pulse height ranges to set an appropriate trigger level and other processing parameters. When the measurement is finished, the time series of the entire data stream is

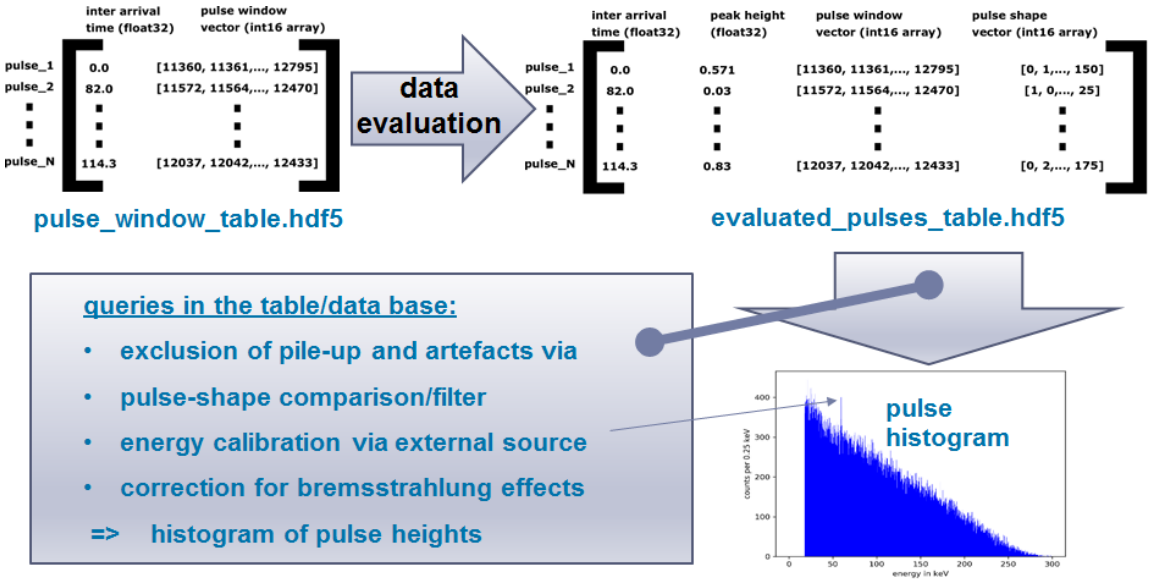

Figure 4.7: Overview of the data evaluation routines, at the bottom right the pulse histogram of a test measurement of ^{99}Tc is depicted.

software triggered to extract the pulse windows. This is achieved by finding departures (peaks/valleys) from the signal baseline. Several kinds of triggers can be used e.g. a slope path trigger which finds consecutive points having a positive/negative

slope and when the slope crosses zero which can be used to get a first estimate of the pulse height. Alternatively, a Constant Threshold Discriminator (CTD) and a Constant Fraction Discriminator (CFD) trigger can be used, see e.g. [Abb16, Ogr19]. When a signal has been found, the peak/valley start index is recorded along with the pulse window i.e. a vector of data points before and after that index. The processing parameters of the algorithm e.g. the slope and window length are set by the user and can be estimated by studying individual pulses before recording the data set (a similar preparation is necessary for the trigger mode option). At 100 kS/s approximately five sample points are recorded for a typical 10/90 rise time of 50 µs and this is sufficient for the software triggering algorithm.

The processed data is collected in a pulse table in the hdf5 format [HDF19], which is a compact, cross-platform compatible binary data format, that is optimized for efficient data querying pulse_window_table.hdf5 in figure 4.7). The pulse table is further evaluated, creating an evaluated pulse table where properties such as pulse-height estimates, inter-arrival times and normalized pulse shapes are calculated (evaluated_pulses_table.hdf5 in figure 4.7. Now, queries on the evaluated pulse table can be used to select data e.g. for pile-up rejection and pulse-shape classification.

5

Measurement results and analysis

In the first part of this chapter, the experimental results of measuring the beta spectrum of ^{99}Tc with the MMC based beta spectrometer are presented. We will begin by describing the detector performance in terms of magnetization, signal shape and energy resolution. The main part is considered with the spectral evaluation of the measurement data of the active pixel and the non-active pixel along with their energy calibration. A comparison of the extracted beta spectrum is done with other measurements and a state-of-the-art calculation.

The issue of sub-optimal quantum efficiency in high energy beta spectrometry with microcalorimeters is addressed in the second part of the chapter. In such cases, the energy losses of the absorber lead to spectral distortions which can be formulated as an unfolding problem. A novel, matrix-inversion based algorithm is proposed as its solution. The accuracy of the algorithm is demonstrated on simulated data of the beta emitter ^{36}Cl.

5.1 An MMC beta spectrum of ^{99}Tc

Several test runs were done with the setup described in chapter 4 in order to optimize its performance. This involved reducing vibrations by finding the most stable position for the detector module on the bottom plate of the cryostat, adjusting the lead collimator to set the illumination level of the pixels from the calibration source and finding the optimal persistent current, as described in the following.

5.1.1 Detector performance

By varying the base temperature of the cryostat for several fixed values of the persistent current, the resulting magnetic flux change in the SQUID was measured. Since the

magnetization of Ag:Er is strongly temperature dependent, the characteristic curves were recorded and are depicted in figure 5.1. For each persistent current, pulses were recorded at the typical operating temperature of $\sim 20\,\mathrm{mK}$. The largest pulse signal was found for the persistent current of 80 mA which was thus used for the measurement.

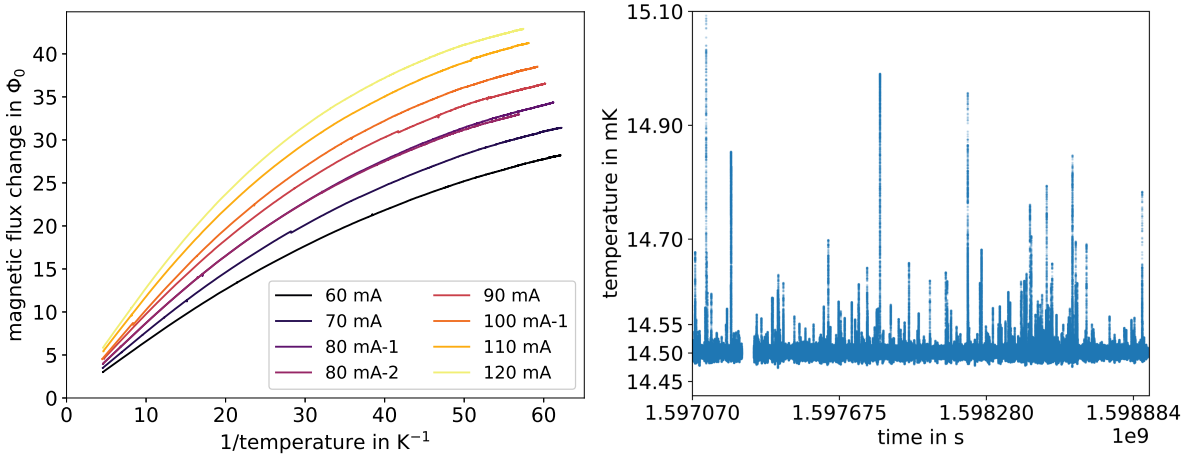

Figure 5.1: Magnetization curves of the detector for several different persistent currents (80 mA was used in the measurement) **(left)**, corresponding to the theoretical magnetization curves in figure 3.5. Temperature measured by the cryostat thermometer which was mounted on the bottom plate **(right)**. The tick interval length corresponds to one week.

The cryostat temperature was set to 14.5 mK, since this is a low level at which the refrigerator is still rather stable. Measurement data for the base plate temperature is depicted in figure 5.1. A persistent current of 80 mA was injected into the detector and measurement data were acquired for 505 h i.e. approximately 21 days and sampled at 200 kS/s. The gap in the recording of data was due to a software update of the measurement PC. However, the persistent current in the MMC remained intact and the SQUID FLL was still in lock, such that the measurement intervals are fully compatible concerning the experimental parameters. The resulting binary files were 678 GB in size and triggered in offline mode i.e. on the saved measurement data after the experiment was finished.

An optimized constant fraction discriminator trigger was used to evaluate the active pixel (^{99}Tc/^{57}Co) for positive polarity pulses and the non-active pixel (^{57}Co) for negative polarity pulses, respectively. The trigger level was set to the 3σ-level, where σ denotes the standard deviation of the pre-trigger noise. Thus, a pulse needs to be at least three times above the standard deviation of the noise in order for the trigger to respond. The number of triggered events was approximately $6.26 \cdot 10^6$ ($5.95 \cdot 10^6$ positive and $0.31 \cdot 10^6$ negative pulse events).

The next part of the evaluation consisted in constructing an optimal filter for the triggered data. This procedure was done separately for each pixel, as the pulses have reverse polarities and slightly different pulse shapes. The first step was to create an

initial average template pulse, which was done by visual inspection. Around 100 pulses of a wide range of voltage amplitudes were selected and their average along with the baseline noise were used to create an initial optimal filter, which was applied to the triggered data and noise. To improve the optimal filtering, an average based on a larger pulse population was constructed by calculating the so-called χ^2-value for each pulse i.e. the weighted sum of its squared deviation from the initial average template pulse. Using this information, pulse windows that contain pile-up or other distortions can effectively be rejected and a more representative average template pulse could be constructed by selecting pulse populations with reasonably low χ^2-values. Also, limits were set on the root-mean-square value of the pre-trigger noise, i.e. the baseline values before the triggered event within the pulse window, to avoid pulses that occurred when the detector was not in thermal equilibrium. The updated optimal filter was then applied to the triggered data once again. Plots of the resulting FFT spectra and template pulses for the active and non-active pixel are depicted in figure 5.2.

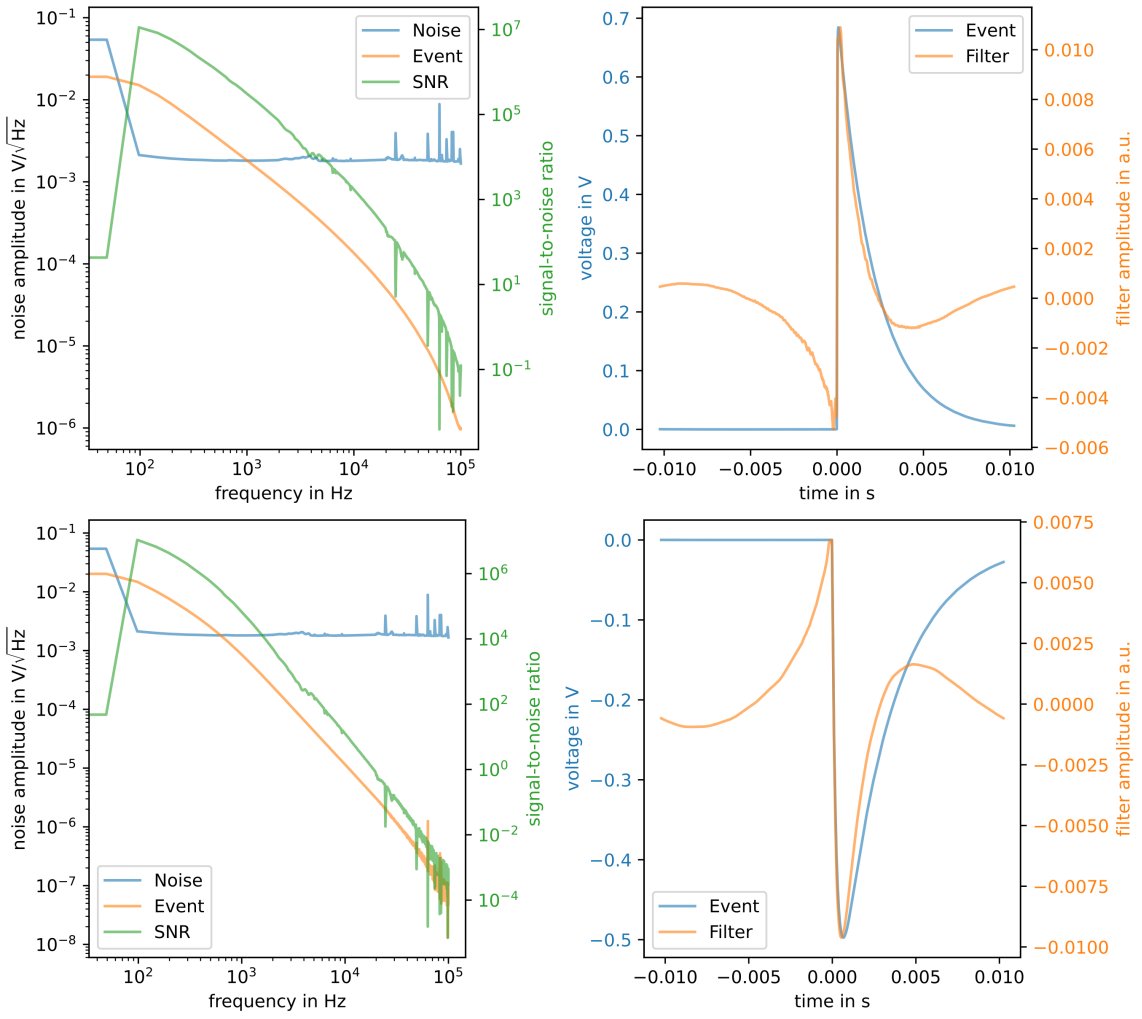

Figure 5.2: FFT spectra and template pulses for the active [non-active] pixel **(top row)** [**(bottom row)**].

For the active pixel containing the ^{99}Tc sample (pixel with positive polarity) illuminated with the external ^{57}Co source, the 10/90 rise time and 90/10 decay time are 30 µs and 4 ms, respectively. The peaks in both noise spectra above 10 kHz are likely caused by electromagnetic background disturbances that affects the wiring and electronics at room temperature. The empty absorber (pixel with negative polarity) illuminated with the external ^{57}Co source has a slightly different pulse shape. On this pixel the pulses have 10/90 rise times and 90/10 decay times of 300 µs and 7 ms, respectively.

By making a histogram of the respective baseline data points and fitting a Gaussian function to it, the energy resolution i.e. the FWHM[1] value at 0 keV can be determined, see figure 5.3. Since each pixel has its own optimal filter, the energy resolutions concerning the baseline are not identical and these reflect the individual detection performance of each pixel.

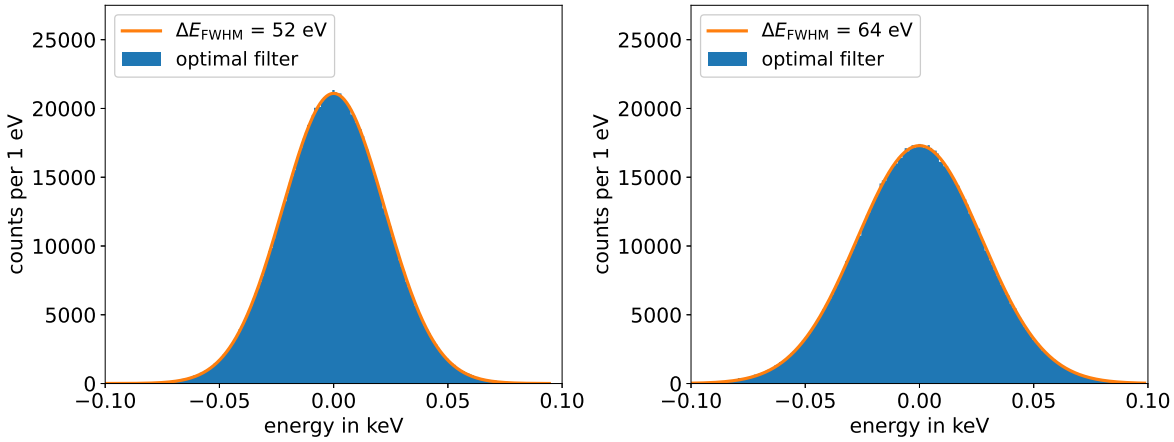

Figure 5.3: Energy resolutions at 0 keV for the active pixel **(left)** and the non-active pixel **(right)**. Gaussian functions were fitted to the histograms and centered at 0 keV. One has $\Delta E_{\mathrm{FWHM}} = 2\sqrt{2\ln 2}\sigma$, where σ denotes the standard deviation.

The average pulses of the pixels, in particular the rise and decay times, in figure 5.2 indicate that the thermalization of the active pixel is faster than that of the non-active pixel. This agrees with the corresponding energy resolutions of 52 eV and 64 eV found at 0 keV in figure 5.3 and qualitatively with formula (3.22). The latter yields lower limits for the energy resolution of 5 eV and 7 eV when only the thermodynamic fluctuations of the detector are considered at 14.5 mK. A more realistic energy resolution under completely optimized experimental conditions can be calculated when the other noise sources, in particular by the SQUID, are considered. Such values are given in table 4.1 and at 20 mK i.e. slightly above the nominal cryostat temperature, the energy resolution for the MetroBeta M detector is given by 19.1 eV.

Each of the filtered pulse's shape was again compared to the template pulse by calculating its χ^2 deviation. When these values are plotted against the calculated amplitude

[1] FWHM = Full Width at Half Maximum

of each pulse, clusters of pulse populations emerge which corresponds to lines from the ^{57}Co calibration source and the ^{99}Tc continuous beta spectrum, respectively. These populations were selected using quadratic functions, as depicted in figure 5.4.

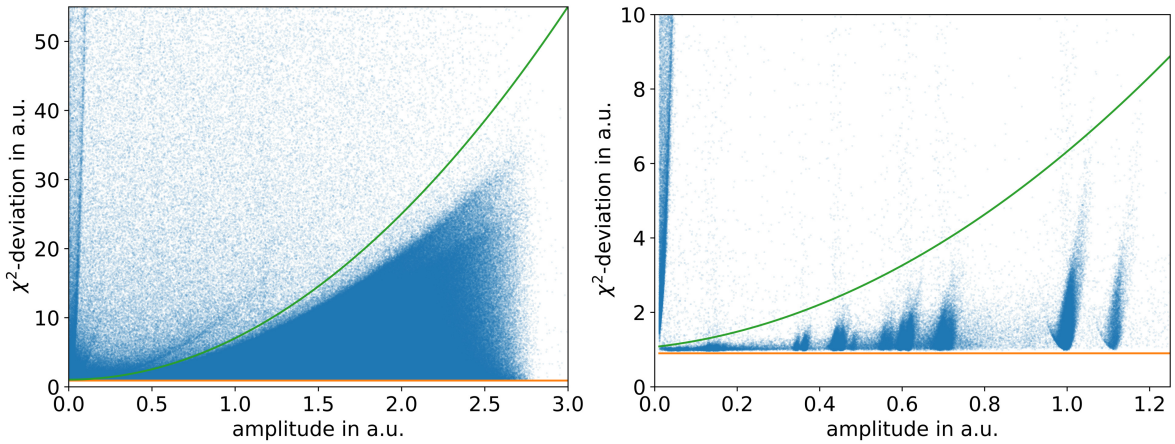

Figure 5.4: Clustering of pulse populations for the active pixel that had an absorber with an embedded ^{99}Tc sample **(left)** and lines of the non-active pixel which had an empty absorber **(right)**. Each blue dot corresponds to one detected pulse event. Both pixels were illuminated with ^{57}Co that has a line spectrum, whose pulse population is immersed in the continuous spectrum on the left but can easily be seen on the right. Pulse populations below [above] the green [orange] line are selected for further analysis, respectively.

The cuts were done such that the possible noise triggers having very small amplitudes and rather large χ^2 deviations were avoided while selecting as many of the true pulses as possible. From the selected pulse population, a histogram is plotted which is depicted in figure 5.5 for the active pixel. It contains a first approximate, linear energy calibration. The energy calibration was done by locating a dominant line in the ^{99}Tc/^{57}Co spectrum which corresponds to an intense, well-known line from the calibration source (^{57}Co γ at 122.06 keV). However, a continuous spectrum with several broad peaks can be observed. Their widths of several keV neither reflect the energy resolution of the detector nor the width of the calibration lines. Apparently, these simply determined pulse amplitudes do not correspond to the actual pulse energies very well. The reason is that over long time intervals, there are small temporal baseline fluctuations before a pulse gets triggered i.e. in the so called pre-trigger, which affect the determination of the pulse heights using the evaluation code. Thus, a reference level needs to be found for the pre-trigger level and the corrected pulse amplitude values need to be coupled with well defined energies.

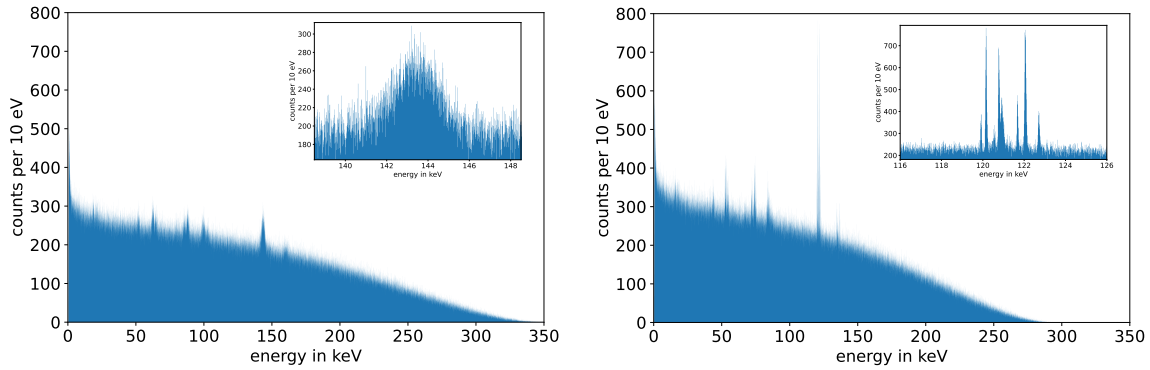

Figure 5.5: The measured ^{99}Tc/^{57}Co spectrum before **(left)** and after **(right)** an amplitude correction has been done with a specific linear calibration to one calibration pulse population. **Insets**: instead of one wide peak **(left)**, several thin peaks have emerged **(right)**.

5.1.2 Temporal correction of small baseline shifts

Over rather long time intervals of up to several days, the detector baseline is very stable and free from shifts. When the amplitude of each pulse is plotted over its pre-trigger offset, as shown in figure 5.6, straight lines can be identified which correspond to the detected 122.06 keV-photons from the external calibration source.

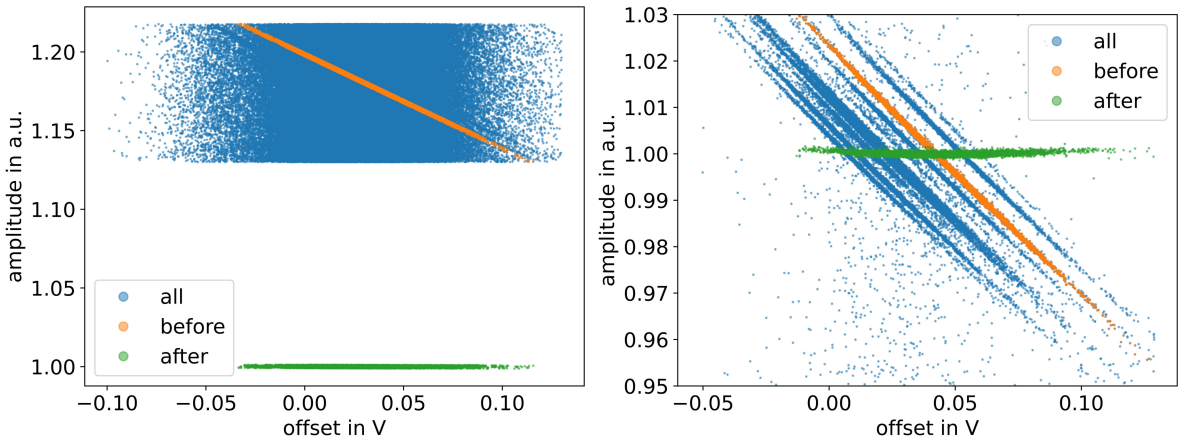

Figure 5.6: The 122.06 keV calibration line of ^{57}Co was identified and its amplitude values were linearized in relation to the offset for the active pixel **(left)** and the non-active pixel **(right)**. Each blue dot corresponds to one detected pulse event. The fact that there are several lines reflects that there are jumps in the pre-trigger, the width that there is noise and the slope that there is a drift component. For the active pixel the line emerges when zooming in more closely.

The next step was to correct for the small jumps and for each pulse acquired from the active pixel, the offset of the pre-trigger baseline was plotted against the amplitude. Since the offset contains jumps, several pulse populations for the 122.06 keV calibration

line could be identified within the beta spectrum pulse population. A linear fit was done and the amplitudes of the entire pulse population were corrected accordingly, as depicted in figure 5.6.

In a second step, the linearly corrected population was corrected for its temporal fluctuations using a spline fit, as depicted in figure 5.7. The noise and drifts are likely to be

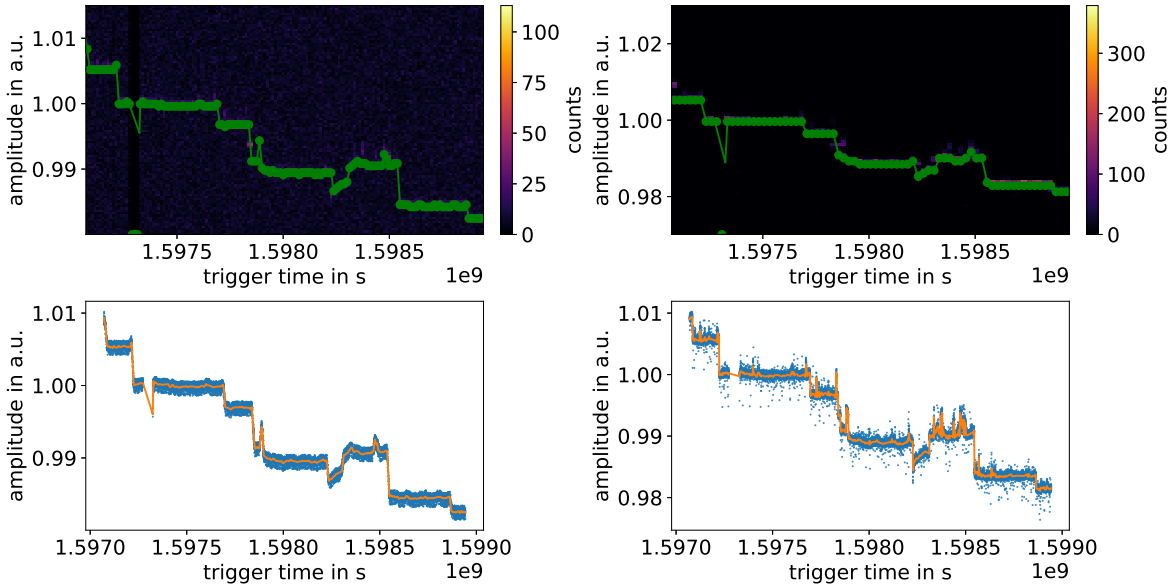

Figure 5.7: The calibration line amplitude fluctuations were corrected using an interpolating cubic spline fit for the active pixel **(left column)** and the non-active pixel **(right column)**. Each blue dot corresponds to one detected pulse event, while the spline fit is depicted in green and orange, respectively.

caused by thermal effects but the jumps are probably due to small and sudden changes in the on-chip magnetic field. There are several superconducting structures that hold persistent currents and when one of these traps or loses magnetic flux quanta, such jumps may occur due to a change in magnetization of the paramagnetic sensor.

5.1.3 Calibration peak identification and fitting

After the first linear calibration for the offset corrected amplitudes had been done, histograms were plotted once more. See figures 5.8 and 5.9 for the active and non-active pixel, respectively. Now, several peaks at energies that correspond to lines caused by the external ^{57}Co calibration source could be identified. Throughout, experimental literature values and uncertainties were used as references for the ^{57}Co calibration [Be16] and observed X-ray transition [Des03] energies. The peaks were fitted with a Gaussian density on a quadratic background, by finding the parameters for the following function of the energy E

$$g(E) = \frac{A}{\sqrt{2\pi}\sigma} e^{\frac{(E-\mu)^2}{2\sigma^2}} + a \cdot E^2 + b \cdot E + c, \tag{5.1}$$

where A denotes the Gaussian peak amplitude, μ the mean i.e. the central peak energy and σ its standard deviation. a, b and c are background parameters which vary freely. The statistical uncertainty of the energy position of the fitted peaks are given by $\frac{\sigma}{N_{\text{peak}}}$, where N_{peak} denotes the number of counts in the Gaussian peak i.e. when the background has been subtracted. The bin width of 10 eV was chosen such that the FWHM of a Gaussian fit function concerning an identifiable calibration peak in the histogram is at least five bins.

The identified peaks are annotated along with their energetic position in figures 5.8-5.9 and listed in tables 5.1-5.2.

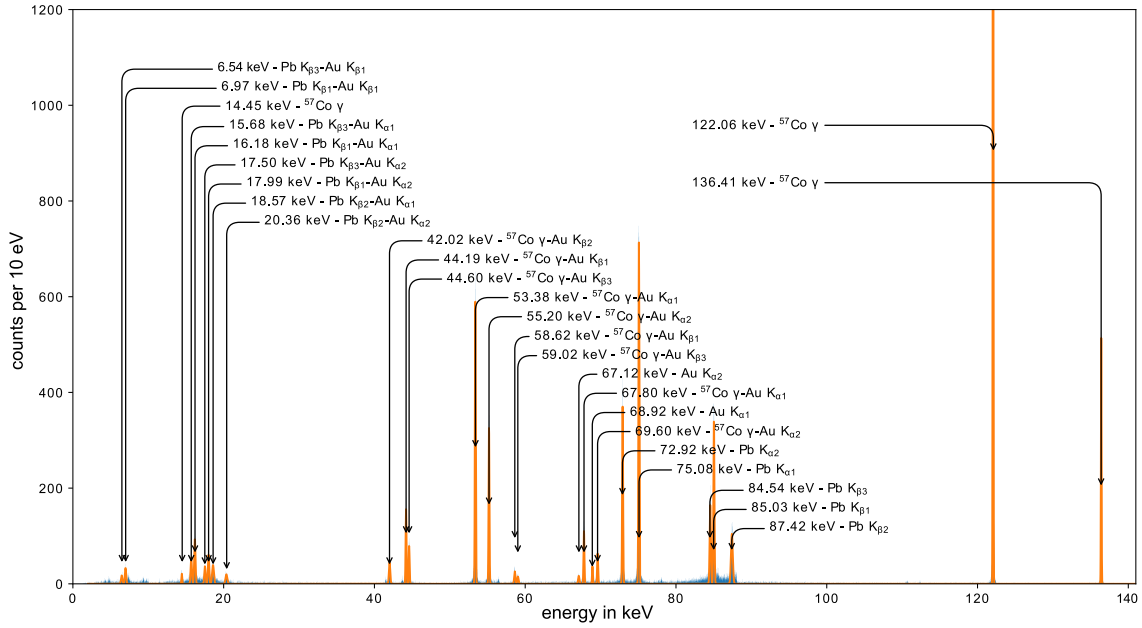

Figure 5.8: The measured spectrum of ^{57}Co with annotations for the detected peaks. There are $0.13 \cdot 10^6$ counts in the spectrum.

From figure 5.8 it is evident that other interactions than just full energy deposition of the emitted particles from the calibration source into the Au absorber of the MMC are detected. Indeed, the ^{57}Co gamma particle source interacts significantly with the setup on its way to the Au absorber e.g. via the Pb collimator.

Firstly, there are native lines due to the electron capture decay of ^{57}Co. Secondly, there are fluorescent lines of Au and Pb such as the Pb $K_{\alpha 1}$-line at 75.08 keV. Thirdly, there are so called escape lines which arise when a photon of energy E from the calibration source hits an electron in an atom of the absorber. This causes a hole in an electron shell of the Au atom. The hole can be filled with an electron that transitions from a higher energy level and a photon of energy $E^{\text{ph}}_{\text{Au}}$ is thereby emitted. If this photon then leaves the absorber, the energy $E - E^{\text{ph}}_{\text{Au}}$ is detected. The ^{57}Co γ-Au $K_{\alpha 1}$ line at 53.36 keV is an example of such an escape mechanism.

Table 5.1: Identified peaks in the ^{57}Co spectrum after linear calibration to the ^{57}Co γ line at 122.06065 keV.

Peak type	**Lit. value in keV**	**Uncert. in eV**	**Exp. value in keV**	**FWHM in eV**	**Events in peak**	**Stat. error in eV**	**Difference in eV**
Pb $K_{\beta 3}$ - Au $K_{\beta 1}$	6.47065	0.98	6.5373	218	134	8.0	66.6
Pb $K_{\beta 1}$ - Au $K_{\beta 1}$	6.95928	0.72	6.9709	144	324	3.4	10.6
^{57}Co γ	14.41950	0.31	14.4510	58	141	2.1	31.5
Pb $K_{\beta 3}$ - Au $K_{\alpha 1}$	15.64595	0.78	15.6830	138	542	2.5	37.1
Pb $K_{\beta 1}$ - Au $K_{\alpha 1}$	16.13458	0.52	16.1758	146	1018	1.9	41.3
Pb $K_{\beta 3}$ - Au $K_{\alpha 2}$	17.45972	0.82	17.5068	205	568	3.7	47.1
Pb $K_{\beta 1}$ - Au $K_{\alpha 2}$	17.94835	0.56	17.9983	161	712	2.6	50.0
Pb $K_{\beta 2}$ - Au $K_{\alpha 1}$	18.49795	0.77	18.5747	240	612	4.1	76.7
Pb $K_{\beta 2'}$ - Au $K_{\alpha 2}$	20.31172	0.33	20.3561	234	315	5.6	44.4
^{57}Co γ - Au $K_{\beta 2}$	41.92955	0.54	42.0209	174	782	2.6	91.4
^{57}Co γ - Au $K_{\beta 1}$	44.08085	0.50	44.1932	112	1834	1.1	112.3
^{57}Co γ - Au $K_{\beta 3}$	44.48564	0.73	44.6043	117	968	1.6	118.7
^{57}Co γ - Au $K_{\alpha 1}$	53.25615	0.30	53.3813	115	4500	0.7	125.2
^{57}Co γ - Au $K_{\alpha 2}$	55.06992	0.34	55.1981	124	4408	0.8	128.2
^{57}Co γ - Au $K_{\beta 1}$	58.49376	0.67	58.6220	111	351	2.5	128.2
^{57}Co γ - Au $K_{\beta 3}$	58.89855	0.90	59.0260	115	193	3.5	127.5
Au $K_{\alpha 2}$	66.99073	0.22	67.1158	137	217	4.0	125.1
^{57}Co γ - Au $K_{\alpha 1}$	67.66906	0.11	67.7936	115	1326	1.3	124.5
Au $K_{\alpha 1}$	68.80450	0.18	68.9230	113	409	2.4	118.5
^{57}Co γ - Au $K_{\alpha 2}$	69.48283	0.07	69.6060	121	790	1.8	123.1
Pb $K_{\alpha 2}$	72.80542	0.24	72.9221	127	5160	0.8	116.7
Pb $K_{\alpha 1}$	74.97011	0.17	75.0807	124	9310	0.5	110.6
Pb $K_{\beta 3}$	84.45045	0.60	84.5419	130	2167	1.2	91.4
Pb $K_{\beta 1}$	84.93908	0.34	85.0312	132	4650	0.8	92.1
Pb $K_{\beta 2}$	87.30245	0.55	87.4190	197	2021	1.9	116.5
^{57}Co γ	122.06065	0.12	122.0602	92	29732	0.2	-0.4
^{57}Co γ	136.47356	0.29	136.4126	92	4658	0.6	-61.0

Table 5.2: Identified peaks in the ^{99}Tc/^{57}Co spectrum after linear calibration to the ^{57}Co γ line at 122.06065 keV.

Peak type	**Lit. value in keV**	**Uncert. in eV**	**Exp. value in keV**	**FWHM in eV**	**Events in peak**	**Stat. error in eV**	**Difference in eV**
Pb $K_{\beta 3}$ - Au $K_{\beta 1}$	6.47065	0.98	6.4438	49	486	0.9	-26.8
Pb $K_{\beta 1}$ - Au $K_{\beta 1}$	6.95928	0.72	6.9728	77	610	1.3	13.5
^{57}Co γ	14.41950	0.31	-	-	-	-	-
Pb $K_{\beta 3}$ - Au $K_{\alpha 1}$	15.64595	0.78	15.7258	122	798	1.8	79.9
Pb $K_{\beta 1}$ - Au $K_{\alpha 1}$	16.13458	0.52	16.2163	48	821	0.7	81.7
Pb $K_{\beta 3}$ - Au $K_{\alpha 2}$	17.45972	0.82	-	-	-	-	-
Pb $K_{\beta 1}$ - Au $K_{\alpha 2}$	17.94835	0.56	18.0366	108	824	1.6	88.2
Pb $K_{\beta 2}$ - Au $K_{\alpha 1}$	18.49795	0.77	-	-	-	-	-
Pb $K_{\beta 2'}$ - Au $K_{\alpha 2}$	20.31172	0.33	-	-	-	-	-
^{57}Co γ - Au $K_{\beta 2}$	41.92955	0.54	42.0277	81	838	1.2	98.1
^{57}Co γ - Au $K_{\beta 1}$	44.08085	0.50	44.2349	107	1661	1.1	154.0
^{57}Co γ - Au $K_{\beta 3}$	44.48564	0.73	44.6580	141	1600	1.5	172.4
^{57}Co γ - Au $K_{\alpha 1}$	53.25615	0.30	53.4246	108	6169	0.6	168.5
^{57}Co γ - Au $K_{\alpha 2}$	55.06992	0.34	55.2392	102	3539	0.7	169.3
^{57}Co γ - Au $K_{\beta 1}$	58.49376	0.67	58.6250	122	675	2.0	131.2
^{57}Co γ - Au $K_{\beta 3}$	58.89855	0.90	-	-	-	-	-
Au $K_{\alpha 2}$	66.99073	0.22	-	-	-	-	-
^{57}Co γ - Au $K_{\alpha 1}$	67.66906	0.11	67.8279	110	1242	1.3	158.8
Au $K_{\alpha 1}$	68.80450	0.18	68.9510	114	647	1.9	146.5
^{57}Co γ - Au $K_{\alpha 2}$	69.48283	0.07	69.6513	69	532	1.3	168.5
Pb $K_{\alpha 2}$	72.80542	0.24	72.9763	105	3208	0.8	170.9
Pb $K_{\alpha 1}$	74.97011	0.17	75.1361	97	5445	0.6	166.0
Pb $K_{\beta 3}$	84.45045	0.60	84.5930	69	768	1.1	142.6
Pb $K_{\beta 1}$	84.93908	0.34	85.0900	87	2240	0.8	150.9
Pb $K_{\beta 2}$	87.30245	0.55	87.5073	217	1138	2.7	204.9
^{57}Co γ	122.06065	0.12	122.0624	67	20907	0.2	1.8
^{57}Co γ	136.47356	0.29	136.3839	72	3657	0.5	-89.7

Furthermore, combinations of the second and third effect are possible e.g. when a fluorescent line, which is generated at the Pb collimator by a gamma ray from the calibration source, knocks out an electron of the Au absorber and causes an energy escape such as the Pb $K_{\beta 1}$ - Au $K_{\alpha 1}$-line at 16.18 keV. While 27 lines were found in the background spectrum i.e. the non-active pixel illuminated by ^{57}Co, 21 lines could be identified on the active pixel as some of the peaks with small amplitudes are indistinguishable from the measured beta spectrum of ^{99}Tc, which is depicted in figure 5.9.

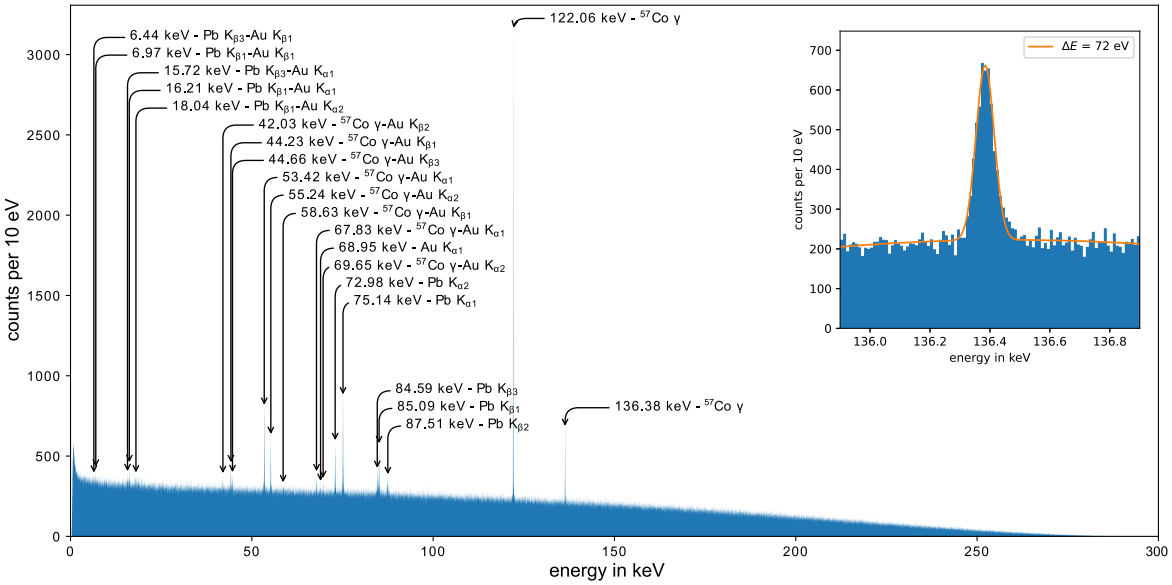

Figure 5.9: The measured ^{99}Tc/^{57}Co spectrum after linear calibration along with annotated peaks along with experimental energy values that were found with the Gaussian fit function (5.1). **Inset**: fitted peak at 136.38 keV. The spectrum contains $5.33 \cdot 10^6$ counts.

5.1.4 Non-linear energy calibration

MMC detectors are not perfectly linear devices, in the sense that the signal strength is an ideal linear function of the energy deposited in the absorber [Kem18]. In fact, the magnetization $M(T)$ of the paramagnet as well as the heat capacities C_{abs} and C_{sens} are temperature dependent and change due to the temperature increase of the deposited energy. Thus, the relative signal strength decreases subtly as the energy is increased and for high-precision measurements it is beneficial to do a non-linear energy calibration as follows.

To explain the procedure, we summarize some important evaluation steps so far. The optimal filtering of the triggered data results in a vector of voltage amplitudes $(a_1, \ldots, a_n)$ which are plotted in a histogram. After an approximate, linear calibration to the ^{57}Co γ line at 122.06065 keV, we were able to correct the amplitudes by mak-

ing a spline fit for the pre-trigger offset. This resulted in the high-resolution spectra of figures 5.8 and 5.9. These are calibrated, in the sense that the mean μ_{fit} of the Gaussian fit function was matched with the corresponding energetic reference value E_γ^{lit}=122.06065 keV. By multiplying the voltage amplitude vector $(a_1, \ldots, a_n)$ with the ratio $\frac{E_\gamma^{\text{lit}}}{\mu_{\text{cal}}}$, an energy scale is provided via a linear energy calibration. In the next step, k other significant peaks were localized, which lead to the values given in tables 5.1 and 5.2. Thus, we attained an array of energies $E_1^{\text{Exp}}, \ldots, E_k^{\text{Exp}}$ for these experimental data peaks in the linear energy scale.

Now, using these values and comparing them to the corresponding literature values $E_1^{\text{lit}}, \ldots, E_k^{\text{lit}}$ a non-linear function f^{fit}, which maps their voltage amplitudes to energies, can be fitted. The non-linear energy calibration is completed when the energy vector $\left(f^{\text{fit}}(a_1), \ldots, f^{\text{fit}}(a_n)\right)$ vector has been calculated, where n denotes the number of counts in the spectrum.

As is apparent from tables 5.1-5.2 above, not all peaks have separable lines due to the finite energy resolution of the detector. Others contain further background e.g. due to scattering effects or interactions with the Al foil which were not considered here. For this reason $k := 5$ significant peaks, that were common to both spectra and covered a large energy range, were chosen for the non-linear calibration of the active and non-active pixel, respectively. A quadratic ansatz was made for the fit function

$$E_i^{\text{lit}} = f^{\text{fit}}(a_i) := x_2 \cdot a_i^2 + x_1 \cdot a_i + x_0 \quad \text{for } i \in \{1, \ldots, 5\} \tag{5.2}$$

where $a_i := \frac{E_i^{\text{exp}}}{E_\gamma^{\text{lit}}}$ denotes the amplitude value i.e. the corresponding pulse height of the Gaussian fitted calibration line center. The object of the fit is to find the coefficients x_0, x_1 and x_2. As no energetic offsets needs to be assumed, the constant coefficient is set to zero. To allow for a simple calculation of the total calibration error via error propagation of the fitting in Python, the ODR[2] package was used [Odr21, Bog90] similar to the method for calibrating the MMC gamma detector in [Bat16]. An advantage of the ODR procedure is that it allows for including the errors on both axes i.e. the uncertainty of the literature values as well as the statistical uncertainty of the Gaussian fits to the experimental peaks.

The quadratic calibration is summarized in tables 5.3-5.4. The fit errors are defined as 3σ-errors calculated by the ODR procedure. For both pixels, the linear coefficient dominates the quadratic coefficient and the deviations from the literature values are greatly reduced, in particular for the active pixel where the largest deviation was -2.5(94) eV. Concerning the non-active pixel, one fitted calibration peak deviated by -13.7(66) eV from the literature value i.e. slightly more than the calculated error, which may be an indication of unidentified background in that energy interval.

[2]ODR = Orthogonal Distance Regression

Table 5.3: Non-linear calibration values of the non-active pixel (^{57}Co).

Peak type	E_i^{lit}: **lit. values in keV**	E_i^{exp}: **exp. value in keV**	$E_i^{\text{exp}} - E_i^{\text{lit}}$ **in eV**	$E_{\text{quad},i}^{\text{fit}} - E_i^{\text{lit}}$ **in eV**	**After quadratic calibration FWHM in eV**
Pb $K_{\beta 1}$ - Au $K_{\alpha 1}$	16.13458(52)	16.2163(7)	81.7(12)	1.8(27)	144
^{57}Co γ - Au $K_{\alpha 1}$	53.25615(30)	53.4240(6)	168.5(9)	-2.5(94)	122
Pb $K_{\alpha 1}$	74.97011(17)	75.1361(6)	166.0(7)	1.2(145)	124
^{57}Co γ	122.06065(12)	122.0624(2)	1.8(3)	0.1(290)	92
^{57}Co γ	136.47356(29)	136.3839(5)	-89.7(8)	-0.8(344)	95

For the non-active pixel, the corresponding fit function parameters were

$$\text{linear coefficient} = 121.58211072997264\ (\pm 0.013482355254566295)\ \frac{\text{keV}}{\text{V}}$$
$$\text{quadratic coefficient} = 0.4786294957347393\ (\pm 0.01356154303956029)\ \left(\frac{\text{keV}}{\text{V}}\right)^2,$$

with 1σ errors.

Table 5.4: Non-linear calibration values of the active pixel (^{99}Tc/^{57}Co).

Peak type	E_i^{lit}: **lit. values in keV**	E_i^{exp}: **exp. value in keV**	$E_i^{\text{exp}} - E_i^{\text{lit}}$ **in eV**	$E_{\text{quad},i}^{\text{fit}} - E_i^{\text{lit}}$ **in eV**	**After quadratic calibration: FWHM in eV**
Pb $K_{\beta 1}$ - Au $K_{\alpha 1}$	16.13458(52)	16.1758(19)	41.3(25)	-13.7(66)	49
^{57}Co γ - Au $K_{\alpha 1}$	53.25615(30)	53.3813(7)	125.2(10)	7.5(258)	105
Pb $K_{\alpha 1}$	74.97011(17)	75.0807(5)	110.6(7)	-2.7(404)	99
^{57}Co γ	122.06065(12)	122.0602(2)	-0.4(3)	-0.3(813)	67
^{57}Co γ	136.47356(29)	136.4126(6)	-61.0(9)	2.0(963)	74

For the active pixel, the fit function parameters were

$$\text{linear coefficient} = 121.3671762112429\ (\pm 0.004800965162718212)\ \frac{\text{keV}}{\text{V}}$$
$$\text{quadratic coefficient} = 0.6918126712089158\ (\pm 0.0048177728553711816)\ \left(\frac{\text{keV}}{\text{V}}\right)^2,$$

where the 1σ errors are given, respectively.

Above 136.47 keV the calibration effectively becomes an extrapolation, as depicted in 5.10. The fit corrections at 300 keV are $\Delta E_{300\,\text{keV}}^{^{99}\text{Tc}/^{57}\text{Co}} = -2.47(12)\,\text{keV}$ and $\Delta E_{300\,\text{keV}}^{^{57}\text{Co}} = -1.72(35)\,\text{keV}$ which correspond to -0.8% and -0.6%, respectively. Thus, the projected non-linearity is indeed very small even over such a large energy interval and in-line with what has been reported in previous works [Bat16, Kem18, Gei20].

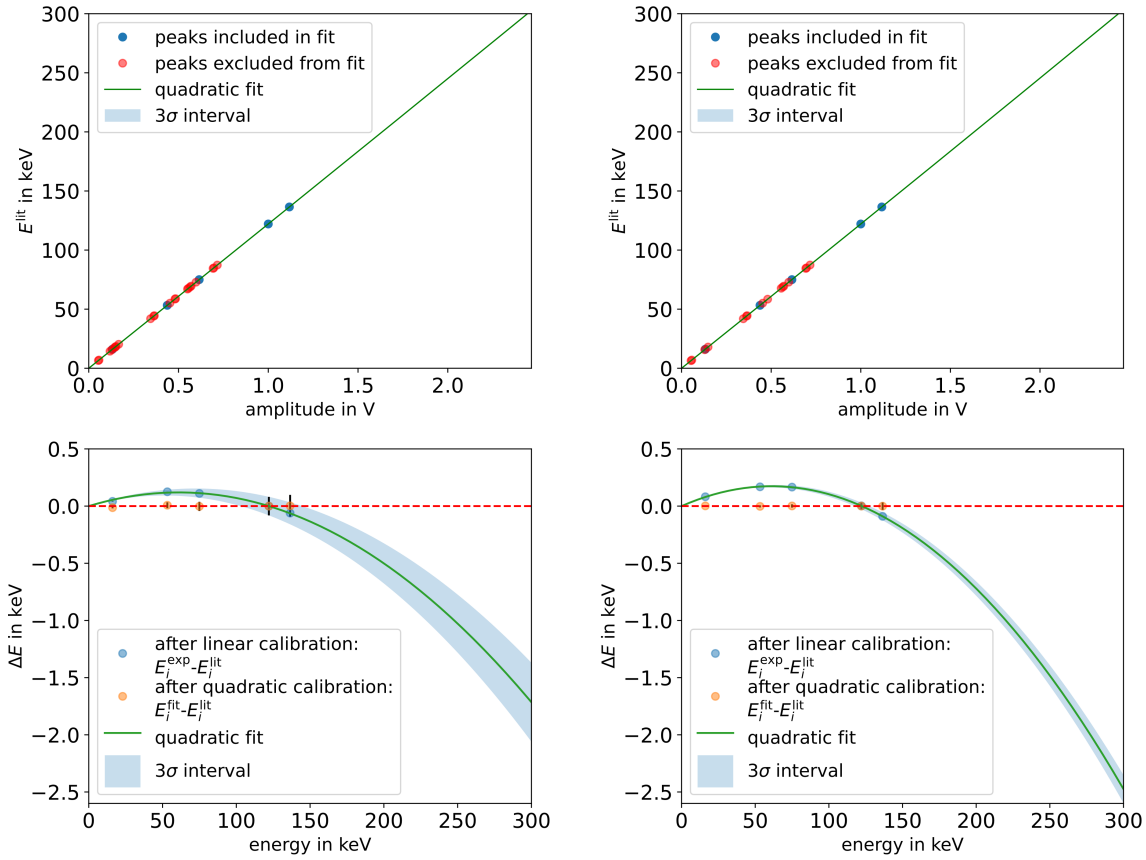

Figure 5.10: Quadratic energy calibration of the non-active ^{57}Co **(left)** and active pixel ^{99}Tc/^{57}Co **(right)**.

Now, a simple way to attain the ^{99}Tc beta spectrum is to remove the calibration background by simply subtracting the scaled ^{57}Co spectrum of the non-active pixel from the ^{99}Tc/^{57}Co spectrum of the active pixel. For a binning of 1 keV this was achieved by using a scaling factor of 0.725555 for the background spectrum in order to eliminate the calibration peaks, see figure 5.11. The scaling factor implies that approximately 27% less calibration peaks were detected by the non-active pixel, probably due to different absorber sizes and relative positioning to the collimator of the calibration source. Small losses may also have been caused by slightly increased amounts of rejected pile-up since the non-active pixels had a larger decay time.

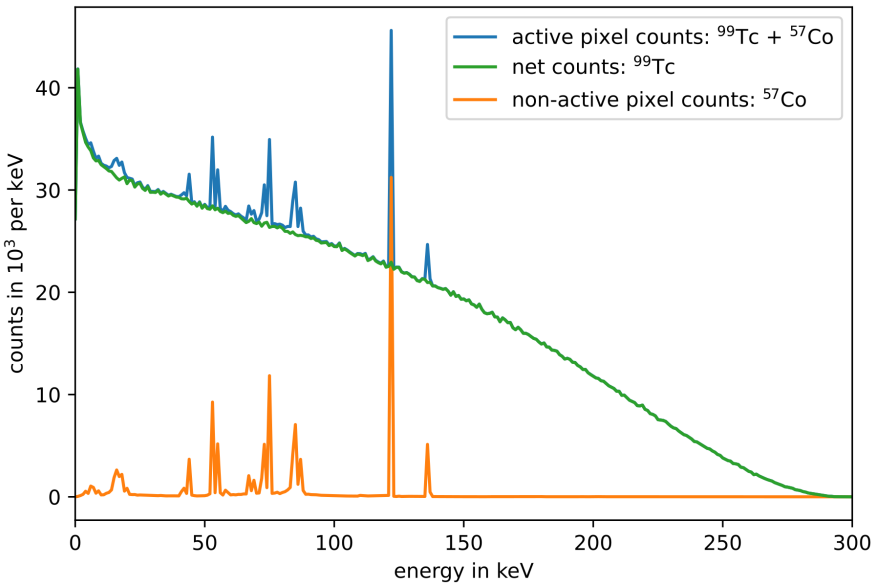

Figure 5.11: Simple background cleaned ^{99}Tc MMC beta spectrum. The net spectrum corresponds to (active pixel counts) - 0.725555·(non-active pixel counts). Thus the number of net counts is approximately $5.23 \cdot 10^6$.

5.1.5 Comparison with previous measurements and theory

In [Loi19, Loi20] a beta spectrum of ^{99}Tc measured with MMCs and calibrated with ^{133}Ba was firstly presented. It featured two orders of magnitude lower energy thresholds (0.65 keV) and a greatly improved energy resolution (0.1 keV up to 383 keV) compared to measurements found in the literature, see table 2.4 and figure 2.10. The experiment was performed at the LNHB[3] and although MMCs where used in both setups, the experiments have several differences which increases their independence and improves the comparative validation. The ^{99}Tc sources were prepared using electrodeposition and automated drop dispensing at the LNHB and PTB, respectively. This is an important issue as drop-deposited sources have been known to cause spectral effects due to sample crystal interaction, in contrast to electrodeposited sources [Hoo15, Loi18]. The MMC detectors had non-identical designs and were mounted in detector modules using different cryogenic setups in comparable electromagnetic lab environments. Data were recorded by individual data acquisition systems, and the analysis was done independently using separate trigger methods and codes, as indicated in table 5.5 below.

[3]LNHB = Laboratoire National Henri Becquerel, the French National Metrology Laboratory for ionizing radiation

Table 5.5: Experimental MMC setups at the LNHB vs. at the PTB.

Institute	**LNHB**	**PTB**
Sample preparation	electrodeposition: metallic Tc	(micro) drop deposition: crystalline Tc_2O_7
Absorber preparation	single quadratic size M	array octagonal: size M
MMC design	MetroBeta V1	MetroBeta V2
Readout SQUIDs	Supracon VC1A	PTB X1
Calibration source	^{133}Ba	^{57}Co
Cryogenic cooling	^{3}He/^{4}He dilution insert in ^{4}He bath	dry ^{3}He/^{4}He cryostat
Detector module	planar	cylindrical
Trigger mode	rising flank	constant fraction discriminator
Evaluation code	MATLAB	Python

The measured and non-linear corrected ^{99}Tc/^{57}Co spectrum is depicted in figure 5.12 where it is compared to the independently measured ^{99}Tc/^{133}Ba spectrum using an MMC beta spectrometer. The spectra show excellent agreement over the entire energy interval, even though the respective calibration backgrounds are still included.

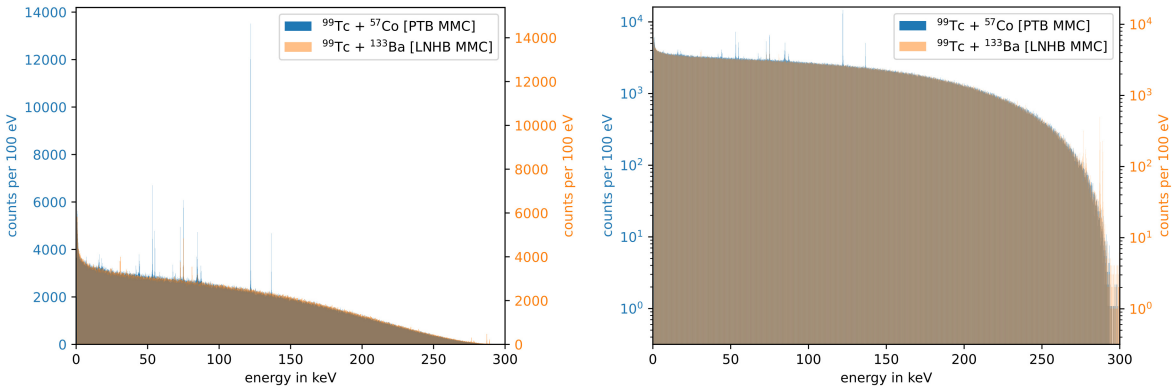

Figure 5.12: Comparison of ^{99}Tc beta spectra with ^{57}Co and ^{133}Ba calibration peaks that were independently measured with MMCs at the PTB and LNHB, respectively, in linear **(left)** and logarithmic scale **(right)**. The spectra were normalized for counts between 150 keV and 250 keV, where no calibration peaks are found to enable a comparison of the beta spectra shapes. While the external ^{133}Ba source offers calibration lines over a wide energy range (at 4.7, 30.6, 31.0, 35.1, 81.0, 302.9, 356.0, 383.8 keV) there are none in the middle-region where there are two ^{57}Co γ lines at 122.06 and 136.47 keV. Interestingly, the spectra share common secondary effect peaks e.g. Pb $K_{\alpha 1}$ at 74.97 keV.

In the LNHB MMC experiment, a simultaneous reference measurement of the calibra-

tion source using a non-active pixel was not done. A ^{99}Tc spectrum was extracted by manually removing the identified photon peaks caused by the ^{133}Ba. For the measured spectrum of this thesis, it is possible to subtract the measured ^{57}Co calibration background from the ^{99}Tc/^{57}Co as a first approximation, at least at an energy resolution of 1 keV as shown in figure 5.11. Furthermore, at energies (> 25 keV) the MMC measurements are further confirmed by a recent measurement using a novel semiconductor PIPS[4] detector setup, see [Sin19, Sin20]. The solid angle of the detector is 98.7% of a full 4π geometry and the spectrum is presented in unfolded form using the algorithm described in [Pau20, Sin20] and section 5.2 below. An advantage of such semiconductor spectrometers is their ability to collect large statistics: the sample activity can be up to 1 kBq and there are approximately $241 \cdot 10^6$ counts in the spectrum. A comparative plot is depicted in figure 5.13.

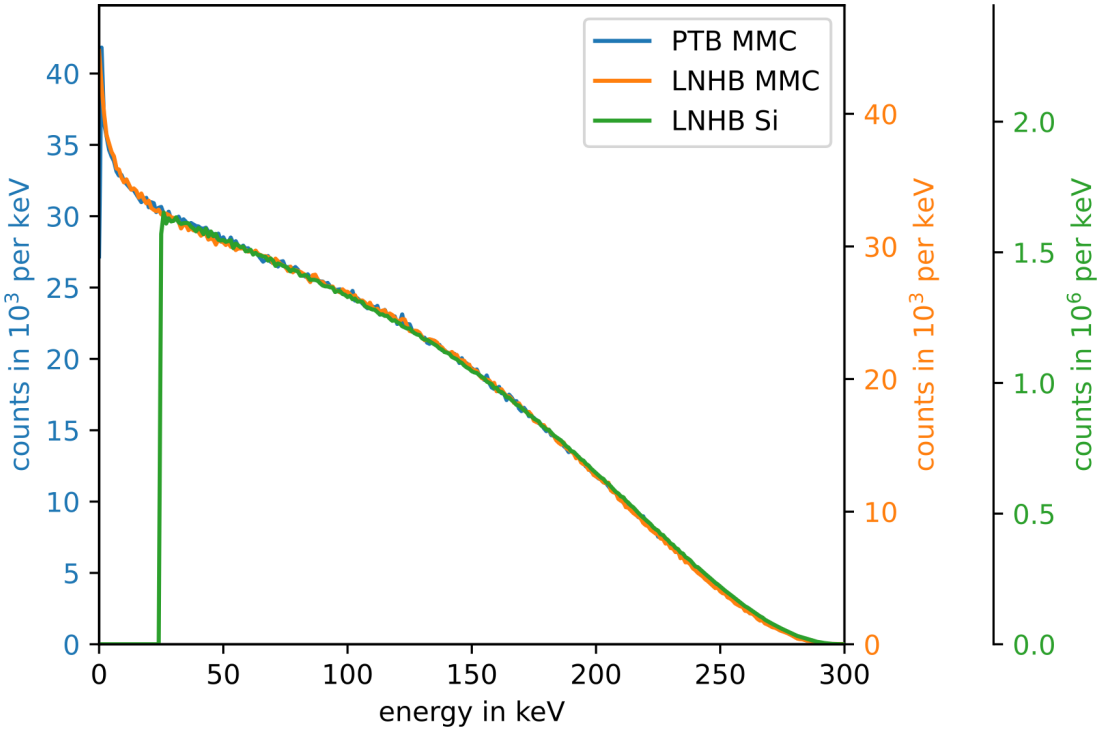

Figure 5.13: Comparison of recent ^{99}Tc measurements, which were normalized for counts between 25 keV and $E_{\max}$.

The MMC spectra were transformed to normalized beta spectra (2.19) by dividing with the respective total number of counts. Notably, the comparison with state-of-the-art theoretically calculated spectrum shapes shows significant deviations, even when using the screening and atomic exchange effects of the calculation methods presented in section 2.3. While the agreement between the experimental spectra is excellent, the calculations underestimate the counts at energies below 20 keV, where there have been no other published measurements to date, see figure 5.14.

[4]PIPS = Passivated Implanted Planar Silicon

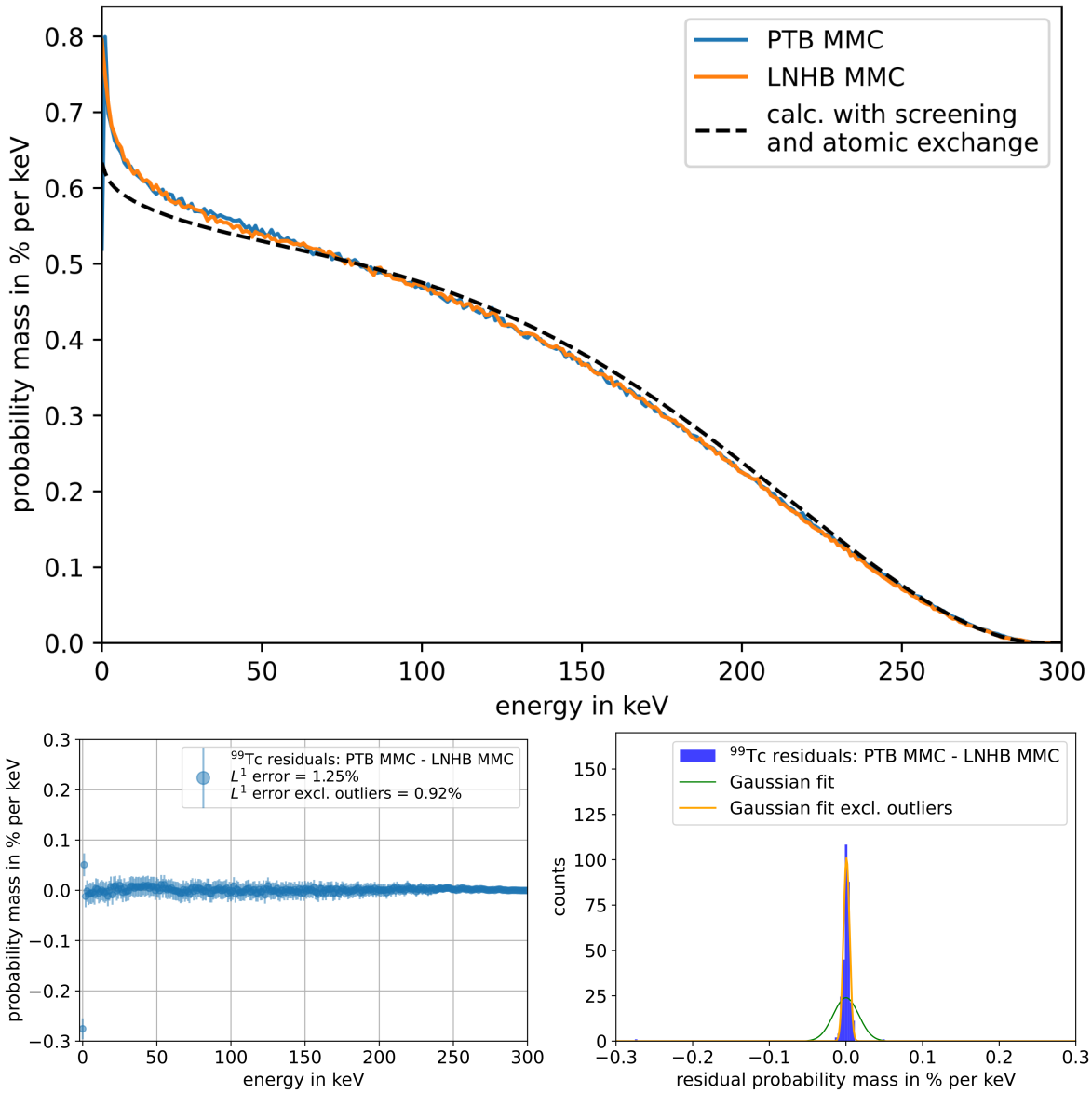

Figure 5.14: Comparison of ^{99}Tc beta spectra measured with MMCs and preliminary state-of-the-art theoretical beta spectrum provided by X. Mougeot **(top)**. A residual plot **(bottom left)** that shows statistical Poisson errors and where the L^1 error is the sum of the absolute residuals. Gaussian plots **(bottom right)** indicate that the residual distribution is mainly statistical in nature as the MMC spectra show excellent agreement, except below 1 keV where there is a significant deviation. This is probably due to slightly differing energy thresholds of 0.65 keV (LNHB) and 0.75 keV (PTB) in the measurements.

As the experiments were conducted independently and MMCs have shown to be very reliable in measuring beta emitters, the result calls for developing new theoretical methods for calculating the spectra of second forbidden non-unique beta transitions such as in the case of ^{99}Tc. This will be addressed in a future work.

Liquid scintillation validation

The activity of a ^{99}Tc solution was determined in [Kos19] with the LSC methods TDCR and CNET. In figure 5.15, the activity is plotted over the efficiency for five 10 ml samples that were measured with TDCR (in an M27 setup) and CNET (in a Tricarb 2800 TR setup *and* in a Wallac CNET counter). Since the commercial CNET setups show some variation, their combined average values are shown. A Birks constant value of kB=0.0075 cm/MeV was used. Two different beta spectra were used as input for the efficiency calculation: the LNHB MMC and the currently recommended Reich and Schüpferling [Rei74, Beh76] spectrum with a maximum beta energy of 293.8 keV [Be11]. Apparently, the CNET results converge much better to the TDCR measurement when the MMC beta spectrum is used as an input.

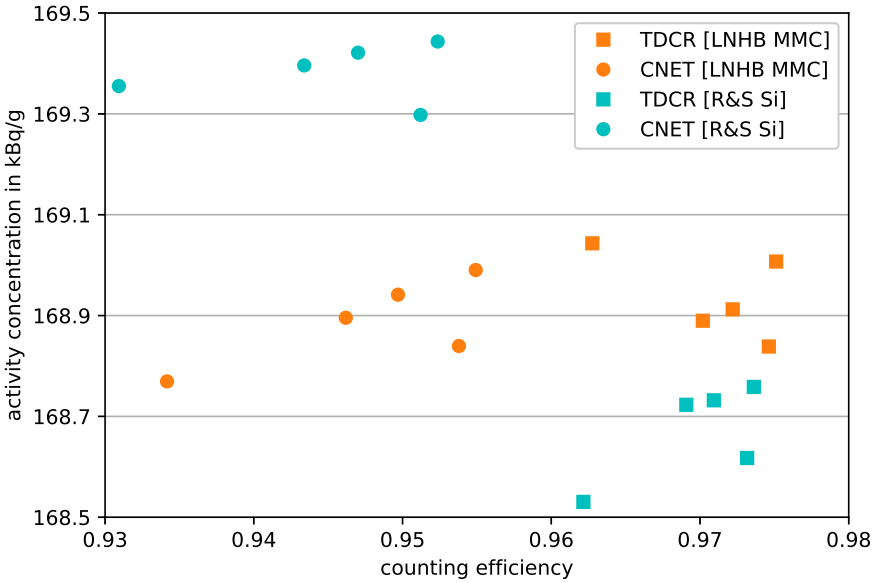

Figure 5.15: Activity concentration of a ^{99}Tc solution as a function of the counting efficiency when using a kB parameter of 0.0075 cm/MeV [Kos19].

In fact, the relative activity deviation between the CNET and TDCR methods was reduced by approximately 78% (from 14‰to -3‰) when the MMC spectrum was used as input for the efficiency calculations.

Table 5.6: Comparison of MMC ^{99}Tc measurements with the recommended measured beta spectrum in the literature [Beh76, Kos19].

Measurement	**Counts**	**Energy resolution FWHM**	**Energy range in keV**
LNHB [Loi19, Loi20]	$5.6 \cdot 10^6$	100 eV up to 384 keV	0.65 - $E_{\max}$
PTB [this work]	$5.3 \cdot 10^6$	73 eV at 136.4 keV	0.75 - $E_{\max}$
Reich and Schüpferling [Rei74]	$\sim 10^6$	7 keV at 624.25 keV	55-255

5.2 An unfolding algorithm for calorimetric beta spectrometry

When aiming at a high energy resolution it is important to keep the combined sensor and absorber heat capacity as low as possible, see chapters 3-4. Hence, the absorber dimensions are often designed to be rather small but large enough to ensure that all beta electrons are completely stopped within the absorber. Considering a high-Z material for the absorber (e.g. gold, with $Z = 79$) and beta emitters with end-point energies of a few hundred keV or more, fractions of the initial energies of emitted beta particles may not be detected due to bremsstrahlung escaping from the absorber. In this case, the measured beta spectrum features distortions and needs to be corrected.

Figure 5.16a illustrates simulated decay events of beta electrons starting in the center of a 4π absorber. In all cases, the electrons are stopped well before reaching the border of the absorber whereas bremsstrahlung photons often escape. This causes some electrons with high initial energies to be detected with a reduced energy. From such a simulation it is rather straightforward to predict the measured spectrum provided that the true beta spectrum and the absorber geometry are known. Figure 5.16b also shows that the measured spectrum underestimates the probabilities for electron emission with high energies whereas low-energy emissions are overestimated. This leads to a systematic skew in the measured spectrum.

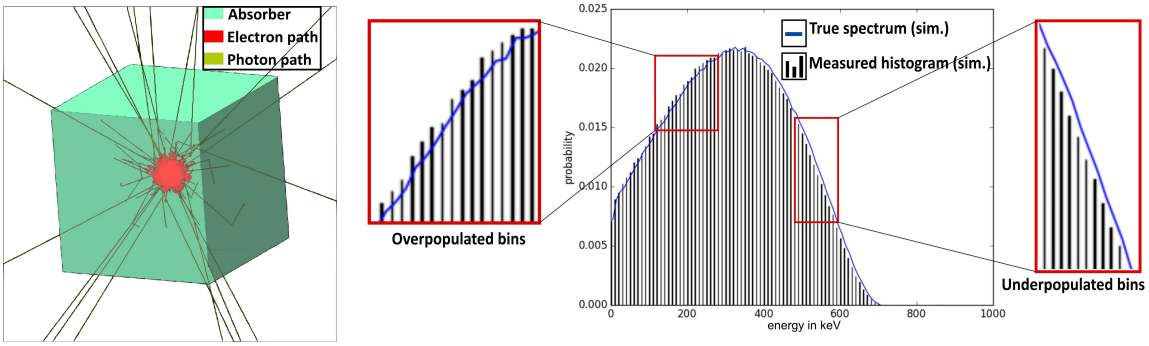

(a) 1000 particle tracks (b) True and measured spectra

Figure 5.16: Simulation results for a ^{36}Cl point source embedded in a 4π Au absorber with dimensions $0.6 \times 0.6 \times 0.6\,\mathrm{mm}^3$. The total energy loss is approximately 0.8% i.e. the absorber quantum efficiency is 99.2%.

To retrieve the true beta spectrum from the measured spectrum requires unfolding (or deconvolution) procedures [Kno10, Cow98]. In this chapter, we use a divide and conquer approach and propose to divide the problem of unfolding such measured data (which is typically in the form of a histogram i.e. a discretized spectrum) from high resolution microcalorimeters into two successive parts:

(i) Reducing the noise, pile-up and background of the raw pulse data e.g. via optimal filtering which is a standard procedure when using MMCs [Szy93, McC05, Arm12]

or using other methods such as a resolution correction [Wor64]. The resulting pulse height distribution is referred to as the measured histogram in this chapter.

(ii) Applying a matrix inversion unfolding algorithm to correct for systematic energy losses within well-defined absorbers. This amounts to estimating a response matrix for the physical properties of the absorber using Monte Carlo simulations. The unfolded histogram is then retrieved from the measured histogram using the calculated absorber response matrix.

The main contribution of this chapter is describing the regularity, implementation and performance of the matrix inversion method of part (ii). While extensive Monte Carlo simulations are needed, the procedure is highly practical and applicable to various absorber geometries as calculated examples indicate. Similar, somewhat simpler matrix inversion methods have been used in several works e.g. for unfolding gamma spectra [Sta56, Lov89, Rah10]. However, to the best of our knowledge, a matrix inversion approach of this kind has not been applied to unfold high resolution beta spectra, thus far. An advantage of the proposed unfolding method is that the true spectrum shape is not needed as an input. The presented method will be required in the analysis of experimentally determined beta spectra of ^{36}Cl ($E_{\max} = 709.5\,\mathrm{keV}$) and other radionuclides which were measured within the scope of the EMPIR MetroBeta project [Loi18].

The general and statistical unfolding problems are formulated in section 5.2.1 along with mathematical definitions. Section 5.2.2, where the unfolding algorithm is presented in detail, constitutes the main part of the section. The consistency of the method is demonstrated in section 5.2.3 using simulated data. In section 5.2.4, the accuracy of the algorithm is tested by correcting external bremsstrahlung effects for independently simulated measurement data. The mathematical proofs are found in appendix A.4.

5.2.1 The unfolding problem

Consider n decays of a pure beta emitter in a time frame $t \in [0, T]$,$T > 0$. Let E_i denote the kinetic energy of the i:th emitted beta particle for $i = 1, \ldots, n$. Assume that the E_i are independent and identically distributed random variables $E_i \in [0, E_{\max}]$, where $E_{\max} > 0$ is the maximum energy of the beta particle. Furthermore, it is assumed that the E_i are absolutely continuous, such that the probability density function of E_i exists and is given by its theoretical (normalized) beta spectrum function f, as depicted in figure 5.17. The function $f : [0, E_{\max}] \to \mathbb{R}_{\geq 0}$ has the following properties by assumption:

- f is smooth i.e. at least three times continuously differentiable and
- $\int_0^{E_{\max}} f(E)\,\mathrm{d}E = 1$ [normalization condition].

Measuring the beta spectrum function f directly and completely is not possible as any experimental setup or detector has an inherent response function due to the interaction of the radionuclide source with the material of the setup. A measured beta spectrum

function f^{meas} can be represented [Kno10] as the convolution of a detector response function r and the true incident (theoretical) energy spectrum f:

$$f^{\text{meas}}(E) = \int_0^{E_{\max}} r\left(\acute{E}, E\right) f(\acute{E})\,\mathrm{d}\acute{E}, \quad \text{[general unfolding problem]}$$

where $f^{\text{meas}}(E)\,\mathrm{d}E$ corresponds to the probability that a decay within $\mathrm{d}E$ about E is measured in the detector and $r\left(\acute{E}, E\right) : [0, E_{\max}] \times \mathbb{R}_{\geq 0} \to \mathbb{R}$ denotes the response function of the detector. While the equation is well-defined under appropriate regularity conditions, it is reasonable to regard it as an idealized, limiting relation since

1. A beta radionuclide measurement provides finitely many data points of the spectrum i.e. one observes n decays of the radionuclide over a finite time frame.

2. The measured beta spectrum is typically represented as a histogram i.e. a step function over a finite number of energy bins, where the number of measurements in a particular energy bin corresponds to the height of the histogram.

Thus, step functions and histograms are relevant when measurements and statistical simulations are considered [Reg02]. Furthermore, the issue of finding the true beta spectrum f can be interpreted as an inverse problem [Mat03, Kai06]. However, before we can formulate the statistical discrete problem that we wish to solve in a precise manner, further definitions are needed.

Measurements: a discrete set of random variables

During a measurement, one observes/measures a somewhat distorted energy $E_i^{\text{meas}} = E_i + B_i + N_i$ where $B_i \in [-E_{\max}, 0]$ and $N_i \in \mathbb{R}$ denote the energy escape terms (e.g. due to bremsstrahlung, deflection, etc.) and noise components, respectively. The normalized measured energy spectrum generated by n decays can be represented as a histogram i.e. a step function over a finite number N of energy bins of length $\Delta E_N := \frac{E_{\max}}{N} > 0$. More precisely, if we define the empirical distribution function of E_i^{meas} for n decays as

$$F_n^{\text{meas}}(E) := \frac{\#E_i^{\text{meas}} : E_i^{\text{meas}} \leq E}{n}, \tag{5.3}$$

the measured energy spectrum over N energy bins (empirical density function of E_i^{meas} [Wat78]) is defined as

$$f_{N,n}^{\text{meas}}(E) := \frac{F_n^{\text{meas}}(E + \Delta E_N) - F_n^{\text{meas}}(E)}{\Delta E_N} \tag{5.4}$$

$$= \sum_{j=1}^{N} h_{N,n,j}^{\text{meas}} \cdot \mathbb{1}_{((j-1)\cdot\Delta E_N, j\cdot\Delta E_N]}(E), \tag{5.5}$$

where

$$h_{N,n,j}^{\text{meas}} = \frac{\#E_i^{\text{meas}} : E_i^{\text{meas}} \in ((j-1)\cdot\Delta E_N, j\cdot\Delta E_N]}{n\cdot\Delta E_N} \tag{5.6}$$

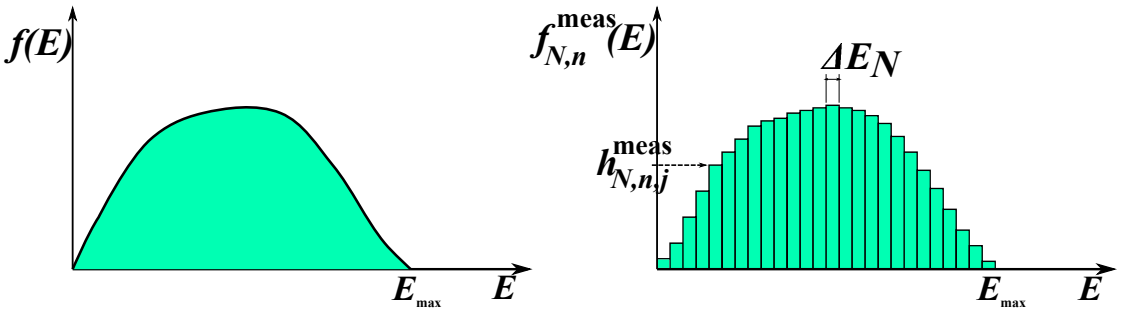

Figure 5.17: Probability density function/theoretical beta spectrum function f **(left)** compared to an empirical density function i.e. a histogram/measured energy spectrum over N energy bins after n decays **(right)**. In the example, the number of energy bins is $N = 26$ and the histogram height for the energy bin with index $j = 5$ is indicated. The area under the respective curve sums to 1.

are the histogram heights of the j:th energy bin, see figure 5.17. It follows that

$$\int_0^{E_{\max}} f_{N,n}^{\text{meas}}(E)\,\mathrm{d}E = \int_0^{E_{\max}} \sum_{j=1}^{N} h_{N,n,j}^{\text{meas}} \cdot \mathbb{1}_{((j-1)\cdot\Delta E_N,\, j\cdot\Delta E_N]}(E)\,\mathrm{d}E \tag{5.7}$$

$$= \sum_{j=1}^{N} h_{N,n,j}^{\text{meas}} \cdot \Delta E_N = \frac{n}{n\cdot\Delta E_N}\cdot\Delta E_N = 1. \tag{5.8}$$

For a sufficiently small noise and if the probability density function of B_i exists and is smooth, it follows (see e.g. [p.129, Wat78]) that

$$\lim_{n\to\infty} f_{N,n}^{\text{meas}}(E) = \frac{F^{\text{meas}}(E+\Delta E_N) - F^{\text{meas}}(E)}{\Delta E_N} \quad \text{with probability 1} \tag{5.9}$$

and since F^{meas} is differentiable, it holds that

$$\lim_{N\to\infty}\lim_{n\to\infty} f_{N,n}^{\text{meas}}(E) = \lim_{N\to\infty} \frac{F^{\text{meas}}(E+\Delta E_N) - F^{\text{meas}}(E)}{\Delta E_N} = f^{\text{meas}}(E), \tag{5.10}$$

where F^{meas} and f^{meas} denote the measured empirical distribution and spectrum functions of $E_i^{\text{meas}} = E_i + B_i + N_i$, respectively, i.e. of the energy measured by the detector. Thus, even when precise and noise-free measurements are made, the energy escape will still be relevant.

In order to statistically compare the true (without detector response) and measured spectrum, one can define empirical distribution and density functions for the true spec-

trum f after n decays and over N energy bins of width ΔE_N:

$$f_{N,n}(E) := \frac{F_n(E + \Delta E_N) - F_n(E)}{\Delta E_N} \tag{5.11}$$

$$= \sum_{j=1}^{N} h_{N,n,j} \cdot \mathbb{1}_{((j-1)\cdot\Delta E_{N,j}\cdot\Delta E_N]}(E), \tag{5.12}$$

where

$$h_{N,n,j} = \frac{\#E_i E_i \in ((j-1)\cdot\Delta E_N, j\cdot\Delta E_N]}{n\cdot\Delta E_N} \tag{5.13}$$

denotes the histogram heights of the j:th energy bin. Thus, the spectrum step functions $f_{N,n}$ and $f_{N,n}^{\text{meas}}$ can be completely reconstructed using their respective histogram heights and the unfolding problem can be reformulated in terms of the histogram heights instead.

Let $\boldsymbol{h}_{N,n} := (h_{N,n,1}, \ldots, h_{N,n,N})^T$ denote the vector of all true histogram heights for n beta decays over N energy bins and $\boldsymbol{h}_{N,n}^{\text{meas}} := \left(h_{N,n,1}^{\text{meas}}, \ldots, h_{N,n,N}^{\text{meas}}\right)^T$ denote the corresponding vector for the measured histogram. It is obvious that these objects are $N\times 1$ random vectors in which each component can take a value in $\left\{0, \frac{1}{n\Delta E_N}, \frac{2}{n\Delta E_N}, \ldots, \frac{n}{n\Delta E_N}\right\}$. They correspond to discrete samples of the corresponding continuous true and measured spectra, respectively [Wat78]. The statistical discrete unfolding problem is defined as

$$\boldsymbol{h}_{N,n}^{\text{meas}} = \boldsymbol{R}_N \boldsymbol{h}_{N,n} \qquad \text{[statistical discrete unfolding problem]} \tag{5.14}$$

where $\boldsymbol{R}_N$ denotes the discrete response (forward) operator given by the $N \times N$ matrix

$$\boldsymbol{R}_N := \begin{pmatrix} R_{11} & \cdots & R_{1N} \\ \vdots & \ddots & \vdots \\ R_{N1} & \cdots & R_{NN} \end{pmatrix} \qquad \text{[response matrix of the absorber]} \tag{5.15}$$

and R_{ij} denotes the response coefficient coupling the ith energy bin of the measured histogram with the jth energy bin of the true histogram [Kno10]. To solve the discrete unfolding problem, one needs to estimate the forward response matrix $\boldsymbol{R}_N$ and then calculate the true histogram $\boldsymbol{h}_{N,n}$. A direct inspection indicates that the system is heavily underdetermined as there are $N^2 + N$ unknowns and only N equations. It may be considered as an inverse problem [Kai06]. As will be shown below, the system of equations simplifies considerably using the proposed Monte Carlo simulation approach such that the response matrix can be estimated, and from this, the true histogram may be calculated.

5.2.2 The unfolding algorithm

The proposed unfolding algorithm is based on the following assumptions:

A1): The extensive utilization of Monte Carlo simulations is a sufficiently accurate

method to simulate particle and radiation transport in matter [Ago03, Sem03, Kaw18].

A2): The detector dynamics are assumed to be slower than the particle material dynamics: if there are several energy depositions for a single decay, the sum of these are detected as a single energy deposition. This is a typical property of microcalorimetric detectors.

A3): It is assumed that for at least one of the simulated decay events in every single-energy bin, the entire decay energy is deposited in the absorber.

A4): The measured decays are assumed to be independent of each other i.e. the detector and the radionuclide source have no memory and pile-up issues are not considered.

Single-energy bin Monte Carlo simulations

A key challenge in the statistical discrete unfolding problem consists in handling the underdetermined system of equations described above. To resolve this issue, N single-energy bin pulse height distributions are simulated for the given absorber geometry. The bin energies cover the entire range of the measured spectrum. This may seem as an overly laborious method, however, a multi-energy bin simulation and correction approach will in general lead to an underdetermined system of linear equations, see proposition A.4.3.

The single-energy bin approach will allow us to consistently estimate the forward response matrix, column by column, and thus solve the unfolding problem, statistically. The (forward) input in the algorithm are $m \sim 10^5$ simulated (pseudo)-random variables i.e. beta particle energies, uniformly distributed over the jth energy bin of length ΔE_N. Thus, the response of a single energy bin is simulated at a time and the corresponding histogram is very simple, as depicted in figure 5.18. The corresponding histogram heights are given by

$$\boldsymbol{h}_{N,m}^{\text{sim\_input},j} = \left(0, \ldots, 0, h_{N,m,j}^{\text{sim\_input},j}, 0, \ldots, 0\right)^T, \quad \text{where} \quad h_{N,m,j}^{\text{sim\_input},j} = \frac{1}{\Delta E_N}. \tag{5.16}$$

The m simulated beta particles interact with the absorber material and, depending on their energy, cause bremsstrahlung, scattering or other radiation that may escape from the absorber. The total energy deposited by each of the m simulated decays in the absorber via primary and secondary particles is recorded in the simulation. The simulation output for each input bin vector j is given by the corresponding normalized simulated output histogram heights, i.e. an $N \times 1$ vector:

$$\boldsymbol{h}_{N,m}^{\text{sim\_output},j} = \left(h_{N,m,1}^{\text{sim\_output},j}, \ldots, h_{N,m,N}^{\text{sim\_output},j}\right)^T. \tag{5.17}$$

It is noted that in 4π absorbers, for small j (small input energy) the vector above has all components equal to zero, except for the jth component. This is because

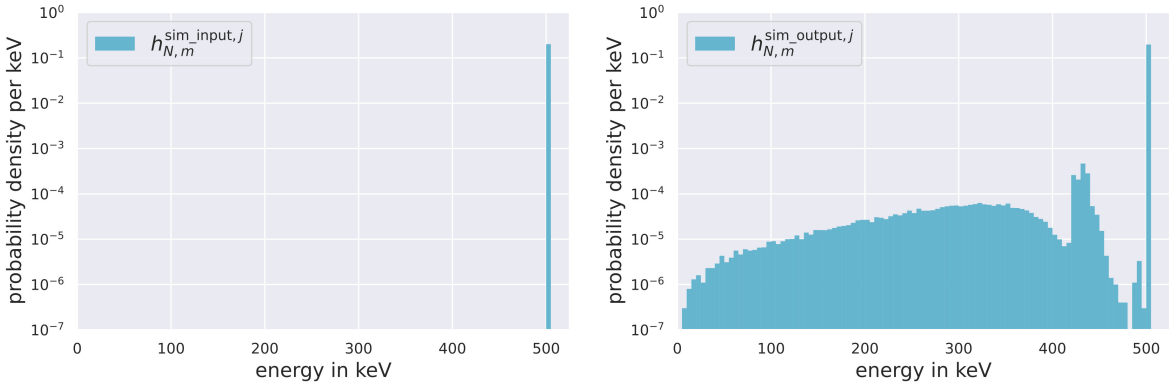

Figure 5.18: Illustration of $h^{\text{sim\_input},j}_{N,m}$ **(left)**, the probability mass is confined to the jth energy bin. This is generally not the case for $h^{\text{sim\_output},j}_{N,m}$ **(right)**, where an isotropic point source of monoenergetic electrons having an energy of 500 keV, embedded at the center of a Au cube of side length 0.6 mm (4π absorber) was simulated for $m = 10^6$ particles. Furthermore, one has $N = 142$, $j = 100$ and $\Delta E_N = 5\,\text{keV}$. Apparently, the energy losses are caused by fluorescence and escape peaks in the Au absorber along with continuous bremsstrahlung.

bremsstrahlung is very improbable at low energies. However, for large j (high input energy), bremsstrahlung generation and hence, energy escape, is quite likely and the components will be non-zero for some components with indices less than or equal to j. In general, probability mass will only "migrate to the left", by conservation of energy. Thus, given that the simulated input particles have energies exclusively in the jth energy bin, the only migration that may occur is to a lower or within the identically indexed bin, see figure 5.18.

Calculating the single-energy bin forward matrix operators

Next, the single-energy bin forward unfolding problem is considered:

$$\boldsymbol{S}^j_{N,m}\boldsymbol{h}^{\text{sim\_input},j}_N = \boldsymbol{h}^{\text{sim\_output},j}_N, \tag{5.18}$$

where the single-energy bin forward matrix $S^j_{N,m}$ is defined for each j as

$$\boldsymbol{S}^j_{N,m} := \begin{pmatrix} 0 & \cdots & 0 & S^{j,1\leftarrow j}_{N,m} & 0 & \cdots & 0 \\ \vdots & \ddots & \vdots & \vdots & \vdots & \ddots & \vdots \\ 0 & \cdots & 0 & S^{j,N\leftarrow j}_{N,m} & 0 & \cdots & 0 \end{pmatrix}, \qquad \text{[single-energy bin forward matrix]} \tag{5.19}$$

and $S^{j,k\leftarrow j}_{N,m} \in [0,1]$ denotes the transformation coefficients for the probability mass migration from energy bin j to energy bin k for m samples in the simulations. The properties of $S^{j,k\leftarrow j}_{N,m} \in [0,1]$ are derived in lemma A.4.1. Please note that all elements of the single-energy bin forward matrix are zero except for in the jth column, as only

the jth histogram energy is operated upon:

$$\begin{pmatrix} 0 & \cdots & 0 & S_{N,m}^{j,1\leftarrow j} & 0 & \cdots & 0 \\ \vdots & \ddots & \vdots & \vdots & \vdots & \ddots & \vdots \\ 0 & \cdots & 0 & S_{N,m}^{j,N\leftarrow j} & 0 & \cdots & 0 \end{pmatrix} \begin{pmatrix} \mathbf{0} \\ h_{N,m,j}^{\text{sim\_input},j} \\ \mathbf{0} \end{pmatrix} = \begin{pmatrix} h_{N,m,1}^{\text{sim\_output},j} \\ \vdots \\ h_{N,m,N}^{\text{sim\_output},j} \end{pmatrix} \tag{5.20}$$

i.e.

$$\begin{pmatrix} S_{N,m}^{j,1\leftarrow j} \\ \vdots \\ S_{N,m}^{j,N\leftarrow j} \end{pmatrix} h_{N,m,j}^{\text{sim\_input},j} = \begin{pmatrix} h_{N,m,1}^{\text{sim\_output},j} \\ \vdots \\ h_{N,m,N}^{\text{sim\_output},j} \end{pmatrix}, \tag{5.21}$$

where the matrix entries $S_{N,m}^{j,k\leftarrow j}$ are easily solved for since the input and output vectors are known as a priori inputs and as simulation result outputs, respectively.

Calculating the total forward matrix

The corresponding estimate of the total forward matrix is given by the sum of the single-energy bin forward matrices over all energy bins:

$$\boldsymbol{S}_{N,m} = \sum_{j=1}^{N} \boldsymbol{S}_{N,m}^{j} = \begin{pmatrix} S_{N,m}^{j,1\leftarrow 1} & \cdots & S_{N,m}^{j,1\leftarrow N} \\ \vdots & \ddots & \vdots \\ \mathbf{0} & \cdots & S_{N,m}^{j,N\leftarrow N} \end{pmatrix} \quad \text{[total forward matrix]}. \tag{5.22}$$

By construction and conservation of energy (see lemma A.4.1) it follows that the total forward matrix is an $N \times N$-dimensional random variable which is upper triangular.

The matrix operator $\boldsymbol{S}_{N,m}$ provides an estimate of the response matrix i.e. how each energy bin of the true histogram is modified for the given absorber configuration, and we may write (see proposition A.4.2):

$$\boldsymbol{R}_N = \boldsymbol{S}_{N,m} + \boldsymbol{O}_{N\times N}\left(m^{-\frac{1}{2}}\right), \tag{5.23}$$

where $\boldsymbol{O}_{N\times N}\left(m^{-\frac{1}{2}}\right)$ denotes an $N \times N$-dimensional error matrix in which each component converges as $O_{N\times N}\left(m^{-\frac{1}{2}}\right)$, as only statistical errors are considered due to assumption A1) above. Inserting the estimate into the statistical discrete unfolding problem (5.14), it follows that

$$\boldsymbol{h}_{N,m}^{\text{meas}} = \boldsymbol{R}_N \boldsymbol{h}_{N,m} = \left[\boldsymbol{S}_{N,m} + \boldsymbol{O}_{N\times N}\left(m^{-\frac{1}{2}}\right)\right] \boldsymbol{h}_{N,m}. \tag{5.24}$$

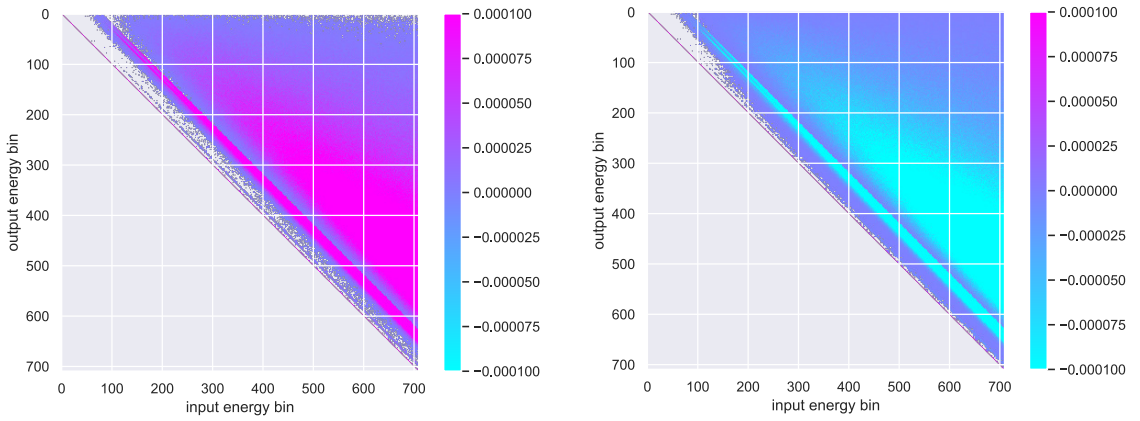

(a) Forward matrix $\boldsymbol{S}_{N,m}$ (b) Backward matrix $(\boldsymbol{S}_{N,m})^{-1}$

Figure 5.19: The forward matrix was generated by simulating within $N = 710$ energy bins of width 1 keV for an isotropic point source embedded in a 4π Au absorber ($0.6 \times 0.6 \times 0.6\,\mathrm{mm}^3$) and in each energy bin, $m = 10^6$ particles were simulated. Column-wise, it contains the energy loss information of figure 5.18. The diagonal elements are close to 1 in both matrices, the off-diagonal elements $x_{\mathrm{forw}} \in (0, 0.0055)$ and $x_{\mathrm{back}} \in (-0.0062, 10^{-6})$. The grey area in the plots corresponds to zero-entries.

Calculating the backward operator and the unfolded histogram

When the algorithm is applied, an estimate $\boldsymbol{h}^{\mathrm{algo}}_{N,n}$ is calculated for the true histogram $\boldsymbol{h}_{N,n}$ by formally inverting the total forward matrix to get

$$\boldsymbol{h}^{\mathrm{algo}}_{N,n} = (\boldsymbol{S}_{N,m})^{-1}\, \boldsymbol{h}^{\mathrm{meas}}_{N,n} \qquad \text{[algorithm estimate of true histogram]} \tag{5.25}$$

where the inverse $(\boldsymbol{S}_{N,m})^{-1}$ exists with probability 1 as shown in proposition A.4.1.

Error of the complete algorithm when used on measurement data

It should be noted that the measured histogram typically contains an $N \times 1$ error vector since it is the result of a noisy measurement combined with a filtering procedure as noted in the introduction:

$$\boldsymbol{h}^{\mathrm{meas}}_{N,n} = \overline{\boldsymbol{h}}_{N,n} + \boldsymbol{O}_N\left(n^{-\frac{1}{2}}\right), \tag{5.26}$$

where $\overline{\boldsymbol{h}}_{N,n}$ denotes an idealized, noise-free measured histogram.

The error component of each bin is assumed to be normally distributed and small compared to the measured bin height such that the propagation of uncertainty, when the matrix inverse (which has small elements as depicted in figure 5.19b) is applied, does not lead to erratic behavior.

The magnitude of the algorithm estimate error is formally given by

$$\left\|\boldsymbol{h}_{N,n} - \boldsymbol{h}^{\text{algo}}_{N,m,n}\right\| = \left\|\boldsymbol{h}_{N,n} - \left[\boldsymbol{S}_{N,m} + \boldsymbol{O}_{N\times N}\left(m^{-\frac{1}{2}}\right)\right]^{-1} \boldsymbol{h}^{\text{meas}}_{N,n}\right\| \tag{5.27}$$

$$= \left\|\boldsymbol{h}_{N,n} - \left[\boldsymbol{S}_{N,m} + \boldsymbol{O}_{N\times N}\left(m^{-\frac{1}{2}}\right)\right]^{-1} \left(\overline{\boldsymbol{h}}_{N,n} + \boldsymbol{O}_{N}\left(n^{-\frac{1}{2}}\right)\right)\right\| \tag{5.28}$$

and depends on the numerical method used to solve for the algorithm estimate via the matrix, the number of measured decays n, the number of samples m used to construct the total forward matrix, the number of bins N and of course on the choice of norm $\|\cdot\|$.

5.2.3 Implementation and consistency results of the algorithm

In this subsection, the algorithm is applied on simulated measured histograms. A practical advantage of using simulated data is that the true histogram is known first hand and thus, the error of the algorithm estimate can be calculated in a straightforward manner. In the following, the implementation procedure is described along with results and a discussion of calculated examples. While the mentioned procedures are software specific, the algorithm could be implemented using many types of Monte Carlo software e.g. GEANT4[5], PENELOPE[6] or EGSnrc[7] [Ago03, Sem03, Kaw18].

Procedure for algorithm implementation

The unfolding algorithm was implemented in Python and the Monte Carlo simulations were carried out using the software EGSnrc [Kaw18]. This consisted of the following steps:

1) Simulation of the true histogram: A ^{36}Cl ($E_{\max} = 709.5\,\text{keV}$) beta spectrum provided by EGSnrc, based on the nuclear decay scheme [Cld19], was used for the true spectrum. From this the true histogram heights were generated by sampling $n \sim 10^6$ energies in a point-like source geometry. The energies, positions and trajectories were saved in the IAEA[8] phase space (phsp) file format [Psd19] using the code EGS Brachy [Tay19].

2) Simulation of the measured histogram: The measured ^{36}Cl histogram heights $\boldsymbol{h}^{\text{meas}}_{N,n}$ were simulated in absorber geometries having typical MMC dimensions, see table 5.7 using the very energies of the true histogram $\boldsymbol{h}_{N,n}$ found in the phsp file.

3) Construction of the total forward matrix: The total forward matrix $\boldsymbol{S}_{N,m}$ was constructed via single-energy bin simulations in the absorber geometry used for

[5]GEANT = GEometry ANd Tracking

[6]PENELOPE = Penetration and ENErgy LOss of Positrons and Electrons

[7]EGS = Electron Gamma Shower, nrc = National Research Council i.e. the largest federal research and development organization in Canada.

[8]IAEA = International Atomic Energy Agency

the measured histogram heights. These simulations covered the energy range from 0 to 710 keV.

4) Calculation of the unfolded histogram heights: The unfolded histogram heights i.e. the algorithm estimate $\boldsymbol{h}^{\text{algo}}_{N,m,n} = (\boldsymbol{S}_{N,m})^{-1}\, \boldsymbol{h}^{\text{meas}}_{N,n}$ were calculated in Python using the forward matrix and the simulated measured histogram heights via the built-in least squares method numpy.linalg.solve [Sci19].

5) Calculation of the algorithm estimate error: In order to calculate the algorithm error, the true histogram heights $\boldsymbol{h}_{N,n}$ were retrieved from the phsp file via simulation of the same point-like source geometry embedded in a large Au block (dimensions: $1 \times 1 \times 1\,\text{m}^3$) to ensure complete energy deposition of primary and secondary particles, in order to exclude any bremsstrahlung effects or information loss in the true histogram.

In step 2), 3) and 5) the pulse height distribution code tutor7pp [Kaw19] was used.

To quantify the consistency and correction capacity of the unfolding algorithm, the residual vectors $\boldsymbol{r}^{\text{meas}}_{N,n} := \boldsymbol{h}_{N,n} - \boldsymbol{h}^{\text{meas}}_{N,n}$ and $\boldsymbol{r}^{\text{algo}}_{N,m,n} := \boldsymbol{h}_{N,n} - \boldsymbol{h}^{\text{algo}}_{N,m,n}$, tracking the bin-wise height differences, were defined. The algorithm error was calculated in the L^1-norm:

$$\left\| \boldsymbol{h}_{N,n} - \boldsymbol{h}^{\text{algo}}_{N,m,n} \right\|_{L^1} = \Delta E_N \sum_{j=1}^{N} \left| h_{N,n,j} - h^{\text{algo}}_{N,m,n,j} \right| \tag{5.29}$$

and analogously for the measured histogram. This corresponds to summing the absolute values of the corresponding residual probability vector elements.

Consistency results

Two different absorber geometries and various measurement relevant values of the algorithm parameters were considered. The steps 1)-5) described in the previous subsection were carried out for 100 random ^{36}Cl histograms, by randomly sampling the initial seeds of the *ranmar* random number generator [Kaw05] in step 1) according to a uniform distribution. An overview of the results is found in table 5.7 along with plots for selected parameter values in figures 5.20-5.22.

Discussion of implementation and consistency results

The implementation shows that the algorithm can be used to unfold measured beta spectra in a consistent manner, especially when 4π absorbers are used. Concerning the rather subtle bremsstrahlung effect, the algorithm gives notable corrections. Table 5.7 indicates that the unfolding algorithm reduces the simulated measured L^1-error by at least 82% at an energy bin width of 1 keV. This is also the case for the 2π absorbers although approximately half of the information/statistics are lost in the measurement process. In practice, a rather precise knowledge of the source geometry is needed for 2π absorbers, as variations of the source distance above the absorber showed. A variation of 10 µm approximately doubled the L^1-error, nonetheless the unfolded histogram

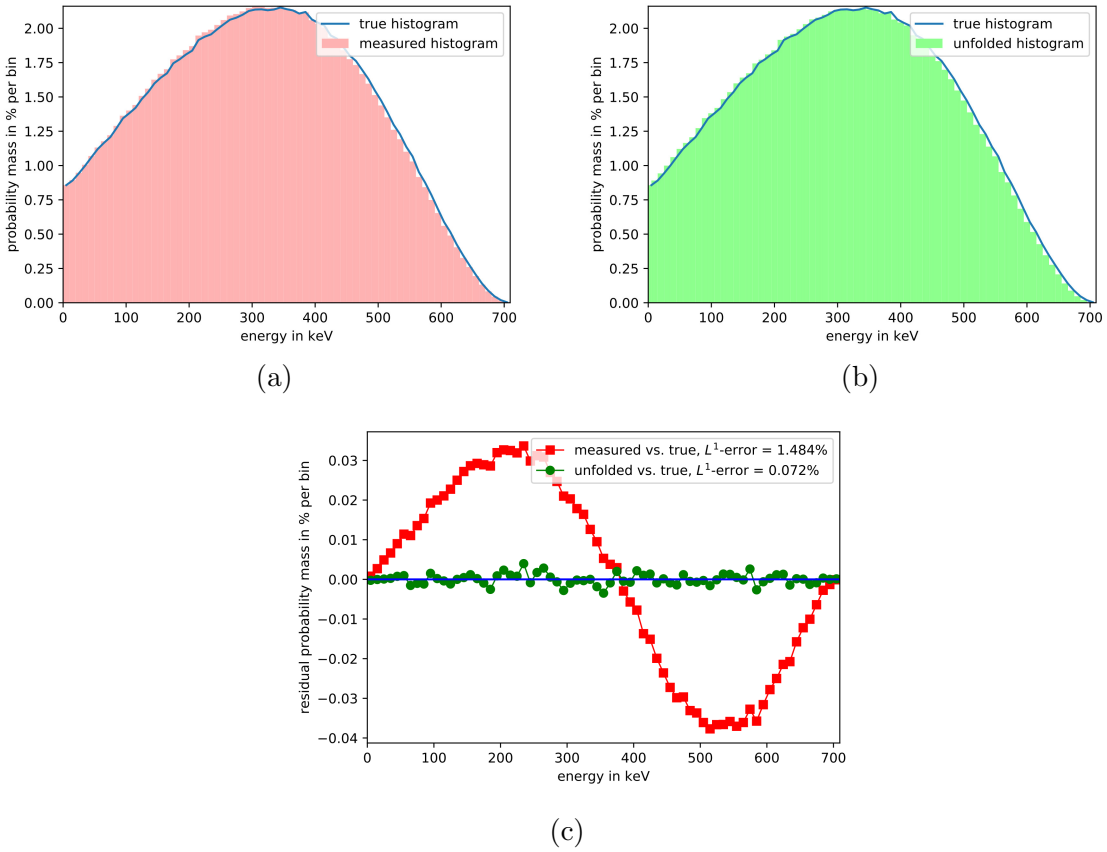

Figure 5.20: Plots of the simulated measured histogram **(top left)** and the unfolded histogram **(top right)** in a 4π absorber along with the true histogram. There are some bremsstrahlung losses at higher energies, which shifts the simulated measured histogram skew slightly to the left. The skew becomes evident in the residual plot **(bottom)** which also shows the correction provided by the unfolding algorithm. Here, the number of events for each single-energy bin simulation was $m = 2.5 \cdot 10^5$ and the number of energy bins is $N = 71$ i.e. the bin width is 10 keV.

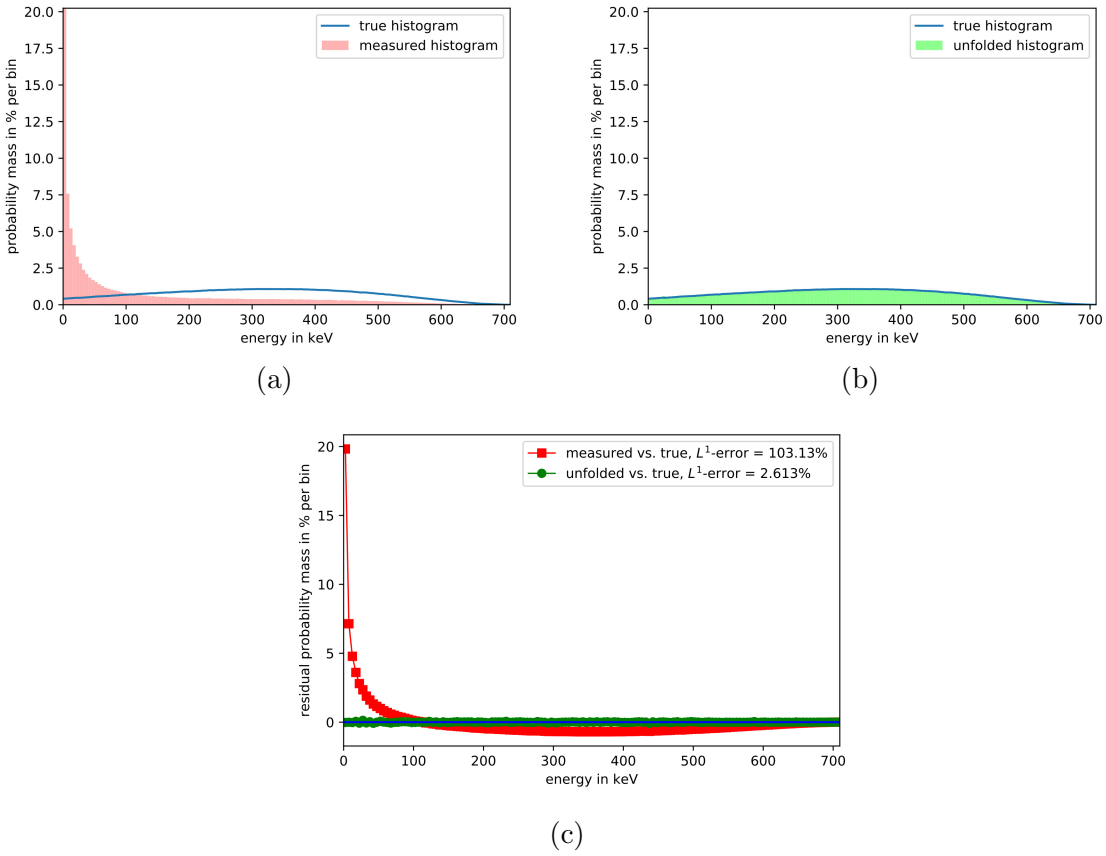

Figure 5.21: The simulated measured spectrum for a 2π absorber geometry **(top left)** and the true spectrum and the algorithm unfolded spectrum **(top right)** are depicted. The residual plot **(bottom)** shows the drastic effect of the unfolding correction. Here, the number of events for each single-energy bin simulation was $m = 5 \cdot 10^5$ and the number of energy bins is $N = 142$ i.e. the bin width is 5 keV.

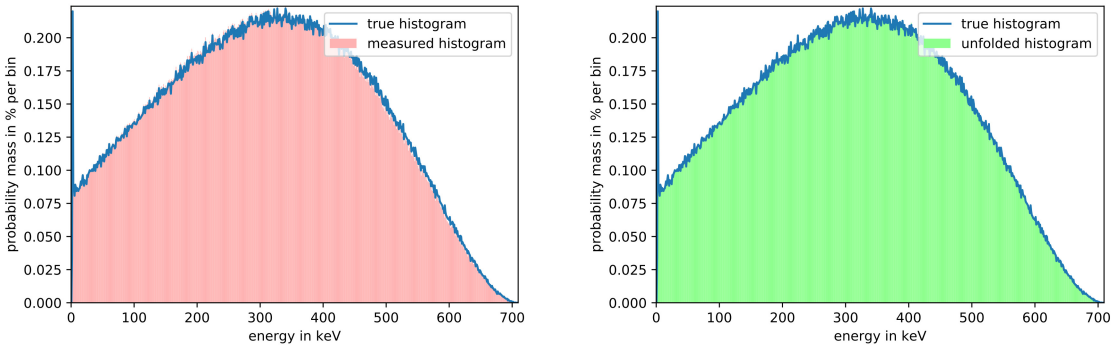

(a)

(b)

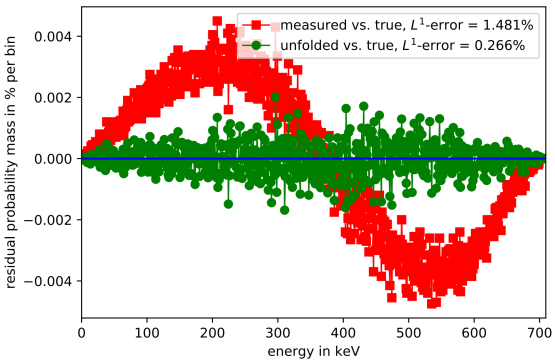

(c)

Figure 5.22: For smaller energy bin width (1 keV, $N = 710$ energy bins), the variance in the simulation becomes more visible. A histogram representation of the simulated measured spectrum **(top left)** and the unfolded spectrum **(top right)** in a 4π absorber is depicted along with the simulated true spectrum. The bremsstrahlung skew is still visible in the residual plot **(bottom)** and the correction provided by the unfolding algorithm is substantial. The number of events for each single-energy bin simulation was $m = 10^6$.

Table 5.7: Overview of simulation results using the proposed unfolding algorithm.

absorber configuration	radionuclide source	true histogram	N bins	m samples per bin	measured L^1-error average [min., max.]	unfolded L^1-error average [min., max.]
4π geometry	^{36}Cl isotropic		71	$2.5 \cdot 10^5$	1.479% [1.449%, 1.508%]	0.085% [0.068%, 0.116%]
				$5 \cdot 10^5$		0.082% [0.064%, 0.112%]
				$1 \cdot 10^6$		0.082% [0.064%, 0.110%]
Au cube 0.6×0.6 $\times 0.6\,\mathrm{mm}^3$	point source at center of cube	100 runs of $2 \cdot 10^6$ samples	142	$2.5 \cdot 10^5$	1.480% [1.450%, 1.508%]	0.118% [0.100%, 0.135%]
				$5 \cdot 10^5$		0.116% [0.097%, 0.135%]
				$1 \cdot 10^6$		0.115% [0.097%, 0.134%]
			710	$2.5 \cdot 10^5$	1.490% [1.461%, 1.516%]	0.256% [0.239%, 0.280%]
				$5 \cdot 10^5$		0.255% [0.238%, 0.278%]
				$1 \cdot 10^6$		0.255% [0.237%, 0.277%]
2π geometry	^{36}Cl isotropic		71	$2.5 \cdot 10^5$	103.22% [102.84%, 103.55%]	2.099% [1.463%, 2.965%]
				$5 \cdot 10^5$		2.069% [1.553%, 2.978%]
				$1 \cdot 10^6$		2.036% [1.531%, 2.890%]
Au half-cube 0.6×0.6 $\times 0.3\,\mathrm{mm}^3$	point source on top of half-cube	100 runs of $2 \cdot 10^6$ samples	142	$2.5 \cdot 10^5$	103.23% [102.90%, 103.56%]	3.005% [2.332%, 3.654%]
				$5 \cdot 10^5$		2.971% [2.337%, 3.652%]
				$1 \cdot 10^6$		2.956% [2.276%, 3.606%]
			710	$2.5 \cdot 10^5$	103.24% [102.90%, 103.56%]	6.648% [6.214%, 7.243%]
				$5 \cdot 10^5$		6.633% [6.183%, 7.215%]
				$1 \cdot 10^6$		6.619% [6.132%, 7.242%]

would still be quite useful as this corresponds to a moderately distorted spectrum.

As expected, an increased number of samples for the matrix generation results in a corresponding variance reduction of the algorithm error in the outermost right column. The results could be improved by optimizing the code e.g. by reducing the so-called cut off energies of the simulated particles (allowing for simulation at lower energies) or using variance reduction methods. Calculation times may also need to be considered. For instance, in the 4π absorber example ($N = 71$ energy bins, $m = 2.5 \cdot 10^5$ events per bin) the calculation time was approximately three hours on an Intel i7 laptop PC using a single core to construct the forward matrix. For smaller energy bin widths and more samples ($N = 710$ energy bins, $m = 1 \cdot 10^6$ events per bin) the calculation time scaled by a factor of 40 to around 120 hours. The Monte Carlo simulations consisted of more than 99% of the calculation time. These may easily be parallelized as the single-energy bin simulations can be run independently. Furthermore, most of the EGSnrc code allows for built-in parallelization. Thus, a large part of the simulations was carried out on a multicore computer cluster at the PTB Berlin.

5.2.4 Accuracy of the proposed unfolding algorithm

In order to test the accuracy of the proposed method, the unfolding algorithm was applied to data that was independent from the software EGSnrc, which was used for the above consistency checks. Firstly, we simulated measurement data in the Monte Carlo software PENELOPE [Sem03] for parameters that are comparable with those that are found in state-of-the-art MMC measurements concerning statistics, energy threshold and energy resolution, see e.g. [Loi19, Loi20].

Unfolding simulated histograms from another Monte Carlo software

^{36}Cl histograms were simulated using the pencyl code in PENELOPE [Sem03] and unfolded with the proposed algorithm implemented in EGSnrc as described above. Two cylindrical absorber geometries (4π and 2π) were simulated for a high number of beta particles to make any systematic deviations visible. The results are depicted in figures 5.23-5.24. The L^1-error is reduced by 79% using the unfolding algorithm for the PENELOPE data in the 4π geometry. The remaining variation seems to be statistical. The L^1-error is reduced by 98% using the unfolding algorithm for the PENELOPE data in a 2π geometry, with a deviation below $\sim 15\,\mathrm{keV}$ that is sensitive to the cut-off energy (below this energy, the considered particles are no longer simulated) and scattering parameters set in the respective software. In both software codes, a very high sensitivity was chosen and cut-off energies of 0.5 keV and 1 keV were used, respectively.

Notably, the semiconductor PIPS spectrum that was shown in figure 5.13 was unfolded with the proposed algorithm. There, the Monte Carlo simulations were done in GEANT4 and the corrected, unfolded spectrum shows excellent agreement with the corresponding MMC spectra that had a very high absorber quantum efficiency of 99.73% according to a simulation of the M absorber. The comparison is further evidence for the validity of the algorithm and its implementation using three different Monte Carlo software codes.

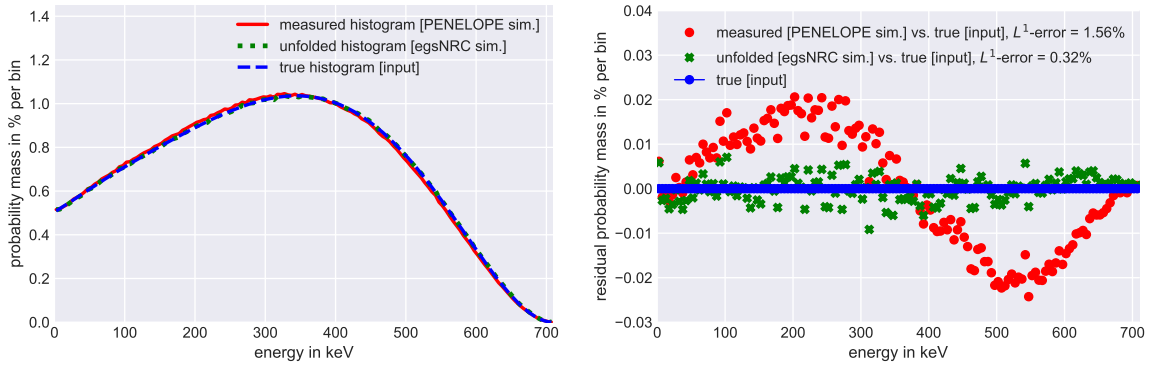

Figure 5.23: Approximately $n = 10^7$ beta particles of ^{36}Cl ($E_{\max} = 709.5\,\text{keV}$) were simulated in PENELOPE and plotted over 142 bins **(red)**. The 4π geometry consisted of a Au cylinder (height = 0.6 mm, radius = 0.3 mm) and EGSnrc was used to calculate the response matrix ($N = 142$ energy bins, $m = 10^6$ events per bin), which in turn was applied to unfold the simulated measured histogram **(green)**.

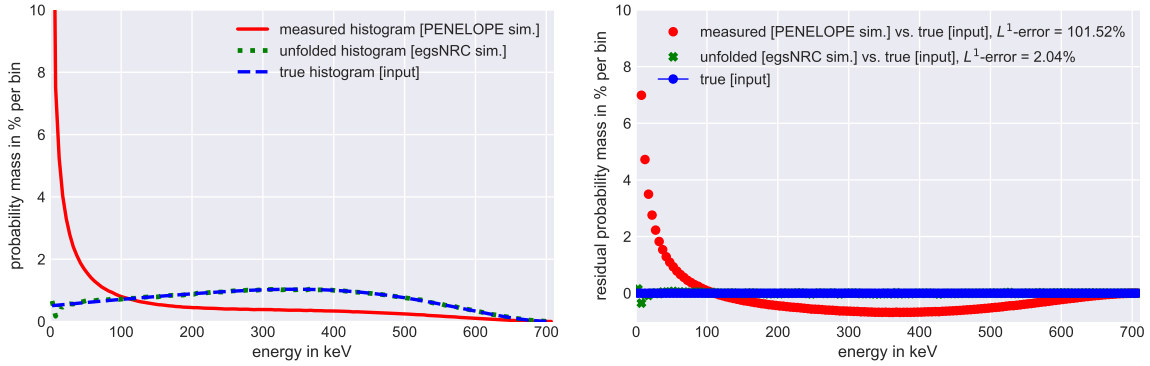

Figure 5.24: Approximately $n = 10^7$ of ^{36}Cl ($E_{\max} = 709.5\,\text{keV}$) were simulated in PENELOPE and plotted over 142 bins **(red)**. The 2π geometry consisted of a Au cylinder (height = 0.3 mm, radius = 0.3 mm) and EGSnrc was used to calculate the response matrix ($N = 142$ energy bins, $m = 10^6$ events per bin) for an idealized point source on top of the absorber, which in turn was applied to unfold the simulated measured histogram **(green)**.

6
Summary

The MetroBeta project [Loi18] aimed to improve theoretical computation methods of beta spectra along with modern measurement techniques for silicon detectors, solid scintillator crystals, magnetic spectrometers and MMCs. The motivation behind these efforts was to acquire radionuclide data, in particular the shape of the beta spectrum, as this would reduce the systematic error of primary activity determination such as the liquid scintillation counting methods CNET and TDCR. Central to this dissertation thesis was the optimization of beta spectrometers based on MMCs, in particular for the second forbidden non-unique transitions of ^{99}Tc and ^{36}Cl. The reason for this was two-fold: such transitions are difficult to calculate [Mou15] and the measurements of the literature do not cover the low-energy part of the spectrum [Kos19].

In the first part of the thesis, a high-resolution beta spectrum of ^{99}Tc was measured with an optimized 4π MMC detector. It features an energy resolution of approximately 100 eV and an energy threshold of ~ 0.75 keV, which is an improvement of approximately one and two orders of magnitude compared to the spectra found in the literature before the project started. Comparisons show excellent agreement with the independently measured spectrum of an equivalent MMC experiment performed at the LNHB [Loi19, Loi20]. When this spectrum was validated using liquid scintillation counting [Kos19], the activity deviation between the CNET and TDCR method was reduced by 78% when compared to the currently recommended beta spectrum [Rei74]. Comparing the experimental MMC data with a state-of-the-art theoretical calculation shows significant differences at energies below 10 keV even when the atomic exchange and screening effects are considered. While this approach was successful in calculating the spectrum at low energies in case of allowed and first forbidden non-unique beta transitions, it fails for ^{99}Tc as it is a second forbidden non-unique beta transition. Given our strong confidence in the measurement of this work and its experimental validation from another laboratory, it indicates that a novel theoretical calculation method needs

to be developed for such beta transitions. When this succeeds, it will enable us to extract an endpoint energy from the measured high-resolution beta spectra with greater confidence and could be added as recommended radionuclide data in the Decay Data Evaluation Project [Dde21]. This will be addressed in a future work.

In the second part of the thesis, a novel algorithm for microcalorimetric beta spectrometers was presented [Pau20]. Provided that one utilizes a reliable Monte Carlo code, has sufficient knowledge of the considered source and absorber geometry along with reasonable computing power, it is well applicable for the unfolding of measured beta spectra. This was demonstrated for partial energy escape corrections in 4π absorbers in the case of ^{36}Cl. Furthermore, the method can be used for other detectors and geometries $< 4\pi$, as was shown by the calculated 2π examples. In cases where it is not possible to completely embed a radionuclide in an ideal absorber, the presented unfolding algorithm may thus be combined with simpler beta spectrometers to allow for novel measurements. Certainly, the quality of the outcome from the proposed unfolding algorithm depends on the accuracy of the code to simulate the particle tracks. This, in turn, is strongly related to the (limited) accuracy of some interaction probabilities, e.g. the cross section for bremsstrahlung production. Results when using different Monte Carlo softwares were consistent. The algorithm has already been successfully applied for beta spectra that were measured with semiconductor calorimeters [Sin20]. Above its threshold of 25 keV, the unfolded ^{99}Tc spectrum agrees very well with the MMC measurements.

Notably, the development and improvement of primary activity measurements using low-temperature detectors are currently being pursued on both sides of the Atlantic Ocean. The American TrueBq project [Fit21, Fit22, Tru21] at the NIST will focus on using TES detectors for actinide radionuclides and new gravimetric methods. In Europe, the PrimA-LTD project [Pri21] will utilize MMCs to measure and standardize the alpha emitter ^{241}Am, the beta emitter ^{129}I and the electron-capture nuclide ^{55}Fe. A central part will be the development of new theoretical methods which over the years, within nuclear physics and other parts of science, has shown to go hand in hand with performing accurate experiments.

A

Supplementary material

A.1 On the continuity of $\beta^{\pm}$ spectra

Let the resting particle A decay into the daughter particle B while emitting an electron:

$$A \longrightarrow B + \mathrm{e}^{-} \tag{A.1}$$

By conservation of momentum and energy one has, respectively:

$$\begin{cases} \vec{p}_B + \vec{p}_{\mathrm{e}^-} = 0 \\ \\ \frac{p_B^2}{2m_B} + \sqrt{p_{\mathrm{e}^-}^2 + m_{\mathrm{e}^-}^2} = E_{\mathrm{released}} \end{cases} \tag{A.2}$$

Inserting the first equation of (A.2) into the second yields

$$\frac{p_{\mathrm{e}^-}^2}{2m_B} + \sqrt{p_{\mathrm{e}^-}^2 + m_{\mathrm{e}^-}^2} = E_{\mathrm{released}} \tag{A.3}$$

and solving for $p_{\mathrm{e}^-}^2$ yields a unique number and thus the electron has a single-valued kinetic energy when it is emitted.

As measured beta spectra seemed to have an unlimited number of lines, several explanations were proposed and since only one emitted particle could be detected, the conservation of momentum and energy were in fact questioned. However, it was the *neutrino hypothesis*, i.e. the proposal that a second particle that was electrically neutral and of extremely small mass is emitted next to the electron, that proved successful. The corresponding three body problem may be formulated as follows. Again, A is

initially at rest but emits an electron e^- and an (anti)neutrino $\overline{\nu}_{e^-}$:

$$A \longrightarrow B + e^- + \overline{\nu}_{e^-} \tag{A.4}$$

and by energy and impulse conservation one has

$$\begin{cases} \vec{p}_B + \vec{p}_{e^-} + \vec{p}_{\overline{\nu}_{e^-}} = 0 \\ \\ \frac{p_B^2}{2m_B} + \sqrt{p_{e^-}^2 + m_{e^-}^2} + \vec{p}_{\overline{\nu}_{e^-}} = E_{\text{released}} \end{cases} \tag{A.5}$$

The system of equations (A.5) is underdetermined as there are three unknowns but only two equations. Thus, there is a free parameter which leads to the sharing of the available kinetic energy after the decay between the electron and the (anti)-neutrino.

A.2 Radiometric dating with ^{14}C

In nature, carbon exists as three isotopes: the stable ^{12}C and ^{13}C and the beta emitter ^{14}C ($\beta^- = 100\%$, $E_{\max} = 146.476\,(4)\,\text{keV}$, $t_{1/2} = 5700\,(30)\,\text{a}$) [Be13]. The latter is produced when atmospheric nitrogen is hit by neutrons generated by cosmic radiation:

$$n + {}^{14}_{7}N \rightarrow {}^{14}_{6}C + p. \tag{A.6}$$

It then quickly reacts with oxygen to form carbon oxides and decays purely as

$${}^{14}_{6}C \rightarrow {}^{14}_{7}N + e^- + \overline{\nu}_e. \tag{A.7}$$

It is assumed that the atmospheric carbon ratio $\frac{^{14}C}{^{12}C} = \frac{1.25}{10^{12}}$ is approximately constant. Living organisms are in equilibrium with their surroundings concerning their carbon build-up, which means that in their life time their carbon ratio is also approximately constant. When the organism dies, however, the carbon exchange breaks down. The stable carbon remains intact while the radioactive carbon decays.

Using the exponential law (2.11) that describes the decaying number of radioactive nuclides in a sample with rate κ, one can determine its age. If the atomic concentrations $P(t)$ of the parent nuclide at different times $\{0, t\}$ are known, its age is given by [Pom15]:

$$\text{Age of sample} = t = \frac{1}{\kappa} \ln \left[\frac{P(0)}{P(t)} \right]. \tag{A.8}$$

Radiometric dating, depending on the half-life of the radionuclide, has wide ranging applications including biology, cosmology and geology. The activity of a specific radioactive sample changes in time as more nuclei decay. It is thus, appropriate to associate a reference time t_{ref} with an activity measurement, which can be used to derive decay correction factors for a sample [Pom15] that is applied e.g. for calibrating a laboratory detector.

A.3 Comparing experimental and theoretical beta spectra

One way of comparing a measured beta spectrum Y with a calculated spectrum Z i.e. the histograms $y = (y_1, \ldots, y_N)$ and $z = (z_1, \ldots, z_N)$, $y_i, z_i \in \mathbb{R}_{\geq 0}$ for $i = 1, \ldots, N$ over N bins is to calculate the R^2 value [Mou15] such that

$$R^2 := 1 - \frac{Var\,(e_i)}{Var\,(y_i)}, \quad \text{with } e_i := y_i - z_i,$$

$$Var\,(y_i) := \sum_{i=1}^{N} \frac{(y_i - \overline{y})^2}{N-1} \quad \text{and} \quad Var\,(e_i) := \sum_{i=1}^{N} \frac{e_i^2}{N-p-1},$$

where $\overline{y}$ is the arithmetic average of the histogram heights and p is the number of model parameters. In the case of beta spectra $p \in \{1, 2\}$, the maximal energy of the emitted beta particle $E_{\max}$ is one model parameter along with an additional one relating to a measurement normalization when shape factors derived from experimental data are used.

The standardized distribution of residuals is defined as

$$r_i := \frac{e_i}{\sqrt{Var\,(e_i)}}$$

and for unbiased comparisons of the same spectrum one would expect that $r_i \sim N(0, 1)$.

A.4 Formal proofs for the unfolding algorithm

In the following it is assumed that the number of simulated samples is $m \geq 1$ and the number of energy bins $N \geq 1$ to avoid degenerate cases. If nothing else is indicated, the statements hold almost surely, i.e. with probability 1 as random variables are considered.

Lemma A.4.1. *The total forward matrix*

$$\boldsymbol{S}_{N,m} = \sum_{j=1}^{N} \boldsymbol{S}_{N,m}^{j} = \begin{pmatrix} S_{N,m}^{1,1\leftarrow 1} & \cdots & S_{N,m}^{1,1\leftarrow N} \\ \vdots & \ddots & \vdots \\ S_{N,m}^{1,N\leftarrow 1} & \cdots & S_{N,m}^{1,N\leftarrow N} \end{pmatrix} \tag{A.9}$$

is upper triangular, in particular

i) $S_N^{j,k\leftarrow j} \in [0, 1]$ [bounded, non-negative entries]

ii) $S_N^{j,k\leftarrow j} = 0$ *for* $j < k$ [conservation of energy]

iii) $S_N^{j,k\leftarrow j} > 0$ *for* $j = k$ [non-zero diagonal elements]

iv) $\sum_{k=1}^{N} S_{N,m}^{j,k\leftarrow j} = 1$ [no loss of probability]

Proof. By construction, the entries of the total forward matrix distribute proportions between 0 and 1 of the simulation input histogram heights, which is expressed by i).

ii) By conservation of energy, the sum of energy depositions in the detector (which is detected as a single pulse by assumption A2)) for a single decay cannot be larger than the entire energy of the primary particle. Thus, "migration to the right" is not possible i.e. detection of higher energies than that of the primary particle. Please note that the simulations formally do not contain any noise part and that "migration to the right" could be possible for measurement data due to detector noise effects that are larger than the width of an energy bin. These issues can be addressed using correction algorithms for resolution distortion in continuous spectra, see e.g. [Wor64].

From assumption A3) it follows that the energy loss of the monoenergetic input is not total i.e. at least one of the m samples in each monoenergetic simulation is completely absorbed within the jth energy bin. This proves iii).

Part iv) follows by the same argument as for i) and assumption A3), i.e. the redistribution of the proportions sum to unity as some trace is always left in the detector. □

Proposition A.4.1. *The total forward matrix* $\boldsymbol{S}_{N,m}$ *is invertible.*

Proof. By lemma A.4.1 the matrix is triangular with non-zero diagonal elements, it follows that it has full rank and thus that it is invertible [Mey00, p.116 and 119]. □

It should be noted that due to the upper triangular nature of the forward matrix, the unfolding equation can be solved via a simple backward substitution algorithm [Hig89].

Proposition A.4.2. *The response matrix* $\boldsymbol{R}_N$ *is described by the total forward matrix with the following error estimate:*

$$\boldsymbol{R}_N = \boldsymbol{S}_{N,m} + \boldsymbol{O}_{N\times N}\left(m^{-\frac{1}{2}}\right), \tag{A.10}$$

where $\boldsymbol{O}_{N\times N}\left(m^{-\frac{1}{2}}\right)$ *denotes an* $N \times N$*-dimensional error matrix in which each component converges as* $O\left(m^{-\frac{1}{2}}\right)$ *and it follows that*

$$\boldsymbol{h}_{N,n}^{meas} = \boldsymbol{R}_N \boldsymbol{h}_{N,n} = \left[\boldsymbol{S}_{N,m} + \boldsymbol{O}_{N\times N}\left(m^{-\frac{1}{2}}\right)\right]\boldsymbol{h}_{N,n} \tag{A.11}$$

Proof. Given that the physics in the Monte Carlo simulations are sufficiently precise, for m independent samples it generally holds that the error of a single simulation quantity A is [Gra13, pp.37-48]

$$\Delta A(m) = \sqrt{\frac{Var(A)}{m}} = O\left(m^{-\frac{1}{2}}\right) \tag{A.12}$$

and the error for the monoenergetic forward operator estimate thus is

$$\Delta S_{N,m}^{j} = \sqrt{\frac{Var\left(S_{m,N}^{j}\right)}{m}} = \boldsymbol{O}_{N\times N}\left(m^{-\frac{1}{2}}\right). \tag{A.13}$$

For the total matrix operator, it holds that

$$\Delta S_{N,m} = \sqrt{\frac{Var\left(\sum_{j=1}^{N}\boldsymbol{S}_{N,m}^{j}\right)}{m}} = \boldsymbol{O}_{N\times N}\left(m^{-\frac{1}{2}}\right) \tag{A.14}$$

since the columns are independent from each other and

$$\boldsymbol{R}_N = \boldsymbol{S}_{N,m} + \boldsymbol{O}_{N\times N}\left(m^{-\frac{1}{2}}\right) \tag{A.15}$$

as the monoenergetic simulations describe the statistical histogram response sufficiently. Inserting this into the statistical discrete unfolding problem, it follows that

$$\boldsymbol{h}_{N,n}^{\text{meas}} = \boldsymbol{R}_N\boldsymbol{h}_{N,n} = \left[\boldsymbol{S}_{N,m} + \boldsymbol{O}_{N\times N}\left(m^{-\frac{1}{2}}\right)\right]\boldsymbol{h}_{N,n} \tag{A.16}$$

□

It is noted that the error decreases sublinearly in the number of simulated samples m used in each simulation. In contrast, the variance of each simulation increases in N for fixed m as there is less statistics in each energy bin. However, usually N is a fixed quantity determined by the energy resolution of the detector and the number of measured pulses n. Thus, the unfolding algorithm error can effectively be decreased by increasing the number of samples m in the Monte Carlo simulations or using variance reduction methods.

Proposition A.4.3. *For $N > 4$ it is not possible to estimate $\boldsymbol{S}_{N,m}$ using only one multi-energy bin simulation input distribution.*

Proof. Let $g_N^{\text{sim\_input}}$ be a multi-energy bin simulation $N \times 1$-input vector and $g_{N,m}^{\text{sim\_output}}$ be the corresponding $N \times 1$-output vector. To solve for $\boldsymbol{S}_{N,m}$ using only this information, one has using lemma A.4.1

$$\boldsymbol{S}_{N,m}\boldsymbol{g}_N^{\text{sim\_input}} = \boldsymbol{g}_{N,m}^{\text{sim\_output}} \tag{A.17}$$

i.e.

$$\begin{pmatrix} S_{N,m}^{1,1\leftarrow 1} & \cdots & S_{N,m}^{N,1\leftarrow N} \\ \vdots & \ddots & \vdots \\ \mathbf{0} & \cdots & S_{N,m}^{N,N\leftarrow N} \end{pmatrix}\begin{pmatrix} g_N^{\text{sim\_input},1} \\ \vdots \\ g_N^{\text{sim\_input},N} \end{pmatrix} = \begin{pmatrix} g_N^{\text{sim\_output},1} \\ \vdots \\ g_N^{\text{sim\_output},N} \end{pmatrix} \tag{A.18}$$

This system has

$$N^2 - \sum_{k=1}^{N-1} k = N^2 - \frac{N(N-1)}{2} = \frac{N(N+1)}{2}$$

unknowns (i.e. non-zero elements in the matrix). The number of equations can be partitioned as

i) N equations for the number of rows in the system.

ii) N equations for the number of columns in the system: each column in the matrix sums to unity.

iii) Two equations: the sum of the input entries and the output entries sum to unity, respectively.

Thus, in total one has $2(N+1)$ equations. The system becomes underdetermined if there are more unknowns than equations i.e.

$$\frac{N(N+1)}{2} > 2(N+1) \Leftrightarrow N > 4.$$

□

List of Figures

List of Tables

Bibliography

[Abb16] D. Abbaneo et al. Design of a constant fraction discriminator for the VFAT3 front-end ASIC of the CMS GEM detector. *Journal of Instrumentation*, 2016. DOI: https://doi.org/10.1088/1748-0221/11/01/c01023.

[Ago03] S. Agostinelli, J. Allison, K. a. Amako, J. Apostolakis, H. Araujo, P. Arce, M. Asai, D. Axen, S. Banerjee, G. Barrand, et al. GEANT4 - a simulation toolkit. *Nuclear instruments and methods in physics research section A: Accelerators, Spectrometers, Detectors and Associated Equipment*, 506(3):250–303, 2003. DOI: https://doi.org/10.1016/S0168-9002(03)01368-8.

[Ahm02] Q. Ahmad, R. Allen, T. Andersen, J. Anglin, J. Barton, E. Beier, M. Bercovitch, J. Bigu, S. Biller, R. Black, et al. Measurement of Day and Night Neutrino Energy Spectra at SNO and Constraints on Neutrino Mixing Parameters. *Physical Review Letters*, 89(1):011302, 2002. DOI: https://doi.org/10.1103/PhysRevLett.89.011302.

[Ake19] M. Aker, K. Altenmüller, M. Arenz, M. Babutzka, J. Barrett, S. Bauer, M. Beck, A. Beglarian, J. Behrens, T. Bergmann, et al. Improved Upper Limit on the Neutrino Mass from a Direct Kinematic Method by KATRIN. *Physical Review Letters*, 123(22):221802, 2019. DOI: https://doi.org/10.1103/PhysRevLett.123.221802.

[Alp15] B. Alpert, M. Balata, D. Bennett, M. Biasotti, C. Boragno, C. Brofferio, V. Ceriale, D. Corsini, P. K. Day, M. De Gerone, et al. HOLMES. *The European Physical Journal C*, 75(3):1–11, 2015. DOI: https://doi.org/10.1140/epjc/s10052-015-3329-5.

[Arm12] J. D. Armstrong. *Data Analysis and Double Pulse Detection for the MARE Experiment*. PhD thesis, University of Miami, 2012. URL https://scholarlyrepository.miami.edu/oa_dissertations/766.

[Ban93] S. Bandler, C. Enss, R. Lanou, H. Maris, T. More, F. Porter, and G. Seidel. Metallic Magnetic Bolometers for Particle Detection. *Journal of Low Temperature Physics*, 93(3-4):709–714, 1993. DOI: https://doi.org/10.1007/BF00693500.

[Bar94] M. Bardies and J.-F. Chatal. Absorbed doses for internal radiotherapy from 22 beta-emitting radionuclides: beta dosimetry of small spheres. *Physics in*

Medicine & Biology, 39(6):961, 1994. DOI: https://doi.org/10.1088/0031-9155/39/6/004.

[Bat16] C. Bates, C. Pies, S. Kempf, D. Hengstler, A. Fleischmann, L. Gastaldo, C. Enss, and S. Friedrich. Reproducibility and calibration of MMC-based high-resolution gamma detectors. *Applied Physics Letters*, 109(2):023513, 2016. DOI: https://doi.org/10.1063/1.4958699.

[Be11] M.-M. Bé, V. Chisté, C. Dulieu, X. Mougeot, V. Chechev, N. Kuzmenko, F. Kondev, A. Luca, M. Galan, A. Nichols, et al. Table of Radionuclides (Vol. 6-A = 22 to 242). *Monographie BIPM-5*, 6, 2011.

[Be13] M.-M. Bé, V. Chisté, C. Dulieu, X. Mougeot, V. Chechev, F. Kondev, A. Nichols, X. Huang, and B. Wang. Table of radionuclides (Vol. 7-A= 14 to 245). *Monographie BIPM-5*, 7, 2013.

[Be16] M.-M. Bé, V. Chisté, C. Dulieu, M. Kellett, X. Mougeot, A. Arinc, V. Chechev, N. Kuzmenko, T. Kibédi, A. Luca, et al. Table of radionuclides (Vol. 8-A= 41 to 198). *Monographie BIPM-5*, 8, 2016.

[Beh76] H. Behrens and L. Szybisz. Shapes of Beta Spectra, Physics Data. *ZAED 6-1*, 1976.

[Beh82] H. Behrens and W. Bühring. *Electron Radial Wave Functions and Nuclear Beta-decay*. Number 67. Oxford University Press, 1982.

[Bet21] X. Mougeot. BetaShape. URL http://www.lnhb.fr/rd-activities/spectrum-processing-software/.

[BIP12] Joint Committee for Guides in Metrology (JCGM). International vocabulary of metrology. *Bureau International de Poids et Mesures*, 3rd edition(200:2012). URL https://www.bipm.org/utils/common/documents/jcgm/JCGM_200_2012.pdf.

[Boc19] L. Bockhorn, M. Paulsen, J. Beyer, K. Kossert, M. Loidl, O. J. Nähle, P. C.-O. Ranitzsch, and M. Rodrigues. Improved Source/Absorber Preparation for Radionuclide Spectrometry Based on Low-Temperature Calorimetric Detectors. *Journal of Low Temperature Physics*, 2019. DOI: https://doi.org/10.1007/s10909-019-02274-8.

[Bog90] P. T. Boggs and J. E. Rogers. Statistical Analysis of Measurement Error Models and Applications: Proceedings of the AMS-IMS-SIAM joint summer research conference held June 10-16, 1989, with support from the National Science Foundation and the US Army Research Office. volume 112, pages 183–194. American Mathematical Soc., 1990.

[Bou00] J. Bouchard and P. Cassette. MAC3: an electronic module for the processing of pulses delivered by a three photomultiplier liquid scintillation counting

system. *Applied Radiation and Isotopes*, 52(3):669–672, 2000. DOI: https://doi.org/10.1016/S0969-8043(99)00228-6.

[Bro07] R. Broda, P. Cassette, and K. Kossert. Radionuclide metrology using liquid scintillation counting. *Metrologia*, 44(4):S36–S52, 2007. DOI: https://doi.org/10.1088/0026-1394/44/4/s06.

[Buh88] M. Bühler and E. Umlauf. A Magnetic Bolometer for Single-Particle Detection. *EPL (Europhysics Letters)*, 5(4):297, 1988. DOI: https://doi.org/10.1209/0295-5075/5/4/003.

[Cld19] Laboratoire National Henri Becquerel (LNHB). Nuclear decay scheme of ^{36}Cl. URL www.lnhb.fr/nuclides/Cl-36.txt.

[Col02] R. Collé and B. Zimmerman. A dual-compensated cryogenic microcalorimeter for radioactivity standardizations. *Applied Radiation and Isotopes*, 56(1-2):223–230, 2002. DOI: https://doi.org/10.1016/S0969-8043(01)00192-0.

[Col07] R. Collé. Classical radionuclidic calorimetry. *Metrologia*, 44(4):S118, 2007. DOI: https://doi.org/10.1088/0026-1394/44/4/S15.

[Cos93] E. Cosulich, F. Gatti, and S. Vitale. Further Results on μ-Calorimeters with Superconducting Absorber. *Journal of Low Temperature Physics*, 93(3):263–268, 1993. DOI: https://doi.org/10.1007/BF00693430.

[Cow56] C. L. Cowan, F. Reines, F. B. Harrison, H. W. Kruse, and A. D. McGuire. Detection of the Free Neutrino: a Confirmation. *Science*, 124(3212):103–104, 1956. DOI: https://doi.org/10.1126/science.124.3212.103.

[Cow98] G. Cowan. *Statistical Data Analysis*. Oxford University Press, 1998.

[Cza18] A. Czarnecki, W. J. Marciano, and A. Sirlin. Neutron Lifetime and Axial Coupling Connection. *Physical Review Letters*, 120:202002, May 2018. DOI: https://doi.org/10.1103/PhysRevLett.120.202002.

[Dde21] Decay Data Evaluation Project. www.nucleide.org/DDEP.htm.

[Des03] R. D. Deslattes, E. G. Kessler Jr, P. Indelicato, L. De Billy, E. Lindroth, and J. Anton. X-ray transition energies: new approach to a comprehensive evaluation. *Reviews of Modern Physics*, 75(1):35, 2003. DOI: https://doi.org/10.1103/RevModPhys.75.35.

[Dru07] D. Drung, C. Aßmann, J. Beyer, A. Kirste, M. Peters, F. Ruede, and T. Schurig. Highly Sensitive and Easy-to-Use SQUID Sensors. *IEEE Transactions on Applied Superconductivity*, 17(2):699–704, 2007. DOI: https://doi.org/10.1109/TASC.2007.897403.

[Egu03] K. Eguchi, S. Enomoto, K. Furuno, J. Goldman, H. Hanada, H. Ikeda, K. Ikeda, K. Inoue, K. Ishihara, W. Itoh, et al. First Results from KamLAND: Evidence for Reactor Antineutrino Disappearance. *Physical Review Letters*, 90(2):021802, 2003. DOI: https://doi.org/10.1103/PhysRevLett.90.021802.

[Fel52] L. Feldman and C. S. Wu. Investigation of the Beta-Spectra of ^{10}Be, ^{40}K, ^{99}Tc, and ^{36}Cl. *Phys. Rev.*, 87:1091–1099, Sep 1952. DOI: https://doi.org/10.1103/PhysRev.87.1091.

[Fer34] E. Fermi. Versuch einer Theorie der β-Strahlen. I. *Zeitschrift für Physik*, 88(3):161–177, 1934. DOI: https://doi.org/10.1007/BF01351864.

[Fit21] R. Fitzgerald, Z. Ahmed, D. Bergeron, N. Klimov, D. Schmidt, and R. Tosh. Micrometrology in pursuit of quantum radiation standards. *Measurement: Sensors*, 18:100295, 2021. DOI: https://doi.org/10.1016/j.measen.2021.100295.

[Fit22] R. P. Fitzgerald, B. Alpert, D. Becker, D. E. Bergeron, R. Essex, K. Morgan, S. Nour, G. O'Neil, D. Schmidt, G. A. Shaw, et al. Toward a New Primary Standardization of Radionuclide Massic Activity Using Microcalorimetry and Quantitative Milligram-Scale Samples. 2022. DOI: https://doi.org/10.6028/jres.126.048.

[Fle03] A. Fleischmann. *Magnetische Mikrokalorimeter: Hochauflösende Röntgenspektroskopie mit energiedispersiven Detektoren*. PhD thesis, Heidelberg University, 2003.

[Fle05] A. Fleischmann, C. Enss, and G. Seidel. Metallic Magnetic Calorimeters. In C. Enss, editor, *Cryogenic Particle Detection. Topics in Applied Physics*, pages 151–216. Springer, Berlin, Heidelberg, 2005. DOI: https://doi.org/10.1007/10933596_4.

[Fle09] A. Fleischmann, L. Gastaldo, S. Kempf, A. Kirsch, A. Pabinger, C. Pies, J. Porst, P. Ranitzsch, S. Schäfer, F. v. Seggern, T. Wolf, C. Enss, and G. M. Seidel. Metallic magnetic calorimeters. *AIP Conference Proceedings*, 1185(1):571–578, 2009. DOI: https://doi.org/10.1063/1.3292407.

[Fra09] A. Franklin. The Spectrum of β Decay: Continuous or Discrete? A Variety of Errors in Experimental Investigation. In *Going Amiss In Experimental Research*, pages 211–235. Springer, 2009. DOI: https://doi.org/10.1007/978-1-4020-8893-3_12.

[Fuk01] S. Fukuda, Y. Fukuda, M. Ishitsuka, Y. Itow, T. Kajita, J. Kameda, K. Kaneyuki, K. Kobayashi, Y. Koshio, M. Miura, et al. Constraints on Neutrino Oscillations Using 1258 Days of Super-Kamiokande Solar Neutrino Data. *Physical Review Letters*, 86(25):5656, 2001. DOI: https://doi.org/10.1103/PhysRevLett.86.5656.

[Ful51] H. Fulbright and J. Milton. The Beta-Spectrum of ^{36}Cl. *Physical Review*, 82(2):274, 1951. DOI: https://doi.org/10.1103/PhysRev.82.274.

[Gas14] L. Gastaldo, K. Blaum, A. Dörr, C. E. Düllmann, K. Eberhardt, S. Eliseev, C. Enss, A. Faessler, A. Fleischmann, S. Kempf, et al. The Electron Capture ^{163}Ho Experiment ECHo. *Journal of Low Temperature Physics*, 176(5):876–884, 2014. DOI: https://doi.org/10.1007/s10909-014-1187-4.

[Gei20] J. Geist. *Bestimmung der Isomerenergie von ^{229}Th mit dem hochauflösenden Mikrokalorimeter-Array maXs30*. PhD thesis, Heidelberg University, 2020.

[Gla70] S. L. Glashow, J. Iliopoulos, and L. Maiani. Weak Interactions with Lepton-Hadron Symmetry. *Phys. Rev. D*, 2:1285–1292, Oct 1970. DOI: https://doi.org/10.1103/PhysRevD.2.1285.

[Gra05] A. G. Carles. Beta shapefactor determinations by the cutoff energy yield method. *Nuclear Instruments and Methods in Physics Research Section A: Accelerators, Spectrometers, Detectors and Associated Equipment*, 551(2-3):312–322, 2005. DOI: https://doi.org/10.1016/j.nima.2005.05.070.

[Gra13] C. Graham and D. Talay. *Stochastic Simulation and Monte Carlo Methods: Mathematical Foundations of Stochastic Simulation*, volume 68. Springer Science & Business Media, 2013.

[Gro89] K. Grotz and H. V. Klapdor-Kleingrothaus. *Die schwache Wechselwirkung in Kern-, Teilchen-und Astrophysik: Eine Einführung*. Teubner, 1989.

[HDF19] The HDF group. URL https://www.hdfgroup.org.

[Hen12] D. Hengstler. Untersuchung der Eigenschaften von supraleitenden Re-, Zn- und Zn:Mn-Absorbern für magnetische Mikrokalorimeter. *Diplomarbeit, Kirchhoff-Institut für Physik, Universität Heidelberg*, 2012.

[Hen17] D. Hengstler. *Development and characterization of two-dimensional metallic magnetic calorimeter arrays for the high-resolution x-ray spectroscopy*. PhD thesis, Heidelberg University, 2017.

[Her49] L. Herforth and H. Kallmann. Die Fluoreszenzanregung von festem und flüssigem Naphthalin, Diphenyl und Phenanthren durch Alphateilchen, schnelle Elektronen und Gammastrahlen.(Mit 11 Abbildungen). *Annalen der Physik*, 439(5):231–245, 1949. DOI: https://doi.org/10.1002/andp.19494390503.

[Hig89] N. J. Higham. The Accuracy of Solutions to Triangular Systems. *SIAM Journal on Numerical Analysis*, 26(5):1252–1265, 1989. DOI: https://doi.org/10.1137/0726070.

[Hoo06] A. Hoover, M. Rabin, C. Rudy, D. Tournear, D. Vo, J. Beall, W. Doriese, R. Horansky, K. Irwin, J. Ullom, et al. Monte Carlo Studies of High Resolution Microcalorimeter Detectors. In *2006 IEEE Nuclear Science Symposium Conference Record*, volume 2, pages 1268–1272. IEEE, 2006. DOI: https://doi.org/10.1109/NSSMIC.2006.356074.

[Hoo15] A. S. Hoover, E. M. Bond, M. P. Croce, T. G. Holesinger, G. J. Kunde, M. W. Rabin, L. E. Wolfsberg, D. A. Bennett, J. P. Hays-Wehle, D. R. Schmidt, et al. Measurement of the ^{240}Pu/^{239}Pu Mass Ratio Using a Transition-Edge-Sensor Microcalorimeter for Total Decay Energy Spectroscopy. *Analytical chemistry*, 87(7):3996–4000, 2015. DOI: https://doi.org/10.1021/acs.analchem.5b00195.

[Irw05] K. D. Irwin and G. C. Hilton. Transition-Edge Sensors. *Cryogenic Particle Detection*, pages 63–150, 2005. DOI: https://doi.org/10.1007/10933596_3.

[Joh56] R. Johnson, O. Johnson, and L. Langer. Beta Spectrum of ^{36}Cl. *Physical Review*, 102(4):1142, 1956. DOI: https://doi.org/10.1103/PhysRev.102.1142.

[Kai06] J. Kaipio and E. Somersalo. *Statistical and Computational Inverse Problems*, volume 160. Springer Science & Business Media, 2006.

[Kal50] H. Kallmann. Scintillation Counting with Solutions. *Physical Review*, 78(5):621, 1950. DOI: https://doi.org/10.1103/PhysRev.78.621.2.

[Kaw05] I. Kawrakow, E. Mainegra-Hing, F. Tessier, R. Townson, and B. Walters. EGS_Ranmar Class Reference. URL https://nrc-cnrc.github.io/EGSnrc/doc/pirs898/classEGS__Ranmar.html.

[Kaw18] E. Kawrakow, D. Mainegra-Hing, F. Rogers, B. Walters, I. Kawrakow, D. Rogers, E. Mainegra, and F. Tessier. The EGSnrc Code System: Monte Carlo Simulation of Electron and Photon Transport. *Technical Report PIRS-701*, 2018.

[Kaw19] I. Kawrakow, E. Mainegra-Hing, F. Tessier, R. Townson, and B. Walters. tutor7pp.cpp application in C++. URL https://nrc-cnrc.github.io/EGSnrc/doc/pirs898/tutor7pp_8cpp-example.html.

[Kem18] S. Kempf, A. Fleischmann, L. Gastaldo, and C. Enss. Physics and Applications of Metallic Magnetic Calorimeters. *Journal of Low Temperature Physics*, 193(3):365–379, 2018. DOI: https://doi.org/10.1007/s10909-018-1891-6.

[Kir10] A. Kirsch. Entwicklung eines mikrostrukturierten metallisch magnetischen Kalorimeters mit massivem Rheniumabsorber zur β-Spektroskopie von ^{187}Re. *Diplomarbeit, Kirchhoff-Institut für Physik, Universität Heidelberg*, 2010.

[Kno10] G. F. Knoll. *Radiation Detection and Measurement*. Wiley, 2010.

[Koe21] K. E. Koehler. Low Temperature Microcalorimeters for Decay Energy Spectroscopy. *Applied Sciences*, 11(9):4044, 2021. DOI: https://doi.org/10.3390/app11094044.

[Kos11] K. Kossert, O. J. Nähle, and A. G. Carles. Beta shape-factor function and activity determination of ^{241}Pu. *Applied Radiation and Isotopes*, 69(9):1246–1250, 2011. DOI: https://doi.org/10.1016/j.apradiso.2011.03.046.

[Kos14] K. Kossert, A. G. Carles, and O. Nähle. Improved Čerenkov counting techniques based on a free parameter model. *Applied Radiation and Isotopes*, 86:7–12, 2014. DOI: https://doi.org/10.1016/j.apradiso.2013.12.022.

[Kos15] K. Kossert and X. Mougeot. The importance of the beta spectrum calculation for accurate activity determination of ^{63}Ni by means of liquid scintillation counting. *Applied Radiation and Isotopes*, 101:40–43, 2015. DOI: https://doi.org/10.1016/j.apradiso.2015.03.017.

[Kos18] K. Kossert, J. Marganiec-Gałązka, X. Mougeot, and O. J. Nähle. Activity determination of ^{60}Co and the importance of its beta spectrum. *Applied Radiation and Isotopes*, 134:212–218, 2018. DOI: https://doi.org/10.1016/j.apradiso.2017.06.015.

[Kos19] K. Kossert, J. Beyer, L. Bockhorn, F. Juget, M. Loidl, X. Mougeot, O. Nähle, M. Paulsen, P. Ranitzsch, and M. e. a. Rodrigues. Validation of beta spectra by means of liquid scintillation counting and Čerenkov counting. *Deliverable 7*, 15SIB10 MetroBeta, 2019. URL http://metrobeta-empir.eu/?page_id=1673.

[Kra13] S. Kraft-Bermuth, V. Andrianov, A. Bleile, A. Echler, P. Egelhof, P. Grabitz, S. Ilieva, C. Kilbourne, O. Kiselev, D. McCammon, et al. High-precision x-ray spectroscopy of highly charged ions with microcalorimeters. *Physica Scripta*, 2013(T156):014022, 2013. DOI: https://doi.org/10.1088/0031-8949/2013/T156/014022.

[LAn03] M. F. L'Annunziata. *Radioactivity Analysis*. Academic Press, 2003.

[LAn16] M. F. L'Annunziata. *Radioactivity: Introduction and History, from the Quantum to Quarks*. Elsevier, 2016.

[Loi10] M. Loidl, M. Rodrigues, B. Censier, S. Kowalski, X. Mougeot, P. Cassette, T. Branger, and D. Lacour. First measurement of the beta spectrum of ^{241}Pu with a cryogenic detector. *Applied Radiation and Isotopes*, 68(7):1454–1458, 2010. DOI: https://doi.org/10.1016/j.apradiso.2009.11.054. Proceedings of the 17th International Conference on Radionuclide Metrology and its Applications (ICRM 2009).

[Loi14] M. Loidl, M. Rodrigues, C. Le-Bret, and X. Mougeot. Beta spectrometry with metallic magnetic calorimeters. *Applied Radiation and Isotopes*, 87:302 – 305, 2014. DOI: https://doi.org/10.1016/j.apradiso.2013.11.024.

[Loi18] M. Loidl, J. Beyer, L. Bockhorn, C. Enss, D. Györi, S. Kempf, K. Kossert, R. Mariam, O. Nähle, M. Paulsen, M. Rodrigues, and M. Schmidt. MetroBeta: Beta Spectrometry with Metallic Magnetic Calorimeters in the Framework of the European Program of Ionizing Radiation Metrology. *Journal of Low Temperature Physics*, 193(5):1251–1256, 2018. DOI: https://doi.org/10.1007/s10909-018-1933-0.

[Loi19] M. Loidl, J. Beyer, L. Bockhorn, C. Enss, S. Kempf, K. Kossert, R. Mariam, O. Nähle, M. Paulsen, P. Ranitzsch, M. Rodrigues, and M. Schmidt. Beta spectrometry with metallic magnetic calorimeters in the framework of the European EMPIR project MetroBeta. *Applied Radiation and Isotopes*, 153:108830, 2019. DOI: https://doi.org/10.1016/j.apradiso.2019.108830.

[Loi20] M. Loidl, J. Beyer, L. Bockhorn, J. J. Bonaparte, C. Enss, S. Kempf, K. Kossert, R. Mariam, O. Nähle, M. Paulsen, P. Ranitzsch, M. Rodrigues, and M. Wegner. Precision Measurements of Beta Spectra using Metallic Magnetic Calorimeters within the European Metrology Research Project MetroBeta. *Journal of Low Temperature Physics*, 199(1):451–460, Apr 2020. DOI: https://doi.org/10.1007/s10909-020-02398-2.

[Lov89] D. Love and A. Nelson. Unfolding the response function of high-quality germanium detectors. *Nuclear Instruments and Methods in Physics Research Section A: Accelerators, Spectrometers, Detectors and Associated Equipment*, 274(3):541 – 546, 1989. DOI: https://doi.org/10.1016/0168-9002(89)90188-5.

[Mal20] A. G. Malonda and A. G. Carles. Chapter 7 - Radionuclide standardization. In M. F. L'Annunziata, editor, *Handbook of Radioactivity Analysis: Volume 2 (Fourth Edition)*, pages 531–625. Academic Press, fourth edition edition, 2020. DOI: https://doi.org/10.1016/B978-0-12-814395-7.00007-6.

[Mal82] A. G. Malonda and E. Garcia-Toraño. Evaluation of Counting Efficiency in Liquid Scintillation Counting of Pure β-Ray Emitters. *The International Journal of Applied Radiation and Isotopes*, 33(4):249–253, 1982. DOI: https://doi.org/10.1016/0020-708X(82)90022-9.

[Mat03] M. Matzke. Unfolding procedures. *Radiation protection dosimetry*, 107(1-3):149–168, 2003. DOI: https://doi.org/10.1093/oxfordjournals.rpd.a006384.

[McC05] D. McCammon. Thermal Equilibrium Calorimeters - An Introduction. In C. Enss, editor, *Cryogenic Particle Detection. Topics in Applied Physics*,

pages 1–34. Springer, Berlin, Heidelberg, 2005. DOI: https://doi.org/10.1007/10933596_1.

[Mey00] C. D. Meyer. *Matrix Analysis and Applied Linear Algebra*, volume 71. SIAM, 2000.

[Mou14] X. Mougeot and C. Bisch. Consistent calculation of the screening and exchange effects in allowed β^- transitions. *Phys. Rev. A*, 90:012501, Jul 2014. DOI: https://doi.org/10.1103/PhysRevA.90.012501.

[Mou15] X. Mougeot. Reliability of usual assumptions in the calculation of β and ν spectra. *Physical Review C*, 91(5):055504, 2015. DOI: https://doi.org/10.1103/PhysRevC.91.055504.

[Mou16] X. Mougeot. Systematic comparison of beta spectra calculations using improved analytical screening correction with experimental shape factors. *Applied Radiation and Isotopes*, 109:177–182, 2016. DOI: https://doi.org/10.1016/j.apradiso.2015.11.030.

[Nic06] A. Nicols. Summary Report of Consultants' Meeting on Beta-decay and decay heat, Vienna, Austria 12-14 December 2005. *IAEA Nuclear Data Section*, INDC (NDS)-0483, 2006. URL https://www.osti.gov/etdeweb/servlets/purl/20895414.

[Nuc21] Laboratoire National Henri Becquerel. TDCR method. www.nucleide.org/ICRM_LSCWG/icrmtdcr.htm.

[Odr21] SciPy 1.7.1. Orthogonal distance regression in Python's SciPy module. URL https://docs.scipy.org/doc/scipy/reference/odr.html.

[Ogr19] C. O'Grady. Stanford Linear Accelerator Center (SLAC): Constant Fraction Discriminator. URL https://confluence.slac.stanford.edu/display/PSDM/Constant+Fraction+Discriminator.

[Pau19] M. Paulsen, J. Beyer, L. Bockhorn, C. Enss, S. Kempf, K. Kossert, M. Loidl, R. Mariam, O. Nähle, P. Ranitzsch, and M. Rodrigues. Development of a beta spectrometry setup using metallic magnetic calorimeters. *Journal of Instrumentation*, 14(08):P08012–P08012, aug 2019. DOI: https://doi.org/10.1088/1748-0221/14/08/p08012.

[Pau20] M. Paulsen, K. Kossert, and J. Beyer. An unfolding algorithm for high resolution microcalorimetric beta spectrometry. *Nuclear Instruments and Methods in Physics Research Section A: Accelerators, Spectrometers, Detectors and Associated Equipment*, 953:163128, 2020. DOI: https://doi.org/10.1016/j.nima.2019.163128.

[Per22] I. PerkinElmer. Liquid Scintillation Cocktails. URL https://www.perkinelmer.com/de/lab-products-and-services/application-support-knowledgebase/radiometric/liquid-scintillation-cocktails.html.

[Poc88] K. Pochwalski, R. Broda, and T. Radoszewski. Standardization of Pure Beta Emitters by Liquid-Scintillation Counting. *International Journal of Radiation Applications and Instrumentation. Part A. Applied Radiation and Isotopes*, 39(2):165–172, 1988. DOI: https://doi.org/10.1016/0883-2889(88)90162-1.

[Pom07] S. Pommé. Methods for primary standardization of activity. *Metrologia*, 44(4):S17, 2007. DOI: https://doi.org/10.1088/0026-1394/44/4/S03.

[Pom15] S. Pommé. The uncertainty of the half-life. *Metrologia*, 52(3):S51, 2015. DOI: https://doi.org/10.1088/0026-1394/52/3/S51.

[Pom18] S. Pommé, H. Stroh, T. Altzitzoglou, J. Paepen, R. Van Ammel, K. Kossert, O. Nähle, J. D. Keightley, K. M. Ferreira, L. Verheyen, et al. Is decay constant? *Applied Radiation and Isotopes*, 134:6–12, 2018. DOI: https://doi.org/10.1016/j.apradiso.2017.09.002.

[Pri21] PrimA-LTD. https://prima-ltd.net/.

[Psd19] International Atomic Energy Agency. Phase-space database for external beam radiotherapy. URL https://www-nds.iaea.org/phsp/phsp.htmlx.

[Qui97] T. Quinn. Primary methods of measurement and primary standards. *Metrologia*, 34(1):61, 1997. DOI: https://doi.org/10.1088/0026-1394/34/1/9.

[Rah10] M. Rahman and G. Cho. Unfolding Low-Energy Gamma-Ray Spectrum obtained with NaI(Tl) in Air Using Matrix Inversion Method. *Journal of Scientific Research*, 2(2):221–226, 2010. DOI: https://doi.org/10.3329/jsr.v2i2.4372.

[Ran20] P.-O. Ranitzsch, D. Arnold, J. Beyer, L. Bockhorn, J. Bonaparte, C. Enss, K. Kossert, S. Kempf, M. Loidl, R. Mariam, et al. MetroMMC: Electron-capture spectrometry with cryogenic calorimeters for science and technology. *Journal of Low Temperature Physics*, 199(1):441–450, 2020. DOI: https://doi.org/10.1007/s10909-019-02278-4.

[Reg02] M. Reginatto, P. Goldhagen, and S. Neumann. Spectrum unfolding, sensitivity analysis and propagation of uncertainties with the maximum entropy deconvolution code MAXED. *Nuclear Instruments and Methods in Physics Research Section A: Accelerators, Spectrometers, Detectors and Associated Equipment*, 476(1-2):242–246, 2002. DOI: https://doi.org/10.1016/S0168-9002(01)01439-5.

[Rei74] M. Reich and H. M. Schüpferling. Formfaktor des β-Spektrums von ^{99}Tc. *Zeitschrift für Physik*, 271(2):107–113, Jun 1974. DOI: https://doi.org/10.1007/BF01676381.

[Rey50] G. T. Reynolds, F. B. Harrison, and G. Salvini. Liquid Scintillation Counters. *Physical Review*, 78(4):488, 1950. DOI: https://doi.org/10.1103/PhysRev.78.488.

[Rot07] H. Rotzinger. *Entwicklung magnetischer Mikrokalorimeter für die hochauflösende Spektroskopie des β-Emitters ^{36}Cl.* PhD thesis, Heidelberg University, 2007.

[Rot08] H. Rotzinger, M. Linck, A. Burck, M. Rodrigues, M. Loidl, E. Leblanc, L. Fleischmann, A. Fleischmann, and C. Enss. Beta Spectrometry with Magnetic Calorimeters. *Journal of Low Temperature Physics*, 151(3):1087–1093, 2008. DOI: https://doi.org/10.1007/s10909-008-9787-5.

[Rut03] E. Rutherford and F. Soddy. LX. Radioactive Change. *The London, Edinburgh, and Dublin Philosophical Magazine and Journal of Science*, 5(29):576–591, 1903. DOI: https://doi.org/10.1080/14786440309462960.

[Sal68] A. Salam. Proceedings of the 8th Nobel Symposium. *Almqvist & Wiksell, Stockholm*, 1968.

[Sas72] K. S. R. Sastry. Investigation of longitudinal polarization and other properties of some beta-transitions. Technical report, Massachusetts University Report No. AD-752621, 1972.

[Sch16] F. Schneider, K. Chrysalidis, H. Dorrer, C. Düllmann, K. Eberhardt, R. Haas, T. Kieck, C. Mokry, P. Naubereit, S. Schmidt, and K. Wendt. Resonance ionization of holmium for ion implantation in microcalorimeters. *Nuclear Instruments and Methods in Physics Research Section B: Beam Interactions with Materials and Atoms*, 376:388 – 392, 2016. DOI: https://doi.org/10.1016/j.nimb.2015.12.012.

[Sch66] E. Schwerdtel. Simple method for an exact efficiency determination in liquid scintillation counting of low-energy beta emitters. *Atomkernenergie (West Germany) Merged with Kerntechnik to form Atomkernenerg./Kerntech. Acta Radiol. Changed to Acta Radiol.: Oncol., Radiat. Phys.*, 11, 1966.

[Sci19] SciPy.org. Documentation of numpy.linalg.solve. URL https://docs.scipy.org/doc/numpy-1.15.0/reference/generated/numpy.linalg.solve.html.

[Sei86] W. Seidel. Diplomarbeit. *Technische Universität München*, 1986.

[Sem03] J. Sempau, J. Fernández-Varea, E. Acosta, and F. Salvat. Experimental benchmarks of the Monte Carlo code PENELOPE. *Nuclear Instruments and Methods in Physics Research Section B: Beam Interactions with Materials and Atoms*, 207(2):107–123, 2003. DOI: https://doi.org/10.1016/S0168-583X(03)00453-1.

[Sim21] E. Simpson. The Colourful Nuclide Chart. URL https://people.physics.anu.edu.au/~ecs103/chart/.

[Sin19] A. Singh, X. Mougeot, B. Sabot, D. Lacour, and A. Nourreddine. Beta spectrum measurements using a quasi-4π detection system based on Si detectors. *Applied Radiation and Isotopes*, 154:108897, 2019. DOI: https://doi.org/10.1016/j.apradiso.2019.108897.

[Sin20] A. Singh. *Metrological study of the shape of beta spectra and experimental validation of theoretical models*. PhD thesis, Université de Strasbourg, 2020.

[Sny66] R. E. Snyder and G. B. Beard. Decay of ^{94}Nb and ^{94m}Nb. *Phys. Rev.*, 147:867–870, Jul 1966. DOI: https://doi.org/10.1103/PhysRev.147.867.

[Sta56] N. Starfelt and H. W. Koch. Differential Cross-Section Measurements of Thin-Target Bremsstrahlung Produced by 2.7- to 9.7-MeV Electrons. *Phys. Rev.*, 102:1598–1612, Jun 1956. DOI: https://doi.org/10.1103/PhysRev.102.1598.

[Suh07] J. Suhonen. *From Nucleons to Nucleus: Concepts of Microscopic Nuclear Theory*. Springer Science & Business Media, 2007.

[Szy93] A. E. Szymkowiak, R. L. Kelley, S. H. Moseley, and C. K. Stahle. Signal Processing for Microcalorimeters. *Journal of Low Temperature Physics*, 93(3):281–285, 1993. DOI: https://doi.org/10.1007/BF00693433.

[Tai51] S. I. Taimuty. The Beta-Spectrum of ^{99}Tc. *Phys. Rev.*, 81:461–462, Feb 1951. DOI: https://doi.org/10.1103/PhysRev.81.461.

[Tay19] R. Taylor, R, M. Chamberland, D. Rogers, and R. Thomson. EGS Brachy. URL https://clrp-code.github.io/egs_brachy/index.html.

[Tcd20] Laboratoire National Henri Becquerel (LNHB). Nuclear decay scheme of ^{99}Tc. URL www.lnhb.fr/nuclides/Tc-99.txt.

[Tru21] National Institute of Standards and Technology. TrueBq. https://www.nist.gov/programs-projects/basic-metrology-true-becquerel-new-paradigm-21st-century-radioactivity.

[Vel20] C. Velte. *Measurement of a high energy resolution and high statistics ^{163}Ho electron capture spectrum for the ECHo experiment*. PhD thesis, Heidelberg University, 2020.

[Ver09] R. M. Verkouteren and J. R. Verkouteren. Inkjet Metrology: High-Accuracy Mass Measurements of Microdroplets Produced by a Drop-on-Demand Dispenser. *Analytical Chemistry*, 81(20):8577–8584, 2009. DOI: https://doi.org/10.1021/ac901563j.

[vRo95] G. van Rossum. Python tutorial, CS-R9526. Technical report, Centrum voor Wiskunde en Informatica (CWI), Amsterdam, 1995.

[Wat78] M. Waterman and D. Whiteman. Estimation of probability densities by empirical density functions. *International Journal of Mathematical Education in Science and Technology*, 9(2):127–137, 1978. DOI: https://doi.org/10.1080/0020739780090201.

[Wei67] S. Weinberg. A Model of Leptons. *Physical Review Letters*, 19:1264–1266, Nov 1967. DOI: https://doi.org/10.1103/PhysRevLett.19.1264.

[Wei92] C. F. von Weizsäcker. Die Philosophie eines Physikers, Vortrag am 22. Juni 1992 in der Universität Bamberg. URL https://youtu.be/LVHOvDsPoQ0.

[Wil67] J. Willett and E. Spejewski. A method for resolution correction and shape factor analysis of beta spectra. *Nuclear Instruments and Methods*, 52(1):77 – 85, 1967. DOI: https://doi.org/10.1016/0029-554X(67)90560-5.

[Wor64] D. Wortman and J. Cramer. The correction of resolution distortion in continuous pulse-height spectra. *Nuclear Instruments and Methods*, 26:257 – 262, 1964. DOI: https://doi.org/10.1016/0029-554X(64)90086-2.

[Wu55] C. S. Wu. Beta and Gamma-Ray Spectrometry. Series in Physics, page 345. Interscience Publ., New York, 1955.